



Universidad de Valladolid

PROGRAMA DE DOCTORADO EN QUÍMICA

TESIS DOCTORAL:

**STRUCTURAL PROBES FOR
SWEETNESS: MICROWAVE
SPECTROSCOPIC STUDIES OF
EDULCORANTS**

Presentada por Gabriela Juárez López para
optar al grado de

Doctor/a por la Universidad de Valladolid

Dirigida por

Iker León Ona y Elena Rita Alonso Alonso

Esta investigación ha sido finaniciada por:
Ministerio de Ciencia e Innovación y la Junta de
Castilla y León



Plan Nacional I+D+I
CTQ 2016-76393-P
FPI GRANT: BES-2017-082173
PID 2019-111396GB-100



VA077U16
VA244P20

La presente tesis doctoral se ha llevado a cabo en los Laboratorios de Espectroscopía y Bioespectroscopía del Grupo de Espectroscopía Molecular (GEM) de la Universidad de Valladolid, gracias al proyecto de investigación CTQ2016-76393-P: Biomoléculas y Moléculas del Medio Interestelar: Relaciones Estructura-Propiedad, Quiralidad y Detección en el ISM, otorgado por el Ministerio de Ciencia e Innovación. Durante este período (2018-2022) se han realizado estudios sobre la estructura-propiedad en edulcorantes y biomoléculas.

Agradecimientos

Me gustaría agradecer en primer lugar a mi tutor, el profesor José Luis Alonso, por acogerme con el contrato FPI y que me ayudase a mi llegada a Valladolid. Sin su ayuda no habría sido posible comenzar esta tesis doctoral.

Agradezco a mis directores de tesis, la Dra. Elena Alonso y al Dr. Iker León. Gracias a Iker por su ayuda a pesar de las innumerables dificultades y cargar con el peso de la tesis. A Elena por su ayuda y por darme la oportunidad de continuar con las moléculas de su proyecto.

Gracias a todos los miembros del grupo GEM especialmente a Lucie, Raúl, Sergio, Santi, Miguel y todas las personas que han pasado por aquí y han alegrado mis días.

Me gustaría dar las gracias a la Dra. María Eugenia Sanz, profesora del King's College London, por sus muy buenas correcciones, dejarme participar en su grupo, darme la oportunidad de exponer mi primera charla en inglés, y ayudarme a hacerlo muy amablemente. A sus estudiantes por su cordialidad, especialmente a Indy que sacaba un rato para hablar conmigo y así poder mejorar mi inglés.

A Bea por los mojitos, cafés e interminables charlas por WhatsApp. Gracias por hacer mis días más amenos.

Agradezco especialmente en esta dura pero enriquecedora etapa de mi vida a mi amigo, el profesor Francisco Javier Tapiador. Gracias por su apoyo, leer todos mis correos (infinitos), por creer en mí, por enseñarme tanto y ayudarme a crecer, tanto a nivel profesional como personal, gracias por mostrarme lo que es ser un gran científico y una muy buena persona. Mis palabras solo reflejan un poco de toda la ayuda que he recibido de su parte en todos estos años.

Me gustaría agradecer a mi familia por las charlas y risas: mi padre, mi abuela Yayi, tíos y primos.

Por último, quiero dar las gracias a mi madre Claudia y a mis hermanas Verónica y Viviana, que, a pesar de los obstáculos de la vida, lograron que creciera en un ambiente de risas y felicidad. Cada momento a su lado es una aventura preciosa. Asimismo, me gustaría destacar los brazos fuertes de mi madre, fruto de tanto remar, gracias por enseñarme que lo imposible es posible.

A mi madre y mis hermanas

Índice

Resumen	1
Abstract.....	3
1. Introducción	5
1.1. Receptores gustativos	7
1.2. Sabor dulce	8
1.3. Edulcorantes.....	9
1.4. Poder edulcorante y requisitos	11
1.5. Relación estructura-propiedad: teoría molecular del sabor dulce.....	12
1.6. Justificación y Objetivos.....	15
1.7. Referencias.....	19
2. Metodología.....	23
2.1. Metodología experimental	26
2.2. Metodología Computacional.....	29
2.3. Fundamentos teóricos	31
2.4. Software empleado	35
2.5. Referencias.....	36
Resultados.....	37
3. Chapter: Rotational Spectrum and Conformational Analysis of Perillartine: Insights into the Structure–Sweetness Relationship	41
3.1. Introduction.....	43
3.2. Results and Discussion	44
3.3. Conclusion	52
3.4. References.....	53
4. Chapter: Understanding the sweetness of the rare sugar β -D-allose	55
4.1. Introduction.....	57
4.2. Results and Discussion	58
4.3. Conclusion	65
4.4. References.....	66

5. Chapter: The Structural Sign of Sweetness in the Artificial Sweetener Dulcin: A Rotational Study	69
5.1. Introduction.....	71
5.2. Results and Discussion	72
5.3. Conclusion	79
5.4. References.....	80
6. Chapter	83
Unveiling the Eight Forms of Caffeic Acid	83
6.1. Introduction.....	85
6.2. Results and Discussion	86
6.3. Conclusion	91
6.4. References.....	92
7. Conclusions and Future Perspectives	95
Conclusiones y Perspectivas Futuras.....	101
Annex	107
Annex I	109
Annex II	117
Annex III.....	125
Annex IV.....	131

Resumen

La determinación de la estructura tridimensional (3D) de las biomoléculas es de enorme interés porque nos ayuda a obtener respuestas plausibles acerca de las implicaciones de los compuestos en el entorno biológico. En esta memoria de investigación se recoge la caracterización estructural de diferentes moléculas percibidas como dulces: la perillartina, la dulcina y la alosa. Así como también del ácido cafeico, el cual es un compuesto que se utiliza en la industria farmacéutica.

Todas las investigaciones se llevaron a cabo mediante espectroscopía de rotación. En concreto, se utilizaron dos espectrómetros denominados *Laser Ablation Chirped Pulse Fourier Transform Microwave* (LA-CP-FTMW) que operan en los intervalos de frecuencias de 2 a 8 y de 6 a 14 GHz. Además, se realizaron cálculos de mecánica molecular y mecano-cuánticos que facilitaron el análisis espectral.

Estos estudios estructurales fueron abordados para comprobar la Teoría Molecular del Dulzor postulada por Shallenberger-Acree-Kier, la cual no se había podido verificar debido a la falta de información estructural intrínseca de las moléculas. En esta tesis se pudo analizar satisfactoriamente la disposición “glucófora” de los tres compuestos dulces.

En la perillartina se identificaron cuatro confórmeros bajo condiciones de aislamiento generado en la expansión supersónica, todos ellos presentan una configuración *E* del grupo C=N con respecto al doble enlace del anillo. Todas las geometrías caracterizadas cumplen con los requisitos de la teoría del dulzor, incluso, se pudo conjeturar con una doble posibilidad de recepción de la molécula con los receptores de las papilas gustativas.

En cuanto a la dulcina, se pudieron identificar dos confórmeros, ambas estructuras están estabilizadas por una interacción intramolecular N-H $\cdots\pi$ entre el -NH₂ y el anillo de fenilo. Además, se predijo un tercer isómero, pero no se pudo detectar debido al fenómeno de interconversión conformacional. Todas las especies analizadas están en concordancia con Shallenberger, Acree y Kier.

Con respecto a la alosa se lograron detectar tres especies, las cuales exhiben una disposición en sentido contrario a las agujas del reloj de la red de enlaces de hidrógeno intramolecular. Adicionalmente, se hicieron cálculos de interacciones no covalentes (*NCIplot*), para cerciorarse sobre la disposición glucófora. Todas las estructuras cumplen la teoría del dulzor. La similitud de los puntos glucóforos de la alosa y de la glucosa podrían ser la razón de la igualdad de dulzor en ambos compuestos.

Finalmente, en la investigación estructural de la molécula de ácido cafeico se pudo materializar la sutileza en la caracterización de la espectroscopía de rotación, dado que se consiguió descifrar el paisaje conformacional completo de este compuesto. Esta molécula presenta ocho especies, las cuales difieren entre ellas ligeramente. Asimismo, este estudio estructural nos proporciona información muy valiosa que nos ayudaría a elucidar los mecanismos subyacentes a la actividad biológica de este compuesto.

Abstract

The determination of the three-dimensional (3D) molecular geometry of biomolecules is of great interest because it helps us to obtain plausible answers about the implications of compounds in their biological environment. In this thesis, we pursue the structural characterization of molecules perceived as sweet: perillartine, dulcin and allose. Additionally, caffeic acid, which is a compound used in the pharmaceutical industry is also studied.

All the investigations were carried out using rotational spectroscopy. More precisely, two spectrometers known as *Laser Ablation Chirped Pulse Fourier Transform Microwave* (LA-CP-FTMW) were used in the 2 to 8 and 6 to 14 GHz frequency ranges. The results were complemented with computational methods using molecular mechanics and quantum-mechanical calculations to facilitate the analysis.

The results obtained for the sweet compounds were used in order to verify the molecular theory of sweetness postulated by Shallenberger-Acree-Kier. This theory could not be verified so far due to the lack of intrinsic structural information of the molecules. The results obtained in this work allows to satisfactorily analyze the "glucophore" arrangement of the three characterized molecules.

Four conformers were identified in perillartine under the isolated conditions of a supersonic expansion. All the conformers show a *E* configuration of the C=N group with respect to the double bond of the ring. Additionally, the characterized geometries meet the requirements of the sweetness theory, and it was possible to conjecture that perillartine has a double chance of interacting with the receptors located in the taste buds.

In the study of dulcin, two conformers were detected, both structures being stabilized by an intramolecular N-H $\cdots\pi$ interaction between -NH₂ and the phenyl ring. Furthermore, a third isomer was predicted but could not be detected due to conformational interconversion phenomenon. All the species analyzed are in agreement with the theory proposed by Shallenberger, Acree and Kier.

Regarding allose, three species were detected which exhibit a counterclockwise arrangement of the intramolecular hydrogen bond network. Additionally, the results were complemented with calculations using non-covalent interactions (*NCIplot*), to ascertain the glucophore disposition. All the conformers observed fulfill the requirement of the sweetness theory. The similarity of the glucophore points in allose and glucose could explain their similar sweetness.

Finally, the structural investigation of caffeic acid materialized the subtlety in the characterization provided by rotational spectroscopy, since it was possible to decipher the complete conformational landscape of this compound. This molecule has eight species, which differ slightly from each other. Additionally, this structural study provides us with valuable information that would help us to elucidate the mechanisms underlying the biological activity of this compound.

1. Introducción

(Introduction)

El proceso sensorial comienza una vez un estímulo físico o químico actúa sobre los receptores sensoriales. Es por ello que el estímulo se define como el agente químico o físico que produce la respuesta de los receptores sensoriales externos o internos. Dentro de los 5 principales sistemas sensoriales, el gusto es una de las experiencias más duraderas y satisfactorias del cuerpo y, excepto el dolor, ningún otro sistema sensorial está tan completamente desarrollado al nacer. De hecho, la razón de tal desarrollo tiene un sentido evolutivo. Por ejemplo, las sustancias que provocan el gusto son responsables de funciones tan importantes como un aporte de sales, proteínas, energía, o pueden alertar de sustancias peligrosas (tóxicas o venenosas) o en mal estado [1–6]. Es por ello que la capacidad de los animales para distinguir entre algo nutricional frente a algo potencialmente letal puede significar la diferencia entre la vida y la muerte. Es decir, los largos años de adaptación durante la evolución ha hecho que la percepción e impresiones sensoriales determinen si un alimento es aceptado por determinado animal o no [7,8].

Curiosamente, entre los sentidos del hombre, el del gusto es el menos entendido, aunque se ha avanzado bastante en la dilucidación de su funcionamiento. El ser humano puede percibir un total de cinco sabores: dulce, salado, amargo, ácido, y umami. En la lengua existen alrededor de 10000 pequeñas estructuras llamadas papilas gustativas. Estas estructuras se componen de un conjunto de receptores sensoriales llamados receptores gustativos, que están conectadas a ramificaciones nerviosas que envían señales al cerebro. Al comer alimentos, estos son disueltos en la saliva, penetrando las papilas gustativas a través de los poros que hay en la lengua. Estas células nerviosas poseen en su parte superior unos filamentos que dan respuesta a estas sustancias, generando un impulso nervioso que llega al cerebro y se transforma en una sensación: el sabor.

1.1. Receptores gustativos

En un inicio se consideraba que la lengua tenía una distribución topográfica de los sabores en la lengua, es decir, un “mapa del gusto” [9]. En concreto, se pensaba que los sabores dulce y salado se detectaban en la punta de la lengua, el amargo en la zona posterior, mientras que el sabor ácido y el sabor umami eran captados en los laterales y en la zona intermedia de este órgano. No obstante, hoy en día se sabe que este punto de vista es incorrecto y que las células receptoras del sabor pueden detectar múltiples modalidades básicas del gusto creando una distribución uniforme en toda la lengua.

Dependiendo de la proteína receptora, se distinguen dos tipos de receptores gustativos: ionotrópicos y metabotrópicos [10]. Los receptores ionotrópicos actúan como un canal iónico ligando dependiente y participan en la percepción de sustancias saladas y ácidas. Cuando alguna de estas sustancias entra en contacto con estos receptores, los canales iónicos se abren, produciéndose la despolarización de la célula. Posteriormente, esta despolarización desencadena distintos eventos que finaliza en la interpretación del cerebro como un sabor (salado para Na^+ y ácido en el caso del H^+). En cuanto a los receptores metabotrópicos, no son canales iónicos y la señalización de éstos depende de la activación de varias moléculas dentro de la célula. Cuando la sustancia adecuada (dulce, amarga o umami) estimula un receptor gustativo metabotrópicos, éste genera una

cascada de acontecimientos moleculares que finaliza con la percepción del sabor en nuestro cerebro. En la Figura 1, se detallan los dos tipos de receptores localizados en la lengua.

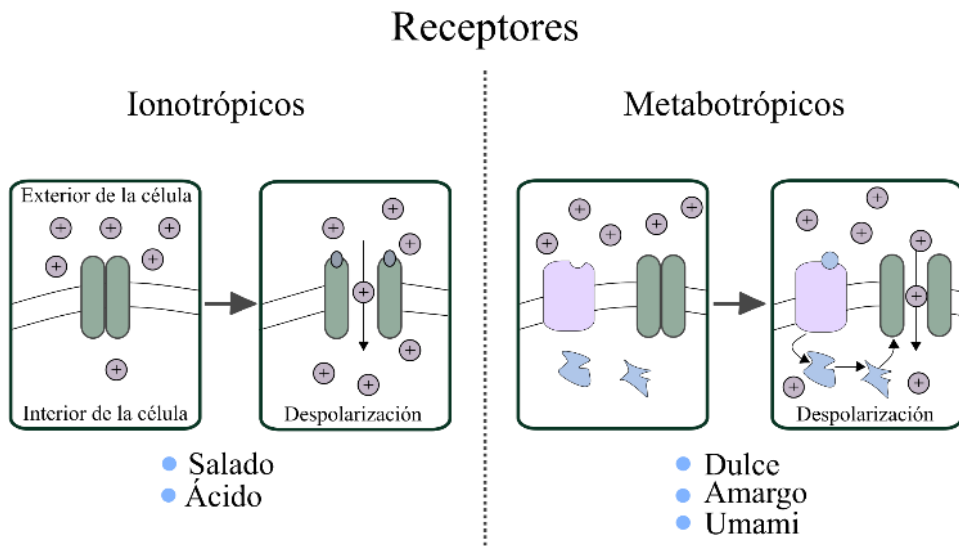


Figura 1. Mecanismo de los receptores ionotrópicos y metabotrópicos que da lugar a la percepción de los distintos sabores.

1.2. Sabor dulce

De las cinco cualidades gustativas, el mecanismo de percepción del dulzor es uno de los eventos fisiológicos más complejos y se produce cuando los receptores del sabor dulce son estimulados por algunas moléculas como los azúcares, edulcorantes artificiales, o aminoácidos. Estos receptores, conocidos como receptores T1Rs, están acoplados a proteínas G (GPRCs). Existen tres tipos de receptores T1R1, T1R2 y T1R3 que se pueden unir dando lugar a 3 combinaciones: T1R1+3, el cual da lugar al receptor del sabor umami, T1R2+3 dando lugar al receptor del sabor dulce y T1R3 solo que conlleva detectar altas concentraciones de azúcares, pero no el sabor dulce. Estos receptores constan de proteínas transmembrana con un dominio externo que une a la molécula responsable del sabor (ligando) y otro dominio interno asociado a proteínas G. La unión del ligando al receptor provoca un cambio conformacional que a su vez crea un cambio en las proteínas heterotriméricas G, activándolas y provocando una cascada de señalización.

En este paso del proceso de transferencia de información, las moléculas de fosfatidilinositol 4,5-bifosfato (PIP₂) se convierten a su homólogo trifosfato (PIP₃) y diacilglicerol. Posteriormente, el PIP₃ se dirige a los canales de calcio produciéndose una liberación de Ca²⁺. El calcio intracelular posibilita la apertura de canales de adenosín trifosfato (ATP), permitiendo la liberación de éstos al medio extracelular. Posteriormente, los neurotransmisores (ATP) estimulan las células sinápticas. Finalmente, nuestro cerebro recibe los impulso eléctricos provenientes de las neuronas, y los descodifica en la percepción de dulzor [11,12]. La Figura 2 muestra un esquema del proceso.

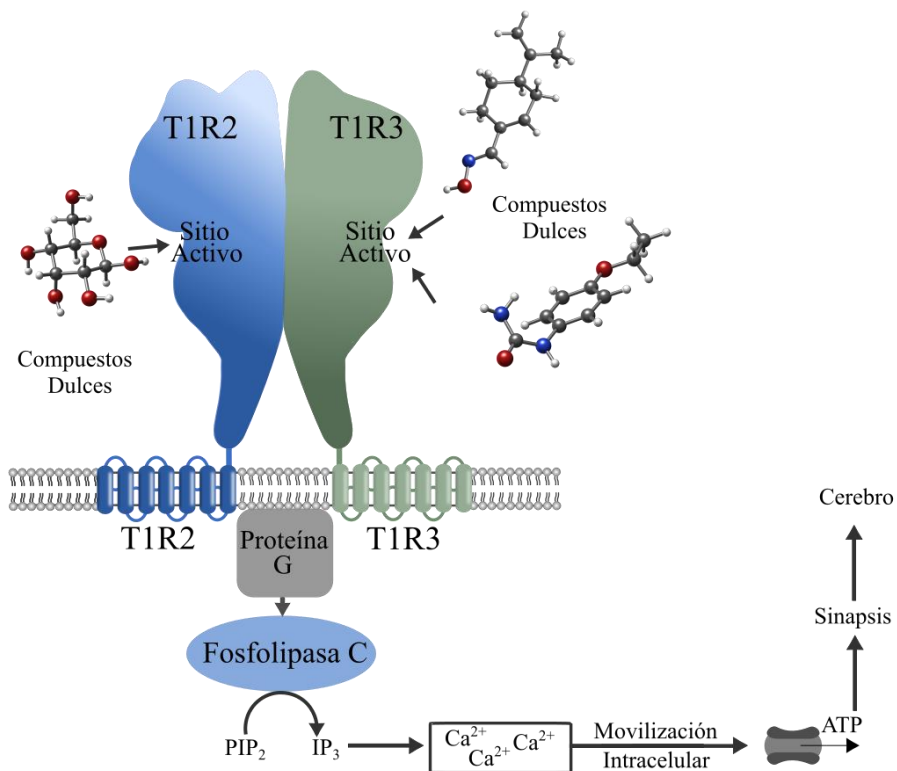


Figura 2. Esquema sobre el mecanismo de la percepción sensorial del dulzor.

En este proceso, el cerebro no solo recibe información sobre el dulzor de los alimentos o bebidas, sino que, además, se producen profundos efectos biológicos. Cuando consumimos alimentos azucarados, las neuronas en la región de la recompensa son más dinámicas, creando sentimientos de placer [13]. De esta manera, los seres humanos intentamos recrear estados anímicos agradables, lo que nos lleva a buscar una y otra vez en este tipo de alimentos [14].

1.3. Edulcorantes

Debido a nuestra atracción por el sabor dulce, existe un enorme interés en buscar, diseñar y desarrollar sustancias comestibles que no sean necesariamente azúcares, pero que emulen dicho sabor. Los aditivos alimentarios, por ejemplo, son sustancias que normalmente no se consumen como alimentos en sí, sino que se incorporan a los alimentos de forma deliberada. La finalidad por la que se añaden es diversa y pueden añadirse para la conservación del alimento, intensificar su sabor o modificar alguna de sus propiedades incluido el dulzor [15].

De forma más específica, los edulcorantes son sustancias naturales o artificiales con la propiedad de dotar de sabor dulce similar al del azúcar a un alimento o producto. El Código Alimentario Español define a los edulcorantes artificiales como sustancias sápidas sintéticas que, sin tener cualidades nutritivas, poseen un poder edulcorante superior al de cualquier hidrato de carbono al que sustituyen o refuerzan [16].

A continuación, se mencionan los dos usos más importantes de los edulcorantes a día de hoy.

- Uso de edulcorantes en la dieta

Es un hecho que la sensación de placer al ingerir alimentos dulces ha provocado un consumo excesivo de alimentos azucarados. Estos aditivos se añaden para que los alimentos tengan un buen sabor y nos sintamos atraídos por ellos. La bollería, alimentos precocinados, ultraprocesados o bebidas azucaradas son la principal fuente de azúcares añadidos en la dieta de la población de países industrializados. En consecuencia, un gran porcentaje de la población de estos países sufre obesidad, y enfermedades asociadas a éstas como hipertensión, diabetes o caries [17–19]. Se estima que el 20 % de las calorías que consume un adulto proviene de azúcares [20]. Estas calorías equivaldrían a comer 9 cucharadas de azúcar al día.

Desafortunadamente, estos azúcares añadidos no proporcionan ningún beneficio para nuestra salud y, por este motivo, muchas organizaciones de la salud (OMS) recomiendan que la población reduzca la adición de azúcar. Así, en las últimas cuatro décadas, ha emergido un mercado de edulcorantes no calóricos y productos dietéticos para responder a las necesidades millones de personas [21–24]. Como se ha mencionado anteriormente, un edulcorante es un compuesto alternativo al azúcar de mesa que se emplea para endulzar alimentos o bebidas. Existen diferentes tipos de edulcorantes, los cuales se clasifican según su origen: naturales o artificiales. Los edulcorantes naturales se extraen de plantas (stevia), frutas (fructosa), caña de azúcar o miel. Mientras que los edulcorantes artificiales son productos de reacciones químicas llevadas a cabo en un laboratorio, entre éstos destaca la sacarina. Además, estos edulcorantes se dividen según el contenido energético: calóricos y no calóricos. Algunos edulcorantes no calóricos o de alta intensidad presentan contenido calórico pero al utilizarse en pequeñas cantidades, su valor energético es residual [25].

- Uso de edulcorantes en fármacos

La gran mayoría de fármacos son administrados mediante vía oral. Curiosamente, aunque es menos sabido, el sabor es el factor más influyente en la aceptación de estos fármacos [26]. De hecho, es un requisito importante en el caso de pastillas o comprimidos que son, generalmente, amargos. Por supuesto, existe también un punto de vista comercial para el empleo de edulcorantes, ya sean artificiales o naturales, en la composición de los medicamentos [26].

En cualquier caso, no hay que olvidar que el empleo de edulcorantes no es trivial y no puede añadirse cualquier edulcorante en cualquier fármaco: por ejemplo, las interacciones entre el principio activo y los excipientes pueden afectar a la naturaleza química, estabilidad y la biodisponibilidad del medicamento. Esto conllevaría a cambios en la eficiencia y seguridad del fármaco [27–29]. Algunos edulcorantes comúnmente empleados en este campo se mencionan a continuación:

- La sacarosa se emplea en siropes para aportar viscosidad y consistencia a los fluidos. Es uno de los edulcorantes más utilizados en fármacos.

- La lactosa se usa a modo de excipiente en pastillas. También es muy utilizado.
- La trehalosa ayuda a incrementar el tiempo de vida de las plaquetas por lo que se emplea en la conservación de la sangre. Esto es útil para almacenar sangre destinada a las transfusiones o para preservar embriones.
- El xilitol es empleado en fármacos con propiedades expectorantes, recubrimientos de vitaminas, y puede encontrarse en la composición de suplementos alimentarios como aminoácidos, elementos traza o azúcares no reductores.

En definitiva, el diseño de edulcorantes es muy importante en la actualidad: es importante encontrar nuevas moléculas que proporcionen un sabor intenso a la vez que puedan tener otras propiedades beneficiosas y que no sean perjudiciales. Para ello, son claves dos factores: se necesita una forma de cuantificar la medida de la intensidad y se necesita entender la interacción entre el ligando y el receptor, es decir, la relación estructura-propiedad.

1.4. Poder edulcorante y requisitos

Normalmente, el poder edulcorante de una molécula no se da en función de su concentración sino mediante la determinación del umbral de percepción del sabor. A continuación, en la Figura 3 se muestran algunos edulcorantes naturales y artificiales. Asimismo, se especifica la intensidad y el valor energético de estos compuestos [30,31].

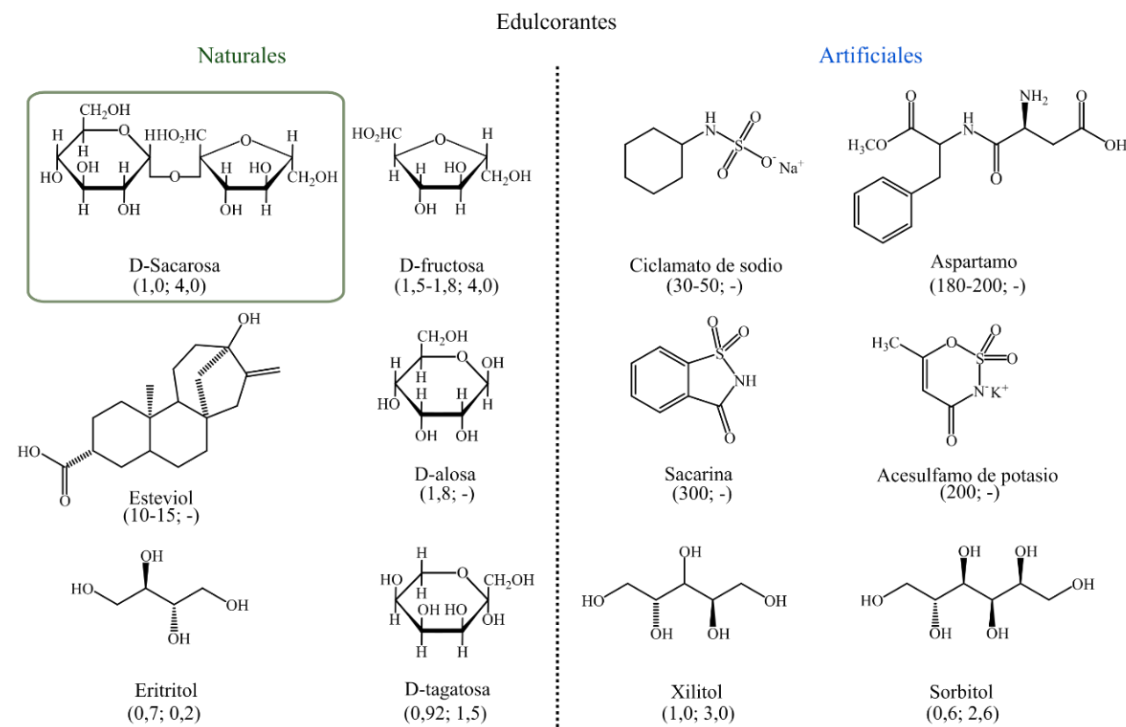


Figura 3. Estructura química de diferentes edulcorantes naturales y artificiales. Entre paréntesis se detalla la intensidad de dulzor con respecto a la sacarosa y la contribución calórica en Cal.g⁻¹.

Además de una alta intensidad, estos aditivos deben presentar una serie de características para que puedan ser empleados en la industria alimentaria o farmacéutica: deben ser inocuos, es decir que no muestren efectos adversos para nuestra salud (tóxico); el sabor dulce tiene que ser lo más parecido al azúcar común y no dejar un sabor metálico residual (el producto alimenticio final debe tener un sabor similar al tradicional). Además, un edulcorante ideal debe ser soluble en agua y estable tanto en condiciones ácidas como básicas y en un amplio intervalo de temperaturas. Un edulcorante debe ser también compatible con una amplia gama de ingredientes alimentarios, ya que el dulzor es solo un componente de los complejos sistemas del sabor. Asimismo, un edulcorante para que tenga éxito debe tener un precio competitivo en relación con la sacarosa y edulcorantes comparables [21].

Sin embargo, como se observa en la Figura 3, es difícil prever cuando una molécula será dulce o no, ya que la disposición estructural y los grupos funcionales que poseen parecen muy distintos. Por ello, la investigación y desarrollo de nuevos edulcorantes que cumplan con todos estos requisitos, no es una tarea sencilla y requiere de una profunda comprensión sobre las bases moleculares del sabor dulce.

1.5. Relación estructura-propiedad: teoría molecular del sabor dulce

Desde comienzos del siglo XX, se han buscado las características que debe tener una molécula o sustancia para ser dulce. Los primeros estudios apuntaban a que se necesitaba una molécula que en su estructura molecular tuviese unos determinados grupos funcionales. En cuanto a las teorías generales sobre las sustancias sápidas, Faraday y Arrhenius propusieron la primera clasificación en la que proponían que los sabores ácido y salado eran generados por moléculas ionizables en disolución. Las primeras especulaciones sobre la correlación entre el dulzor y la estructura química de las sustancias, se remonta a Cohn (1914). Observó patrones simples en la estructura química de los compuestos dulces. Por ejemplo, vio que las sustancias polihidroxiladas y los α -aminoácidos suelen dulces, mientras que los compuestos altamente nitrados suelen ser amargos. Al reconocer estos grupos funcionales propuso una unidad sapófora en la molécula: ésta debía contener un gran número de grupos hidróxilos [32].

Posteriormente, Oertly y Myers (1919) sugirieron que los compuestos dulces para ser percibidos como tal, debían de tener dos unidades a las cuales denominaron “glucóforo” y “auxogluc”. Un ejemplo representativo de estas especulaciones es el glicol ($\text{HOCH}_2\text{CH}_2\text{OH}$), en donde el *glucóforo* es el HOCH_2CHOH , mientras que el hidrógeno restante actuaría como *auxogluc*. Esta propuesta puso algo de orden al trabajo de Cohn [33] y un año más tarde, Kodama (1920) [34] especuló sobre la existencia de un hidrógeno activo o “vibratorio” en las moléculas percibidas como dulce. Este hidrógeno era una forma de tautomerismo [35]. Posteriormente, numerosos científicos fueron aportando diversas modificaciones o teorías sobre el dulzor de los compuestos [36]. En 1966, Deutsch y Hansch [37] señalaron que, para que una molécula fuera percibida como dulce, debía de ser hidróffila y presentar densidad electrónica en un punto específico de la molécula.

Es aquí donde nace una de las teorías más extendidas del siglo XX gracias a su sencillez y correspondencia con una gama amplia de moléculas con diferentes grupos funcionales. En 1967 Shallenberger y Acree [38] propusieron una teoría molecular sobre el dulzor, postulando que las moléculas dulces contienen un sistema *AH-B*, en el que *AH* es un grupo donor de protones, mientras que *B* es una unidad aceptora, separados por una distancia entre 2.5 y 4 Å. Estos dos grupos formarían el conjunto denominado como *glucóforo*, que podría interactuar con un grupo complementario *AH/B*, situado en el receptor de las papillas gustativas, mediante enlaces de hidrógeno.

Finalmente, Kier [39] conjeturó sobre un tercer sitio de recepción, el cual denominó como γ , el cual presenta un carácter hidrofóbico e interacciona con el receptor mediante fuerzas dispersivas. Este punto se especuló por la estereoselectividad de las moléculas: los D-aminoácidos son generalmente dulces, mientras que los L, en su mayoría, no. A esta disposición tridimensional completa formados por los puntos *AH/B/γ*, se le conoce como *triángulo del dulzor*. En la Figura 4, se detalla la disposición glucófora con las distancias que debe presentar para que las moléculas sean percibidas como dulces.

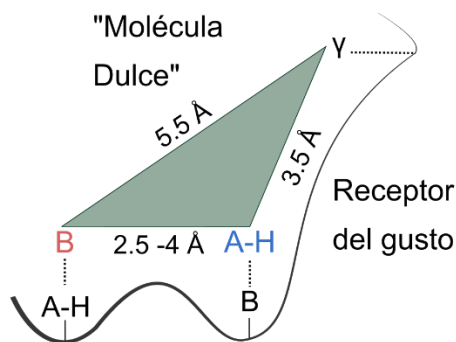


Figura 4. Modelo propuesto en la teoría de Shallenberger-Acree-Kier.

A pesar de que esta teoría pudiera parecer sencilla, ha explicado el dulzor en diversas moléculas. Algunos de los grupos de moléculas analizadas por Shallenberger, Acree y Kier [39–41] se muestran en la Figura 5 y se detallan a continuación:

- **Carbohidratos:** Los hidroxilos son racionalizados como una entidad bifuncional, en donde pueden actuar como donadores de protones (*AH*) o aceptores (*B*). Por ejemplo, en la glucosa, el componente donador (*AH*) es el O₄H mientras que el acceptor es O₃ (*B*). En cuanto al tercer punto γ , se sitúa en el grupo CH₂OH, que en posición *trans* aumenta el carácter hidrofóbico mejorando notablemente el dulzor. Otra molécula representativa de estos monosacáridos es la fructosa, cuya unidad *B/AH*, se localiza en O₁ y O₂H, respectivamente; el punto γ se ubica en el C₆.
- **Oximas:** En estos compuestos se ha especulado con varias posibilidades de interacción con el receptor. Inicialmente, Shallenberger y Acree sugirieron que la entidad dadora de protones en la perillartina (oxima más destacada) estaba conformado por el grupo hidroxilo de la molécula (*AH*), mientras que la unidad *B* era la nube deslocalizada del anillo. Más tarde, Kier supuso que el átomo de hidrógeno en posición *ortho* con respecto a la oxima era el punto *AH* y el oxígeno o nitrógeno correspondían al punto *B*.

• **Ureas:** La propiedad dulce de estos compuestos se debe a que contienen la disposición glucófora ubicada en los grupos amina (*AH*) y carbonilo (*B*), respectivamente. Además, se conjectura que el punto γ está en grupo *alcoxi*, en el caso de la dulcina se localiza en el segundo carbono [36].

• **Sulfamidas:** En este grupo de compuestos podemos mencionar como más representativos a la sacarina y al sulfamato de sodio. La tripartita glucófora de esta familia se sitúa en los átomos NH (*AH*) y O (*B*), con respecto al punto γ se encuentra en un carbono, el cual se señala en la Figura 5 para cada edulcorante.

• **Aminoácidos:** El sistema *AH/B* es el grupo amino y carboxilo. En estos compuestos es muy importante el radical (R) y la actividad óptica, dado que afecta a la percepción de dulzor. La mayoría de los D-aminoácidos son dulces, excepto la D-alanina.

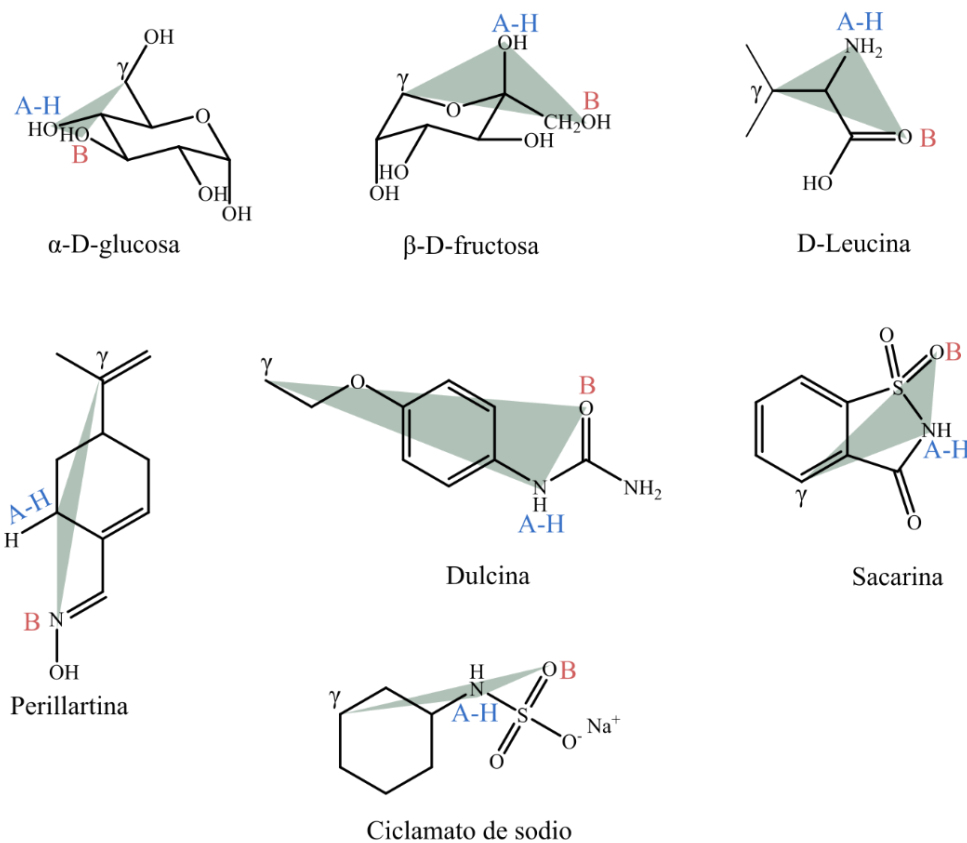


Figura 5. Estructura química de compuestos dulces y el triángulo del dulzor.

Más tarde, se propusieron modelos más complejos como el planteado por Van der Heijden (1985) *et al* [36], quienes introdujeron un nuevo parámetro para describir el tercer sitio de recepción. En este trabajo se especula que la intensidad de percepción del dulzor, se debe a la longitud de la cadena del tercer punto. En otra teoría molecular sobre el sabor dulce se mencionan ocho categorías funcionales organizadas en alta afinidad y sitios secundarios que contribuyen al sabor dulce [42]. Sin embargo, estos modelos subsiguientes contienen el concepto tripartito que, a pesar del descuido de la forma tridimensional, tiene un enorme mérito por su criterio sencillo en la racionalización de la relación estructura-dulzor.

1.6. Justificación y Objetivos

La enorme implicación de la alimentación, además de los daños que causan las dietas modernas ricas en azúcar en el bienestar y salud, han hecho que surja un campo en la investigación sobre las mejoras de los productos alimenticios existentes y el diseño de nuevos aditivos a la carta; es decir, que posean las características deseadas, pero sin olvidar que no han de existir efectos adversos.

Como se ha descrito en la introducción de esta memoria, una teoría muy empleada y que correlaciona el dulzor de las moléculas con su estructura es la postulada por Shallenberger, Acree y Kier. En el caso de los edulcorantes, entender si estos cumplen dicha teoría daría paso a confirmarla o mejorar las teorías actuales. Esto nos ayudaría a relacionar las estructuras moleculares con aquellos receptores del gusto con los que interaccionan y, comprender así, los mecanismos del dulzor y su funcionamiento. Con esta información sería posible proponer el diseño de nuevos edulcorantes artificiales aptos para el consumo y que cumplan con ciertos requisitos tales como una disminución del aporte calórico, no producir alergias e intolerancias, además de maximizar la sensación de dulzor. También hay que tener en cuenta que, en numerosas ocasiones, una pequeña modificación en la molécula o cambio de quiralidad pueden transformar una molécula dulce en amarga.

Por esta razón es importante estudiar la relación entre las propiedades de los edulcorantes con su estructura. No obstante, la información estructural que se posee de los edulcorantes hasta el momento es escasa. Además, la mayoría de estudios están realizados en fase condensada donde muchas de las interacciones están perturbadas y condicionadas por el medio que las rodea. Por ello, determinar la estructura en condiciones aisladas podría aportar una información útil. Con este fin, el Grupo de Espectroscopía Molecular (GEM) ha desarrollado técnicas que permiten la transferencia de moléculas termolábiles de fase sólida a fase gas. De esta forma, es posible observar los confórmeros más estables en el espectro obtenido mediante espectroscopía de rotación, así como su abundancia, para poder determinar su estructura y comprobar si posee un grupo de átomos que forme el glucóforo. Mediante esta metodología se han estudiado moléculas importantes como cetohexosas, como por ejemplo la fructosa, tagatosa, sorbosa y psicosa [43]; polialcoholes como el sorbitol y dulcitol [44]; y otras sustancias como la sacarina [45], todas ellas poseedoras en su estructura de un glucóforo como el descrito en la teoría de Shallenberger-Acree-Kier. Un esquema de dichos resultados se recoge en la Figura 6.

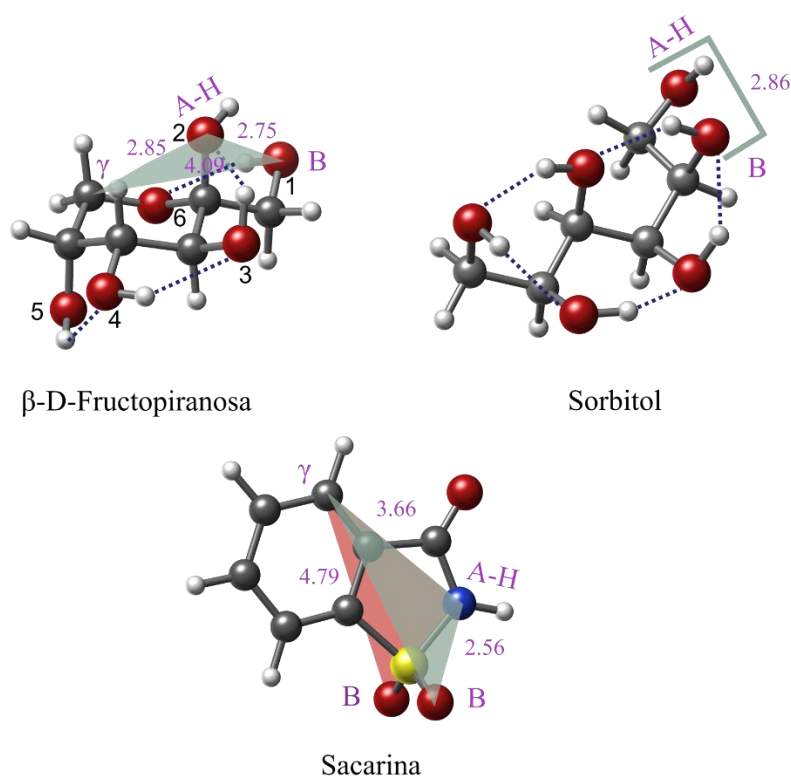


Figura 6. Estructura tridimensional de los edulcorantes de la fructopiranosa, sorbitol y sacarina con su disposición glucófora. Las distancias se dan en Ángstrom.

Dado los excelentes resultados obtenidos y motivados por ello, el grupo GEM ha firmado un convenio con la empresa Helios, quienes forman parte del proyecto. Es aquí donde nace la motivación de este trabajo: ampliar la investigación a otras “moléculas dulces” con diferentes grupos funcionales para continuar aportando datos experimentales a la teoría del dulzor.

Así, el objetivo principal de este trabajo es la determinación estructural de los confórmeros más estables de la perillartina, alosa y dulcina, cuyas estructuras moleculares se muestran en la Figura 7, mediante espectroscopía de rotación. Esto permitirá dilucidar las disposiciones que adoptan estas moléculas en un entorno libre de interacciones, determinar cuáles serán sus confórmeros más estables, y la disposición de los distintos grupos funcionales, así como las distancias entre los posibles glucóforos. Los resultados podrían aportar estudiar la relación entre las estructuras predominantes y sus propiedades dulces atendiendo a la teoría de Shallenberger-Acree-Kier.

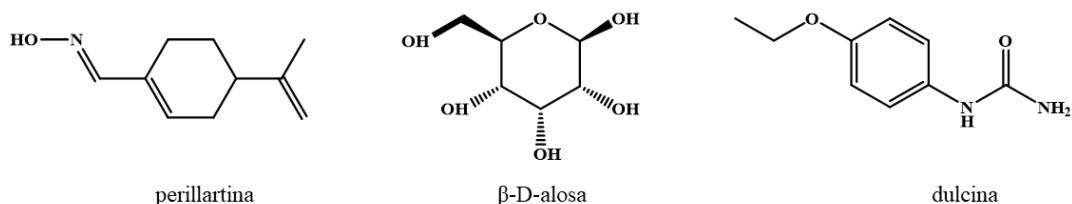


Figura 7. Estructura molecular de la perillartina, alosa y dulcina.

La razón de la elección de estas moléculas son varias. Por un lado, estos edulcorantes presentan un intenso sabor dulce y esta propiedad excepcional podría transferirse a la síntesis de otros edulcorantes más adecuados para el consumo. Por otro lado, cada molécula presenta distintos grupos funcionales: la perillartina es una oxima que contiene un ciclohexeno donde el doble enlace se conjuga con el doble enlace C = N y presenta un grupo hidroxilo. La dulcina es un edulcorante artificial que pertenece a la familia de las poliureas y presenta dos aminas (primaria y secundaria), un carbonilo, un anillo aromático y un grupo alcoxi. Finalmente, la alosa es un monosacárido del grupo de las aldohexosas, más concretamente es el epímero C₃ de la glucosa, y posee varios grupos hidroxilos.

Aunque esta memoria se centre fundamentalmente en corroborar la teoría del dulzor, también se realizó la caracterización estructural del ácido cafeico (Figura 8), teniendo en mente el añadido de aditivos en la comida o en medicamentos. El ácido cafeico se encuentra ampliamente distribuido en los alimentos como un éster junto con el ácido quínico, también llamado ácido clorogénico (ácido 5-cafeoilquínico) [46-48]. El ácido cafeico muestra una amplia variedad de propiedades fisiológicas y farmacológicas [49-52], lo que resulta muy atractivo en la industria farmacéutica.

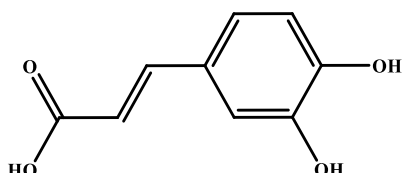


Figura 8. Estructura molecular del ácido cafeico.

Para llevar a cabo el objetivo propuesto, se llevarán a cabo los siguientes subobjetivos:

- Obtener los confórmeros más estables de la perillartina, alosa, dulcina y ácido cafeico sus momentos dipolares y constantes de rotación mediante mecánica molecular y mecánica cuántica, cuyos datos facilitarán la interpretación del espectro experimental.
- Preparación de las muestras y obtención de los espectros de rotación mediante espectroscopía de rotación en banda ancha acopladas a un sistema láser de

pulsos de picosegundos. Esto último será fundamental debido a que las moléculas de interés no son volátiles.

- Asignación conformacional de las estructuras más estables mediante la simbiosis de las metodologías teórica y experimental.
- Determinación de los glucóforo y comprobación del cumplimiento con la teoría de Shallenberger-Acree-Kier.

1.7. Referencias

1. Kinnamon, S. C. and T. A. Cummings, Chemosensory transduction mechanisms in taste, *Annu. Rev. Physiol.* **1992**, *54*, 715–731.
2. Adam Drewnowski, F. B.; Mennella, J. A.; Johnson, S. L. Sweetness and Food Preference, *J. Nutr.* **2012**, 1142–1148.
3. Mennella, J. A. and Bobowski, N. K. The sweetness and bitterness of childhood: Insights from basic research on taste preferences, *Physiol. Behav.* **2015**, *152*, 502–507.
4. Beauchamp, G. K. Why do we like sweet taste: A bitter tale?, *Physiol. Behav.* **2016**, *164*, 432–437.
5. Mergenthaler, P.; Lindauer, U.; Dienel, G. A. and Meisel, A. Sugar for the brain: the role of glucose in physiological and pathological brain function, *Trends Neurosci.* **2013**, *10*, 587-597.
6. Ramirez, I. Why do sugars taste good?, *Neurosci. Biobehav. Rev.* **1990**, *14*, 125–134.
7. Goldsmith, R. H. A tale of two sweeteners, *J. Chem. Educ.* **1987**, *64*, 954.
8. Shallenberger, R. S. Taste recognition chemistry, *Pure Appl. Chem.* **1997**, *69*, 659–666.
9. Häning, D. P. Engelmann, **1901**.
10. Gilbertson, T. A.; Damak, S. and Margolskee, R. F. The molecular physiology of taste transduction, *Curr. Opin. Neurobiol.* **2000**, *10*, 519–527.
11. Meyers, B. and Brewer, M. S. Sweet taste in man: A Review, *J. Food Sci.* **2008**, *73*, 6.
12. Assadi-Porter, F. M.; Radek, J. ; Rao, H. and Tonelli, M. Multimodal ligand binding studies of human and mouse G-coupled taste receptors to correlate their species-specific sweetness tasting properties, *Molecules* **2018**, *10*, 2531.
13. Kenny, P. J. Reward Mechanisms in Obesity: New Insights and Future Directions, *Neuron* **2011**, *69*, 664–679.
14. Del Parigi, A.; Chen, K. A.; Salbe, D.; Reiman, E. M. and Tataranni, P. A. Are we addicted to food?, *Obes. Res.* **2003**, *11*, 493–495.
15. C. de la U. E. Parlamento Europeo, Reglamento (CE) nº 1333/2008 sobre aditivos alimentarios, *D. Of. la Unión Eur.* **2008**, 16–33.
16. *Reglamento de la Unión Europea 1129/2011*, **2011**.
17. Malik, V. S. and Hu, F. B. Sweeteners and risk of obesity and type 2 diabetes: The role of sugar-sweetened beverages, *Curr. Diab. Rep.* **2012**, *12*, 195–203.
18. Malik, V. S.; Schulze, M. B. and Hu, F. B. Intake of sugar-sweetened beverages and weight gain: A systematic review, *Am. J. Clin. Nutr.* **2006**, *84*, 274–288.
19. Gillis, L. J. and Bar-Or, O. Food away from home, sugar-sweetened drink consumption and juvenile obesity, *J. Am. Coll. Nutr.*, **2003**, *22*, 539–545.
20. Edwards, C. H.; Rossi, M. ; Corpe, C. P.; Butterworth, P. J. and Ellis, P. R. The role of sugars and sweeteners in food, diet and health: Alternatives for the future, *Trends Food Sci. Technol.* **2016**, *56*, 158–166.
21. Kinghorn, A. D. and Compadre, C. M. in *In Alternative sweeteners*, eds. L. O.

- Nabors and R. C. Gelardi, New York: Marcel Dekker, 3rd editio., **2001**, 209–234.
- 22. Hernández-Pérez, A. F.; Jofre, F. M.; De Souza Queiroz, S.; Vaz De Arruda, P.; Chandel, A. K. and Felipe, M. D. G. D. A. Biotechnological production of sweeteners, *Biotechnological Production of Bioactive Compounds*, 2020, 261–292.
 - 23. Bellisle, F. and Drewnowski, A. Intense sweeteners, energy intake and the control of body weight, *Eur. J. Clin. Nutr.* **2007**, *61*, 691–700.
 - 24. Rogers, P. J. The role of low-calorie sweeteners in the prevention and management of overweight and obesity: evidence v. conjecture, *Proc. Nutr. Soc.* **2018**, *77*, 230–238.
 - 25. Belloir, C.; Neiers, F. and Briand, L. Sweeteners and sweetness enhancers, *Curr. Opin. Clin. Nutr. Metab. Care* **2017**, *20*, 279–285.
 - 26. Chauhan, R. Taste Masking: A Unique Approach for Bitter Drugs, *J. Stem Cell Biol. Transplant.* **2017**, *1*, 12.
 - 27. Bharate, S. S.; Bharate, S. B. and Bajaj, A. N. *Interactions and incompatibilities of pharmaceutical excipients with active pharmaceutical ingredients: a comprehensive review*. **2010**, vol. 1.
 - 28. Bharate, S. S.; Bharate, S. B. and Bajaj, A. N. ChemInform Abstract: Interactions and Incompatibilities of Pharmaceutical Excipients with Active Pharmaceutical Ingredients, *ChemInform* **2011**, *42*, 3–26.
 - 29. Srikanth, K.; Priya, K. and Mohan-Gupta, V. R. Natural sweeteners: A complete review, *J. Pharm. Res.* **2011**, *4*, 2034–2039.
 - 30. Chattopadhyay, S.; Raychaudhuri, U. and Chakraborty, R. Artificial sweeteners - A review, *J. Food Sci. Technol.* **2014**, *51*, 611–621.
 - 31. Chen, Z.; Chen, J.; Zhang, W.; Zhang, T.; Guang, C. and Mu, W. Recent research on the physiological functions, applications, and biotechnological production of d-allose, *Appl. Microbiol. Biotechnol.* **2018**, *102*, 4269–4278.
 - 32. Cohn, G. *Die organischen Geschmacksstoffe*, F. Siemenroth, **1914**.
 - 33. Oertly, E. and Myers, R. G. A new theory relating constitution to taste. Simple relations between the constitution of aliphatic compounds and their sweet taste, *J. Am. Chem. Soc.* **1919**, 855.
 - 34. Shallenberger, R. S. The AH,B glycophore and general taste chemistry, *Food Chem.* **1996**, *56*, 209–214.
 - 35. Kodoma, S. Taste, *J. Tokyo Chem.* **1920**, *41*, 495–534.
 - 36. Van Der Wel, H.; Van Der Heijden, A. and Peer, H. G. Sweeteners, *Food Rev. Int.* **1987**, *3*, 193–268.
 - 37. Deutsch, E. W. and Hansch, C. Dependence of relative sweetness on hydrophobic bonding, *Nature* **1966**, *211*, 75.
 - 38. Shallenberger, R. S. and Acree, T. E. Molecular Theory of Sweet Taste, *Nature* **1967**, *216*, 480.
 - 39. Kier, L. B. A Molecular Theory, **1972**, 1394–1397.
 - 40. Shallenberger, R. S. and Agree, T. E. Molecular Structure and Sweet Taste, *J. Agric. Food Chem.* **1969**, *17*, 701–703.
 - 41. Shallenberger, R. S. *Taste Chemistry*, **1993**, 5.
 - 42. Nofre, C. and Tinti, J. M. Sweetness reception in man: The multipoint attachment

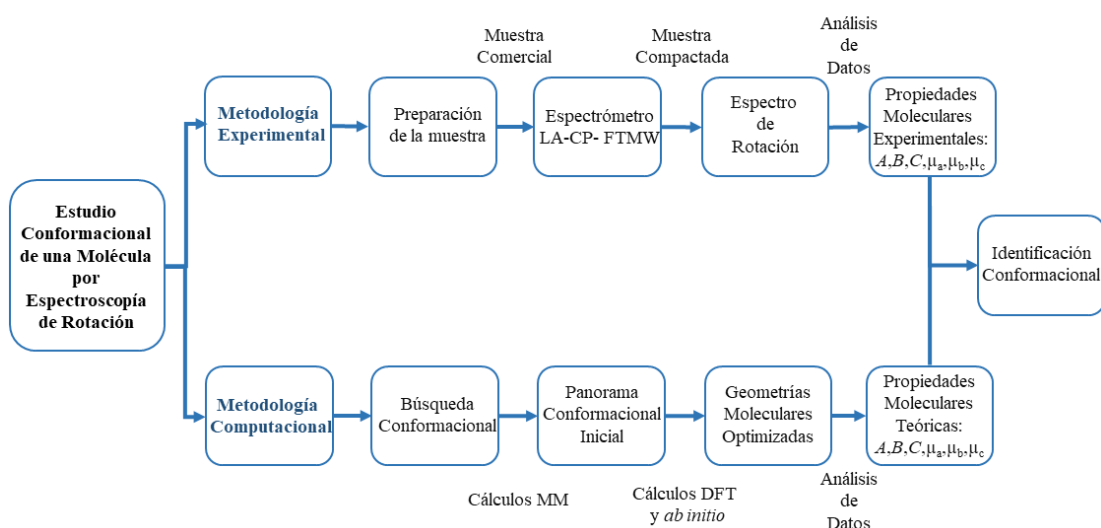
- theory, *Food Chem.* **1996**, *56*, 263–274.
- 43. Bermúdez, C.; Peña, I.; Mata, S. and Alonso, J. L. Sweet Structural Signatures Unveiled in Ketohexoses, *Chem. - A Eur. J.* **2016**, *22*, 16829–16837.
 - 44. E. R. Alonso, I. León, L. Kolesniková and J. L. Alonso, The Structural Signs of Sweetness in Artificial Sweeteners: A Rotational Study of Sorbitol and Dulcitol, *ChemPhysChem.* **2018**, *19*, 3334–3340.
 - 45. Alonso, E.R.; León, I.; Kolesniková, L.; Alonso, J.L. Rotational Spectrum of Saccharin: Structure and Sweetness. *J. Phys. Chem. A* **2019**, *123*, 2756–2761.
 - 46. Clifford, M.N. Chlorogenic acids and other cinnamates - Nature, occurrence and dietary burden. *J. Sci. Food Agric.* **1999**, *79*, 362–372.
 - 47. Li, L.; Shewry, P.R.; Ward, J.L. Phenolic acids in wheat varieties in the healthgrain diversity screen. *J. Agric. Food Chem.* **2008**, *56*, 9732–9739.
 - 48. Nyström, L.; Mäkinen, M.; Lampi, A.M.; Piironen, V. Antioxidant activity of steryl ferulate extracts from rye and wheat bran. *J. Agric. Food Chem.* **2005**, *53*, 2503–2510.
 - 49. Gülcin, I. Antioxidant activity of caffeic acid (3,4-dihydroxycinnamic acid). *Toxicology* **2006**, *217*, 213–220.
 - 50. Agunloye, O.M.; Oboh, G.; Ademiluyi, A.O.; Ademosun, A.O.; Akindahunsi, A.A.; Oyagbemi, A.A.; Omobowale, T.O.; Ajibade, T.O.; Adedapo, A.A. Cardio-protective and antioxidant properties of caffeic acid and chlorogenic acid: Mechanistic role of angiotensin converting enzyme, cholinesterase and arginase activities in cyclosporine induced hypertensive rats. *Biomed. Pharmacother.* **2019**, *109*, 450–458.
 - 51. Spiegel, M.; Gamian, A.; Sroka, Z. A statistically supported antioxidant activity DFT benchmark—the effects of hartree–fock exchange and basis set selection on accuracy and resources uptake. *Molecules* **2021**, *26*.
 - 52. Veeren, B.; Bringart, M.; Turpin, C.; Rondeau, P.; Planesse, C.; Ait-Arsa, I.; Gimé, F.; Marodon, C.; Meilhac, O.; Gonthier, M.P.; et al. Caffeic acid, one of the Major Phenolic Acids of the Medicinal Plant *Antirhea borbonica*, Reduces Renal Tubulointerstitial Fibrosis. *Biomedicines* **2021**, *9*.

2. Metodología

(Methodology)

Las propiedades físicas y químicas de las moléculas dependen directamente de su estructura. Por tanto, es de suma importancia conocer la estructura tridimensional molecular para así obtener un mejor conocimiento de los mecanismos implicados en, por ejemplo, diferentes actividades biológicas. La espectroscopía de microondas es capaz de proporcionar información única de la estructura molecular intrínseca. De hecho, esta técnica nos ofrece detalles sobre los cambios más sutiles, pudiendo distinguir de forma inequívoca entre los confórmeros de los compuestos analizados.

Para llevar a cabo una investigación estructural de esta índole es necesario proceder abordando dos tipos de metodologías: la experimental y la computacional. El diagrama del Esquema 1 muestra una simplificación de ambas vertientes. La parte experimental engloba la preparación de muestras, el manejo instrumental de uno o varios espectrómetros para la adquisición de medidas y el análisis del espectro obtenido. Por otro lado, la parte de metodológica computacional, implica efectuar cálculos de mecánica molecular, lo cual permite obtener el panorama conformacional a muy bajo coste, para posteriormente llevar a cabo cálculos mecánico-cuánticos. Estos nos aportan información sobre el valor energético de cada especie de la molécula, así como constantes de rotación y momentos dipolares eléctricos. La asignación conformacional final se realiza mediante comparación de los parámetros espectroscópicos obtenidos en ambas etapas. En las siguientes secciones se detalla cada etapa.



Esquema 1. Sistemática general en el estudio de la caracterización conformacional de una molécula.

2.1. Metodología experimental

- Preparación de muestra

El estudio experimental de cada una de las moléculas investigadas comienza con la preparación de la muestra. Se parte de entre 0.5 a 1 g de sólido y se pulveriza en un mortero de ágata hasta conseguir un polvo fino que se mezcla con unas gotas de aglomerante comercial para formar una pasta uniforme. A continuación, la pasta se somete a presiones de cerca de 300 MPa con una prensa hidráulica, hasta lograr un cilindro de muestra compactada de aproximadamente 2 cm de largo y 6 mm de diámetro.

- Espectrómetro LA-CP-FTMW

Para esta tesis se usó un espectrómetro denominado como espectrómetro *Laser Ablation Chirped Pulse Fourier Transform Microwave* (LA-CP-FTMW). La Figura 1 muestra la secuencia de operación de dicho espectrómetro [1]. En la primera etapa (1), la muestra sólida se sitúa en un dispositivo motorizado que permite una rotación y traslación constante durante la medición. Con este mecanismo se asegura una vaporización homogénea de la muestra, ya que el láser impacta en lugares diferentes de la barra. De esta forma, cada pulso láser incide sobre la superficie que aún no ha sido ablacionada, haciendo más reproducible el experimento. El láser que se emplea como herramienta de vaporización es un Nd-YAG, el cual opera en el tercer armónico (355 nm) con pulsos de 20 picosegundos de ancho temporal y una energía de 15 mJ por pulso. Las moléculas, una vez en fase gas, son sembradas en el gas portador (neón) y posteriormente se inyectan en el seno de un tanque de alto vacío (10^{-7} mbar sin operar y 10^{-5} mbar durante el pulsado de gas) mediante una válvula pulsada, donde se expanden adiabáticamente [2,3].

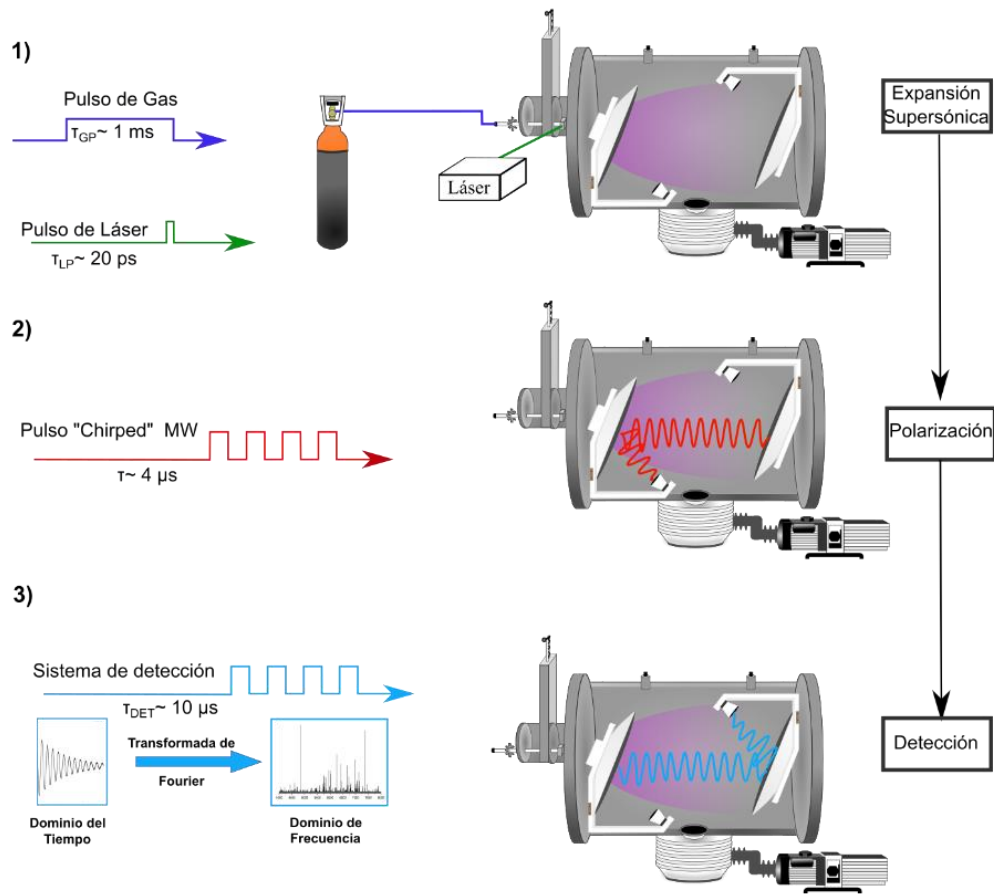


Figura 1. Secuencia de operación del instrumento.

En una segunda etapa (2), un generador de onda arbitrario (AWG) que opera a 24 GS s⁻¹ produce un barrido lineal de frecuencias en un intervalo de microondas dado. El pulso de microondas generado es amplificado mediante un amplificador *Travelling Wave Tube* (TWT) de 300 W, que polariza las moléculas presentes en la expansión supersónica. La polarización macroscópica de las moléculas conlleva una desexcitación de las mismas, produciendo una emisión molecular conocida como *Free Induction Decay* (FID). Este FID es detectado mediante un *Low Noise Amplifier* (LNA) y recogido con un osciloscopio digital de 50 GS/s o 25 GS/s en el dominio del tiempo (3). Del dominio del tiempo pasamos al dominio de frecuencias mediante una transformada de Fourier.

Es importante mencionar que todo el proceso (pulso inicial, válvula de pulsado, AWG, amplificador de microondas, láser de ablación, apertura de la detección y osciloscopio) está sincronizado mediante un oscilador estándar de rubidio de 10 MHz y un generador digital de pulsos (*Digital Delay Generator*). La Figura 2 muestra un esquema general de la secuencia de pulsos.

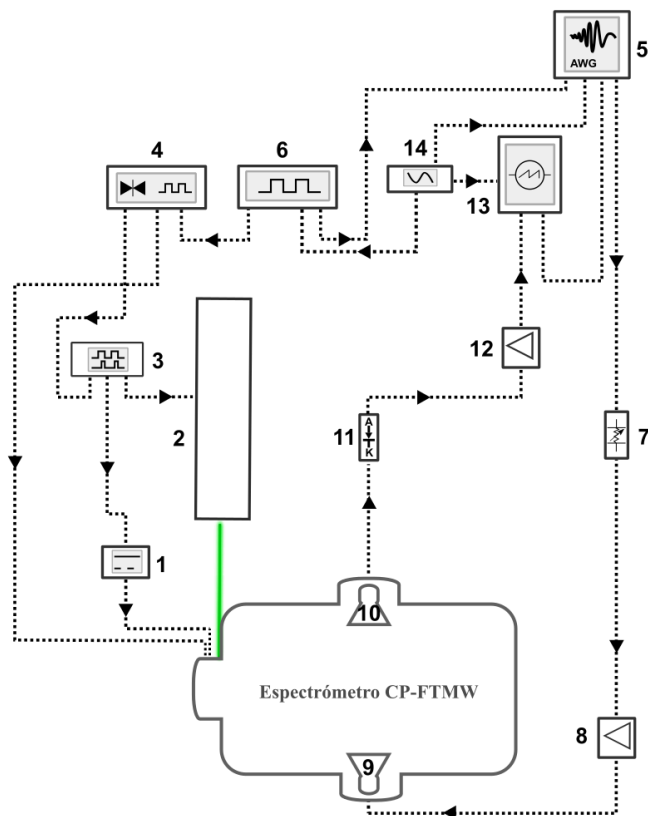


Figura 2. Secuencia de operación del CP-FTMW: (1) Dispositivo que controla el Motor; (2) Láser de Nd-YAG; (3) Generador de pulsos; (4) Válvula Pulsada; (5) Generador de Onda Arbitraria, AWG; (6) Generador digital de pulsos; (7) Atenuador Variable de Polarización; (8) Amplificador TWT; (9-10) Antenas Microondas; (11) Pin de diodo; (12) Amplificador; (13) Osciloscopio Digital; (14) Oscilador Estándar de Rubidio.

Para el estudio de los sistemas moleculares realizados en esta tesis doctoral, se han empleado dos tipos de configuraciones distintas que abarcan distintos rangos: uno de los sistemas está optimizado para medir transiciones de rotación en la zona de 2-8 GHz, mientras que el otro tiene un funcionamiento óptimo en el rango de 6-12 GHz. La secuencia de operación es la misma en ambos y la mayor diferencia radica en el diseño del espectrómetro, además de algunos elementos del sistema de polarización-detección.

La Figura 3 muestra una vista esquematizada de ambos instrumentos de medida. En el instrumento que cubre el rango de 2-8 GHz, se ha utilizado un sistema de polarización de dos antenas de 2-8 GHz ubicadas perpendicularmente a la expansión supersónica. El sistema de detección se basa en un LNA de 2-8 GHz con una figura de ruido de 2 dB. Este espectrómetro es óptimo para moléculas de gran tamaño ya que tienen unas constantes de rotación pequeñas y, por ello, las transiciones de rotación aparecen a menor frecuencia. Como las moléculas estudiadas en esta tesis son de un tamaño medio, el rango es óptimo para medir las transiciones de rotación más bajas.

Con respecto al espectrómetro que cubre el rango de 6-12 GHz, se ha utilizado como sistema de polarización-detección un conjunto de antenas parabólicas (2-32 GHz) situadas coaxialmente a la expansión supersónica y un LNA de 1.7 dB. Este instrumento se ha empleado porque algunas moléculas presentan progresiones de transiciones, mejores en este intervalo.

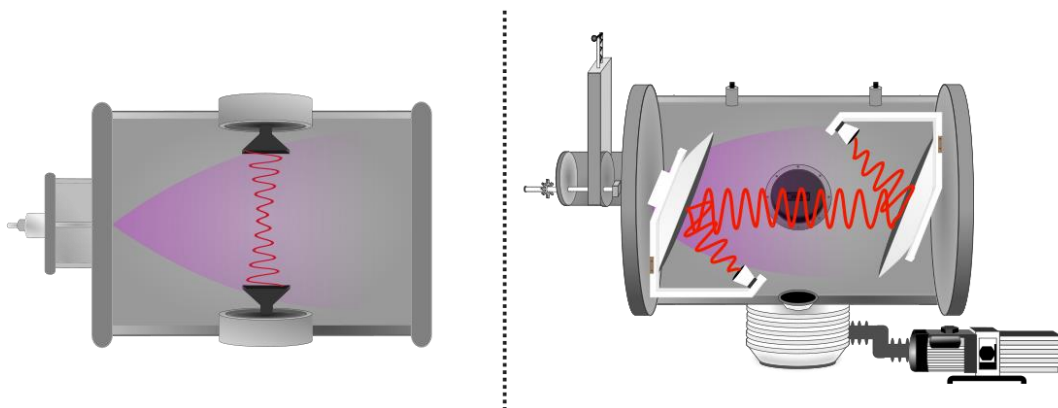


Figura 3. Espectrómetros CP-FTMW: izquierda: vista superior de la configuración de antenas perpendicular al jet supersónico. Derecha: vista frontal del conjunto de antenas parabólicas.

2.2. Metodología Computacional

La metodología computacional es útil de cara al análisis experimental, ya sea para la búsqueda de confórmeros, obtener parámetros estructurales aproximados, entender el alcance de las interacciones inter e intramoleculares, etc. Para este trabajo, emplearemos dos pasos: la obtención de confórmeros mediante mecánica molecular y la optimización de las estructuras mediante cálculos mecano-cuánticos.

- Mecánica Molecular

Las moléculas investigadas en esta tesis son considerablemente grandes por lo que poseen varias torsiones haciéndolas muy flexibles. Esto presenta un problema ya que la exploración de todos los confórmeros, bien examinado todas las posibilidades a mano o bien mediante intuición química, conllevaría una gran cantidad de tiempo además de correr el riesgo de errores (olvidarse de alguna estructura relevante, repetir alguna estructura...). Esto hace que el empleo de tratamientos puramente clásicos sea extremadamente útil para buscar todos los posibles confórmeros. Para ello, se estudian los mínimos de su curva de energía potencial mediante métodos de mecánica molecular.

La superficie de energía potencial de una molécula es una función que representa la relación entre las coordenadas de todos sus núcleos y la energía. Por lo tanto, en cada posición R de los núcleos se puede obtener un valor de energía E (R). La función

E (R) detalla la superficie potencial del sistema. Un confórmero de una molécula es un mínimo de energía local en la superficie de energía potencial, ya que cualquier pequeño cambio en las longitudes o ángulos de enlace da como resultado una energía más alta. La estructura más favorable está representada por el mínimo absoluto. Aparte de los mínimos y máximos de energía se encuentran estados de transición en la superficie de energía potencial en forma de puntos silla.

En esta tesis, la realización de cálculos de mecánica molecular se ha realizado con un *script* de búsqueda conformacional del programa Maestro [4]. Los elementos bases empleados por este *script* durante la búsqueda conformacional son los siguientes: se considera el movimiento nuclear prescindiendo de los electrones; los átomos son masas puntuales unidas mediante enlaces, que son descritos como fuerzas armónicas o elásticas. Así, todas estas interacciones se pueden especificar como funciones de energía potencial, que se parametrizan empíricamente para diferentes tipos de átomos, enlaces, ángulos diedros, etc. La combinación de estas funciones se denomina campo de fuerza y la energía de la molécula surge como resultado de las desviaciones de estos parámetros de los valores ideales [5]. Existen varios campos de fuerza, pero para la realización de este trabajo solamente se han empleado los denominados *Merck Molecular Force Field* (MMFFs) [6] y el llamado *Assisted Model Building with Energy Refinement* (AMBER) [5].

El método MMFFs fue desarrollado para el estudio de compuestos farmacéuticos; principalmente, en aquellos que presentan interacciones no enlazantes como proteínas. Sin embargo, su uso se extendió gracias a sus excelentes resultados cuando se aplica en moléculas orgánicas, como son las que se detallan en este trabajo de investigación. Con respecto, al campo de fuerza AMBER fue parametrizado para un limitado número de moléculas orgánicas y ha sido ampliamente aplicado en biomoléculas y proteínas.

- Cálculos Mecano- Cuánticos

Al basarse en física clásica, las estructuras obtenidas mediante mecánica molecular suelen ser inexactas, al igual que los valores energéticos proporcionados. Por ello, la obtención de todos los confórmeros en el paso previo requiere de una segunda etapa.

Una vez adquirido el paisaje conformacional preliminar de cada molécula, se continúa con las optimizaciones de las geometrías moleculares mediante cálculos mecano-cuánticos. Los resultados obtenidos son de enorme interés, porque nos permite valores energéticos muy precisos de las estructuras de interés, así como sus constantes de rotación y momentos dipolares eléctricos. Para ello, se utiliza el paquete de programas Gaussian 2016, con el que conseguiremos soluciones aproximadas de la ecuación de Schrödinger electrónica [7].

Los niveles de cálculos que se utilizaron para una buena relación entre el coste y la eficacia fueron la Teoría Funcional de la Densidad (DFT), el cual emplea el método funcional B3LYP [8], con las denominadas Dispersiones de Grimme [9] y cálculos *ab initio*, en este caso Møller-Plesset de segundo orden (MP2) [10]. La base que se ha empleado en las dos metodologías es la base 6-311++G(d,p), una de las llamadas bases de Pople [11].

La Teoría Funcional de la Densidad es un método que optimiza la densidad de los electrones, es decir, la energía del estado electrónico fundamental de un sistema se puede determinar mediante la densidad electrónica en lugar de la función de onda. Por otro lado, la metodología MP2 se basa en la resolución de la función de onda y un tratamiento de perturbaciones de segundo orden.

2.3. Fundamentos teóricos

La espectroscopía de rotación se basa en la interacción de la radiación electromagnética con la materia en la región de microondas y cómo ésta produce diferentes transiciones entre los niveles energéticos [12,15]. Estos niveles están descritos por la ecuación de Schrödinger independiente del tiempo, que matemáticamente se expresa como:

$$\hat{H}\Psi = E\Psi \quad (1)$$

En donde Ψ es la función de onda de un determinado nivel energético, E es la energía del estado estacionario y \hat{H} es el operador hamiltoniano, siendo la suma de las energías cinética y potencial del sistema de estudio.

El parámetro más importante en espectroscopía de rotación es el momento de inercia (I), dado que contiene toda la información estructural de la molécula. El momento de inercia se puede escribir mediante la siguiente ecuación:

$$I = \sum_i^{\text{átomos}} m_i \cdot r_i^2 \quad (2)$$

Donde m_i representa la masa del átomo y r_i es la distancia perpendicular del átomo al eje de rotación. De esta manera, cada molécula presenta momentos de inercia en función de la distribución de sus átomos en el espacio. Así, dependiendo de los valores de este parámetro, las moléculas se pueden clasificar como: rotor lineal ($I_a = 0, I_b = I_c$), rotor esférico ($I_a = I_b = I_c$), rotor simétrico *oblate* ($I_a = I_b < I_c$), rotor simétrico *prolate* ($I_a < I_b = I_c$) y rotor asimétrico ($I_a < I_b < I_c$).

Si consideramos la rotación de un cuerpo rígido mediante un enfoque mecano-cuántico, la energía cinética descrita por el hamiltoniano se expresa en términos del momento angular y queda definida como:

$$\hat{H} = \frac{\hat{P}_a^2}{2I_a} + \frac{\hat{P}_b^2}{2I_b} + \frac{\hat{P}_c^2}{2I_c} \quad (3)$$

En esta ecuación, se introducen las constantes de rotación A , B y C , dado que estos valores son a los que se puede acceder directamente desde el espectro de microondas. Por tanto, el hamiltoniano se reescribe como:

$$\hat{H} = \left(\frac{4\pi^2}{\hbar}\right)(A\hat{P}_a^2 + B\hat{P}_b^2 + C\hat{P}_c^2) \quad (4)$$

Para moléculas asimétricas se utilizan aproximaciones que consideran casos límites de niveles de energía para moléculas trompo simétrica “achatada” (molécula *oblate*) y trompo simétrica “alargada” (molécula *prolate*). Las funciones de onda para este caso, se expresan como combinación lineal de las funciones propias del trompo simétrico. De esta manera, la ecuación de Schrödinger nos permite calcular la energía de los autovalores del hamiltoniano. En el caso de una molécula *oblate* se escribe como:

$$E = BJ(J+1) + (C - B)K^2 \quad (5)$$

Mientras que para una molécula *prolate* se define mediante la ecuación:

$$E = BJ(J+1) + (A - B)K^2 \quad (6)$$

La energía de los autovalores está descrita en unidades de frecuencia, J es el número cuántico momento angular, mientras que K es la proyección del número cuántico J , el cual puede adoptar dos valores: uno en el límite prolate (K_{-1}) y otro en el límite oblate (K_1).

De este modo, usando las ecuaciones 5 y 6 podemos obtener los valores de los diferentes niveles de energía para las moléculas, que se ejemplifica mediante el diagrama de correlación (Figura 4). Además, para cuantificar lo lejos que se encuentra una molécula de cualquiera de los dos rotores simétricos, se suele emplear el parámetro de asimetría de Ray. Este indicador se calcula de la siguiente manera:

$$k = \frac{(2B - A - C)}{A - C} \quad (7)$$

Donde k es el parámetro de asimetría. Cuando éste tiende a -1, la molécula presenta simetría *prolate*; mientras que si k tiende a +1, tiene simetría *oblate*. Finalmente, si k es cero, la molécula es totalmente asimétrica (Figura 4). En general, podemos considerar que las moléculas *oblate* o *prolate* son un caso especial de rotor simétrico.

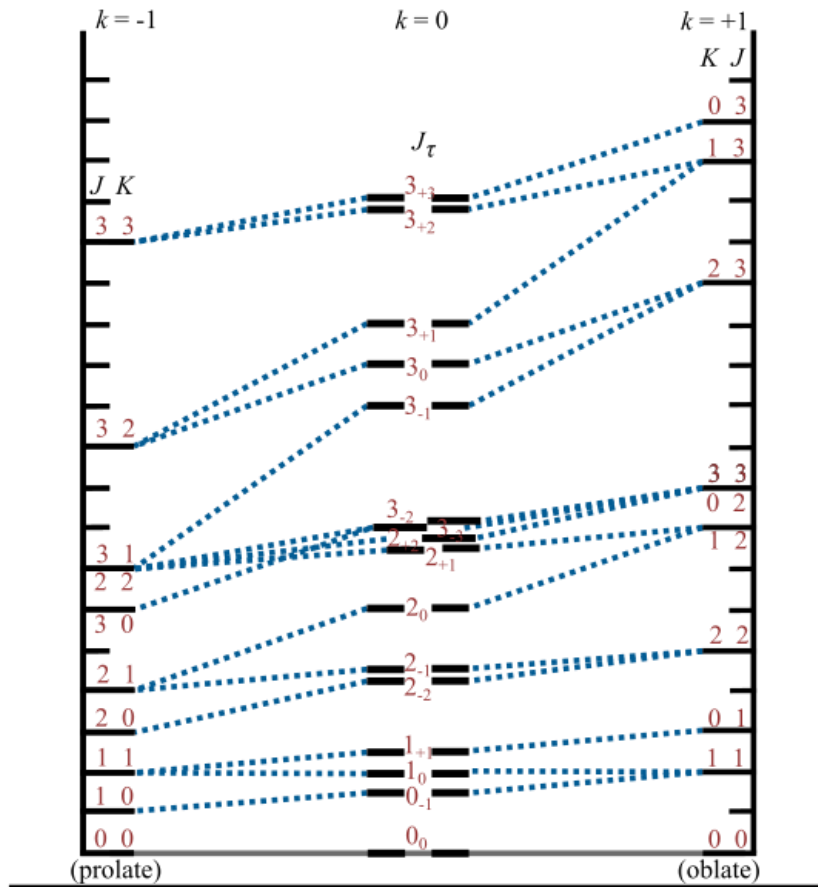


Figura 4. Diagrama de correlación [12].

Las transiciones no se producen al azar y dependen totalmente del tipo de asimetría de la molécula. Estas transiciones, por tanto, están totalmente ligadas a reglas. Estas reglas de selección varían con el tipo de rotor. La condición más importante para que esté permitida una transición es que el valor de la integral de transición sea diferente de cero. Esta integral nos proporciona información sobre la probabilidad que se produzca una transición entre un estado de partida (Ψ'') y un estado de llegada (Ψ'), lo cual se expresa como:

$$\mu_r = \int \Psi' \mu \Psi'' d\tau \quad (8)$$

Las moléculas de estudio de esta tesis son moléculas asimétricas, y debemos considerar sus tres ejes de inercia, lo que conlleva la existencia de las tres componentes

del momento dipolar eléctrico (μ_a , μ_b y μ_c). Como consecuencia, existen distintos tipos de transición: tipo *a*, tipo *b* y tipo *c*.

Otra regla de selección esencial para que una transición esté permitida está relacionada con la variación del número cuántico J . J puede presentar valores de $J = \pm 0,1$, es decir solo pueden ocurrir transiciones en un solo nivel. Cuando J no varía, es necesario que cambie K_{-1} o K_{+1} . No obstante, si J difiere en $\Delta J = \pm 1$, sus pseudonúmeros cuánticos pueden cambiar o no. Cada una de estas posibilidades da lugar a diferentes transiciones que se denominan ramas:

$$\begin{aligned}\Delta J = 0 & \text{ Rama Q} \\ \Delta J = -1 & \text{ Rama P} \\ \Delta J = +1 & \text{ Rama R}\end{aligned}$$

Finalmente, en función del tipo de transición existirán diferentes tipos de restricciones en K_{-1} y K_{+1} . Se resumen en la Tabla 1.

Tabla 1. Se detalla los diferentes valores que pueden tener K_{-1} y K_{+1} en función del momento dipolar eléctrico.

Momento dipolar	ΔK_{-1}	ΔK_{+1}
$\mu_a \neq 0$	$0, \pm 2$	$\pm 1, \pm 3$
$\mu_b \neq 0$	$\pm 1, \pm 3$	$\pm 1, \pm 3$
$\mu_c \neq 0$	$\pm 1, \pm 3$	$0, \pm 2$

Estas transiciones permitidas o prohibidas se deducen mediante el producto directo de la representación irreducible simétrica de los elementos de la integral momento de transición ($\Gamma(\psi') \otimes \Gamma(\mu_{a,b,c}) \otimes \Gamma(\psi'')$), que ha de contener la representación totalmente simétrica.

- Distorsión centrífuga

El modelo del rotor rígido describe de manera fiable la rotación de las moléculas. No obstante, las moléculas reales no son rígidas. Los sistemas moleculares presentan distorsiones durante la rotación, los cuales modifican la distancia y ángulos de enlace. Este fenómeno se produce por las fuerzas centrífugas que actúan sobre las moléculas. Este efecto es muy pequeño, pero es necesario considerar un rotor semirrígido en muchas moléculas, especialmente cuando trabajamos con J altos.

Estas constantes de distorsión suelen tener órdenes de kHz y cuando se aplican, el hamiltoniano de la molécula se describe como la suma del hamiltoniano rígido y el hamiltoniano de distorsión:

$$\hat{H} = H_r + H_d \quad (9)$$

En este trabajo fue necesario emplear el parámetro de distorsión en algunas de las moléculas caracterizadas.

2.4. Software empleado

Después de obtener el panorama conformacional de cada una de las especies con las propiedades de interés espectroscópico, se comienza el análisis del espectro obtenido experimentalmente. Esta tarea se puede llevar a cabo gracias a dos herramientas de análisis de rotación: JB95 [13] y SPCAT/SPFIT [14]. En estos programas, las transiciones observadas se ajustan utilizando un hamiltoniano que describe la rotación de la molécula. Las frecuencias que aparecen en el espectro experimental corresponden a la diferencia de energía entre dos niveles de energías de rotación de las moléculas de estudio. Estos niveles de energía son autovalores del operador hamiltoniano, el cual usualmente es expresado en términos del momento angular. Los autovalores resultantes pueden ser constituidos desde la combinación lineal de las tres constantes de rotación A , B y C , las cuales están directamente relacionadas con la distribución de masa de la molécula. Estas constantes son inversamente proporcionales a los momentos de inercia (I_a , I_b y I_c), que se obtienen como resultado del producto de cada masa del sistema multiplicado con los ejes siendo estos a , b y c . Así, estos valores de las constantes de rotación son únicos para cada geometría molecular estudiada [12,15]. De esta manera, si se analiza una pequeña sección del espectro y se tienen las constantes de rotación, posteriormente, se puede identificar todas las transiciones que están contenidas en éste y, finalmente, hallar cada confórmero del paisaje conformacional responsable de las transiciones de rotación.

2.5. Referencias

1. Alonso, E.R. Biomolecules and Interstellar Molecules: Structure, Interactions and Spectroscopic Characterization. Ph .D. Thesis, Universidad de Valladolid, Valladolid, Spain, **2018**.
2. Miller, D. R.; Scoles, G.; Bassi, D.; Buck, U.; Laine, D. C. *Atomic and Molecular Beam Methods*, Oxford Univ. Press: **1988**.
3. Hollas, J. M., *Modern Spectroscopy*, 4th Edition; John Wiley & Sons: **2004**.
4. Schrödinger Release 2018-3; Maestro Schrödinger, LLC: New York, NY, USA, **2018**.
5. C. I. Bayly *et al.*, A Second Generation Force Field for the Simulation of Proteins, Nucleic Acids, and Organic Molecules. *J. Am. Chem. Soc.* **1995**, *117*(19), 5179–5197.
6. Halgren, T. A., Merck Molecular Force Field. 11. MMFF94 van der Waals and Electrostatic Parameters for Intermolecular Interactions. *J. Comput. Chem.* **1995**, *17*, 520-552.
7. Frisch, M.J.; Trucks, G.W.; Schlegel, H.B.; Scuseria, G.E.; Robb, M.A.; Cheeseman, J.R.; Scalmani, G.; Barone, V.; Petersson, G.A.; Nakatsuji, H.; et al. *Gaussian 16*; Revision B.01 2016; Gaussian, Inc.: Wallingford, CT, USA, **2016**.
8. Becke, A.D. A new mixing of Hartree–Fock and local density-functional theories. *J. Chem. Phys.* **1993**, *98*, 1372–1377.
9. Grimme, S.; Antony, J.; Ehrlich, S.; Krieg, H. A consistent and accurate ab initio parametrization of density functional dispersion correction (DFT-D) for the 94 elements H-Pu. *J. Chem. Phys.* **2010**, *132*, 154104.
10. Møller, C.; Plesset, M.S. Note on an approximation treatment for many-electron systems. *Phys. Rev.* **1934**, *46*, 618–622.
11. Frisch, M.J.; Pople, J.A.; Binkley, J.S. Self-consistent molecular orbital methods 25. Supplementary functions for Gaussian basis sets. *J. Chem. Phys.* **1984**, *80*, 3265–3269.
12. Gordy, W.; Cook, R. L. *Microwave Molecular Spectra*, 3rd ed.; Wiley: **1984**.
13. Plusquellec, D. F. *JB95 Spectral Fitting Program*;NIST: Gaithersburg, MD. <http://www.nist.gov/pml/electromagnetics/grp05/jb95.cfm>.
14. Pickett, H. M. The Fitting and Prediction of Vibration-Rotation Spectra with Spin Interactions. *J. Mol. Spectrosc.* **1991**, *148* (2), 371–377.
15. Kroto, H. W. *Molecular Rotation Spectra*, Dover, **1992**.

Resultados

(Results)

In the following, we present the results divided into four chapters: Chapters 3 to 5 include the results obtained for the molecules perceived as sweet: perillartine, allose, and dulcin, respectively. Chapter 6 deals with the study of caffeic acid, an additive.

All the chapters follow a similar structure: First, an introduction of the interest of the molecule is given. Then, the results and discussion obtained for each molecule is detailed. Afterwards, the conclusions obtained for each system follows. Finally, the selected bibliography is highlighted.

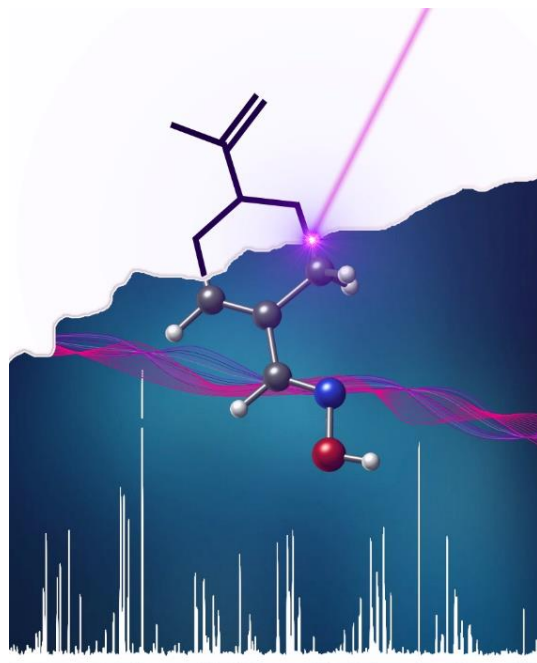
Each chapter has its own annex, collected at the end of this thesis dissertation. Thus, the annexes of Chapters 3 to 6 correspond to Annex I to IV, respectively.

3. Chapter

Rotational Spectrum and Conformational Analysis of Perillartine: Insights into the Structure–Sweetness Relationship

Adapted from: *Molecules*, 2022, 27(6), 1924.

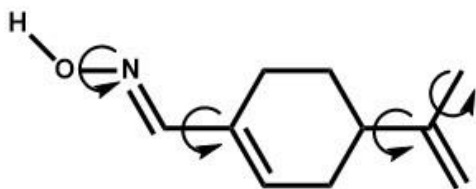
Abstract: In this chapter, high-resolution rotational spectroscopy coupled to a laser ablation source is used to study the conformational panorama of perillartine, a solid synthetic sweetener. Four conformers are identified under the isolation conditions of the supersonic expansion. The results show that all the conformers present an *E* configuration of the C=N group with respect to the double bond of the ring. The observed structures are verified against Shallenberger–Acree–Kier’s sweetness theory to shed light on the structure–sweetness relationship for this particular oxime, highlighting a deluge of possibilities to bind the receptor.



3.1. Introduction

Human's attraction for sweetness is so strong that modern diet has a strong dependence on sugar. This fact has contributed to the obesity and several diseases associated with this condition, reason why some specialists suggest promoting healthier options such as the consumption of sweeteners [1–3]. A sweetener is defined as a food additive that provides a sweet taste similar to sugar, and can be classified according to their origin as natural or artificial sweeteners. For example, carbohydrates are the most important family of the former, whereas saccharin could be mentioned as the most representative of the latest [4,5]. The challenge of the food manufacturers is to develop low or calorie-free products without compromising the real taste of sugar expected by consumers. However, finding new sweeteners is not an easy task and it usually requires a deep understanding about the sweet perception of compounds in humans, i.e., how these sweeteners interact with the receptors. Therefore, obtaining the precise 3D structure of sweeteners is isolation conditions to find a plausible answer to the long-sought question of why these molecules are perceived as sweet [6–9] is fundamental.

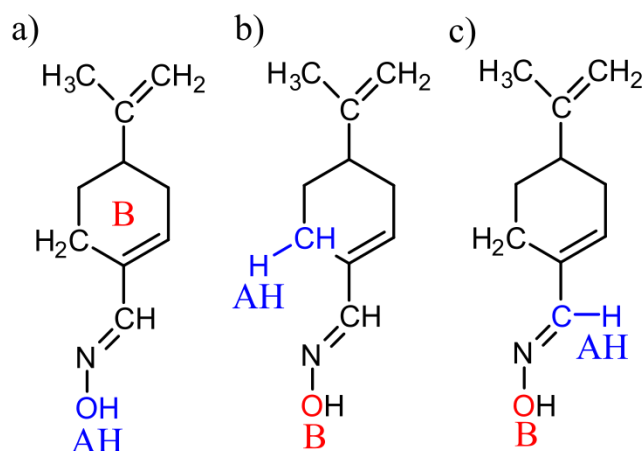
The first sweeteners analyzed were some natural sweeteners such as fructose or tagatose among others [10,11]. Subsequently, the study was extended to different polyols such as dulcitol and sorbitol [12], and the research was continued with one of the oldest synthetic sweeteners, namely saccharin [13]. To further rationalize the theory of sweetness and to extend it to sweeteners involving functional groups different than those of the molecules mentioned above and, given the enormous importance on the continuing search for better nonfattening sweetening agents and artificial flavoring, we have investigated perillartine. This synthetic sweetener is especially attractive given its intense sweet taste, approximately 2000 times larger than sucrose [14]. This peculiar molecule, which is easily obtained by the oximation of perillyl aldehyde, is an oxime containing a cyclohexene where the double bond is conjugated with the C = N double bond, as shown in Scheme 1. Perillartine is used commercially in Japan to sweeten tobacco, but it lacks further applications due to its low solubility and a lingering 'metallic' taste [1].



Scheme 1. Molecular sketch of perillartine highlighting its torsional degrees of freedom, which can give rise to several conformers.

It is worth noticing that this compound exhibits several possibilities for the *AH* and *B* units [15]. Shallenberger & Acree initially suggested that the hydroxyl moiety could correspond to the *AH* point, and the delocalized cloud of the ring was proposed as the *B* point (see Scheme 2a). Later on, Kier selected one of the hydrogen atoms in the *ortho* position with respect to the oxime group as the *AH* point, and the hydroxyl oxygen as *B*. The latter is schematized in Scheme 2b and is in good accordance with several studies of

oxime derivatives of perillartine [9, 16,17]. Alternatively, Heijden et al. [18] proposed that both *AH* and *B* identities are located within the oxime (Scheme 2c). Although some studies have been carried out on perillartine and its analogues [16,19–21] such as the analysis of electrostatic potentials [22], which details the importance of two potential regions to determine the *AH-B* system, the three-dimensional structure has never been specified. Consequently, it has not been possible to verify the characteristic points of the sweetness theory. In another attempt to corroborate ‘the triangle of sweetness’, the structure of perillartine was characterized by X-rays [23]. However, the detailed arrangement of the atoms is distorted in the condensed medium.



Scheme 2. A simplified scheme of the different identifications of the *AH* and *B* units suggested for the structures of oximes [15].

In this context, we have performed the first rotational spectroscopic study of perillartine using Laser Ablation Chirped Pulse Fourier Transform Microwave (LA-CP-FTMW) spectroscopy to identify the most relevant conformers of this sweetener. The results obtained will be compared with the Shallenberger-Acree-Kier’s sweetness theory.

3.2. Results and Discussion

Conformational panorama

Twelve conformers of perillartine have been predicted using the B3LYP-GD3/6-311++G(d,p) methodology (see Figure 1) [24–26] and can be categorized into different groups depending on the position of the allyl and oxime groups. The six most stable structures have a *trans* configuration between the C=N group and the double bond in the ring, also known as *E* (*entgegen*), and with the oxime group in an *anti* disposition. This disposition gives the molecule a greater stability as all the structures with such configuration are below 1000 cm⁻¹. Among the least stable structures, four of them have a *cis* arrangement of the C=N group with respect to the double bond in the ring, also known as *Z* (*zusammen*), and the two least stable structures are in a *E* configuration but with the oxime group in a *sin* disposition. Within all these possibilities, starting from

conformer 5, all of them have relative energies larger than 500 cm^{-1} and are not expected to be observed in a supersonic expansion.

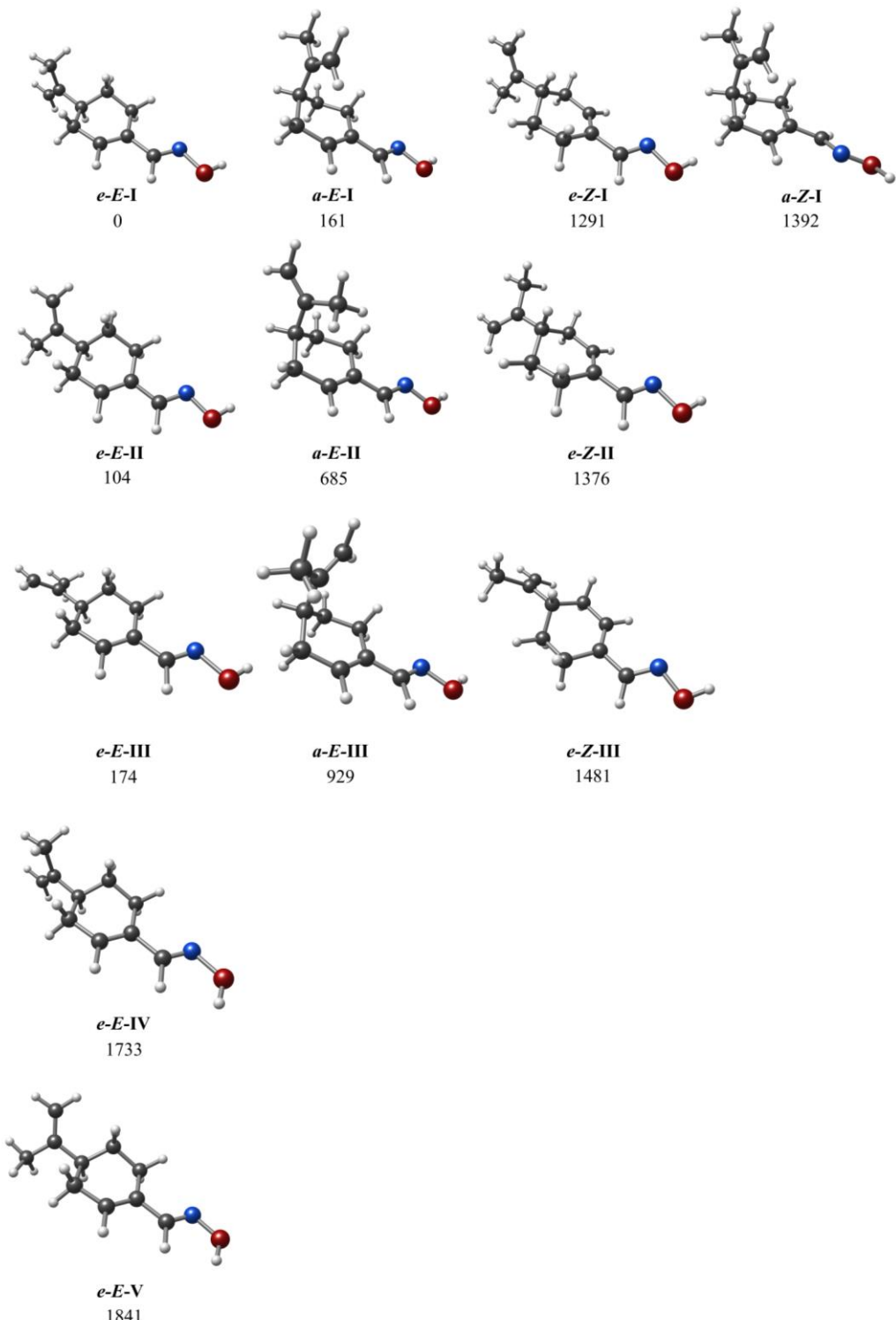


Figure 1. The predicted lowest-energy conformers of perillartine below 2000 cm^{-1} relative to the global minimum. Relative energies are given in cm^{-1} .

Broadband rotational spectrum

The broadband microwave spectrum of perillartine between 2.4 and 8.0 GHz is shown in Figure 2. The rotational spectrum exhibits a high density of lines suggesting the presence of several rotamers. In a first step, we removed the known photofragmentation products from the spectra [27–29]. Subsequently, we turned our attention to the calculated most energetically-stable conformers. As can be seen in Table 1, four structures are below 200 cm⁻¹ and are expected to be in our experiment due to their stability. This is in good agreement with the numerous rotational lines observed in the spectrum. Additionally, Table 1 shows that the geometries of all the conformers are nearly prolate asymmetric rotor, with a non-zero μ_a electric dipole moment. This facilitates our analysis due to the characteristic pattern of appearing at a regular $B + C$ spacing being easily recognizable. Using this strategy, we located intense transitions corresponding to an approximate spacing of $B + C \sim 750$ MHz. An illustration of such characteristic pattern is shown in Figure 2. We first used the JB95 program to match the predicted spectrum with the experimental one [30], and a preliminary set of rotational constants was obtained. These new values of the rotational constants allowed us to refine the search and to expand the number of adjusted transitions. A total of 27 transitions were measured and fitted using a rigid rotor Hamiltonian [31] through Pickett's SPFIT / SPCAT program [32]. The resulting rotational constants for the first rotamer are shown in Table 2. Despite extensive exploration, no (*b*- or *c*- type) transitions were observed in the spectrum indicating that the dipole moment along these two axes must be low or zero.

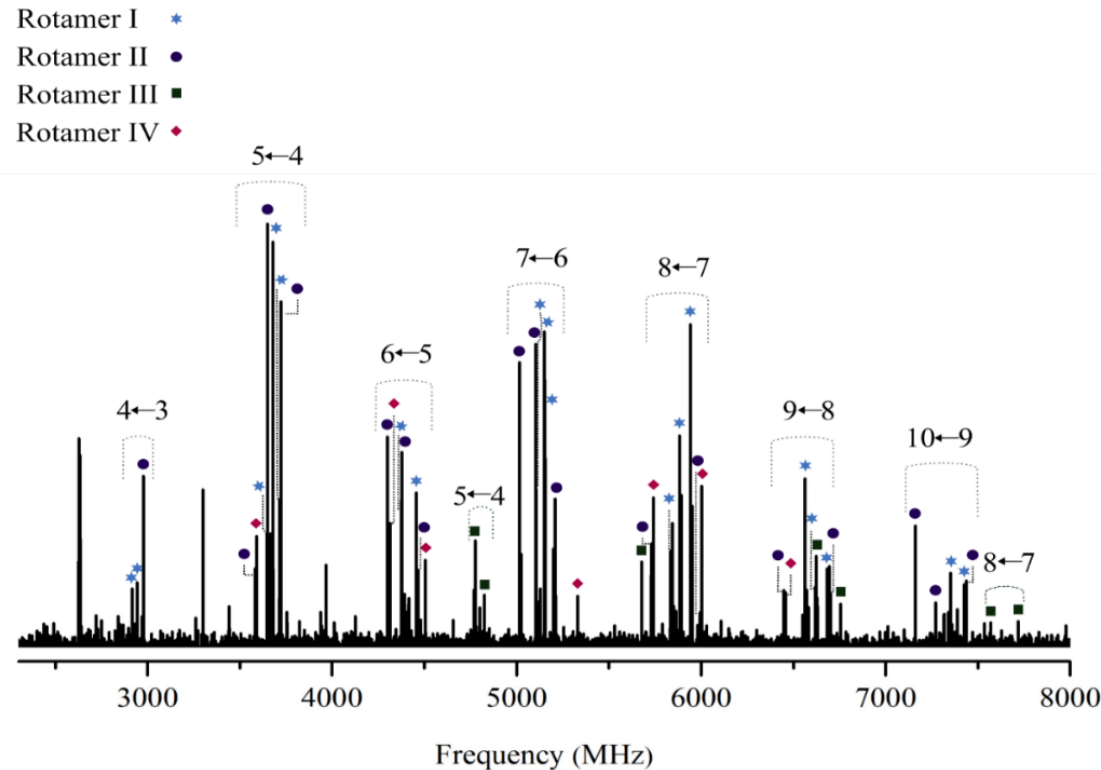


Figure 2. Broadband rotational spectrum of perillartine in the 2400 to 8000 MHz range. Some selected *a*-type transitions are highlighted for all assigned species.

In a second step, we removed the rotational lines from the assigned rotamer I and continued searching for other conformers. Using the same procedure, recognition of a second spectral signature was straightforward due to the high intensity of another progression with a similar spacing as that observed for rotamer I (see Figure 2). It should therefore correspond to another conformer. Initially, a total of 26 *a*-type transitions were added to the fit. Subsequently, the rotational constants obtained were used to refine the search, and look for *b*- or *c*- type transitions. However, similarly to rotamer I, no *b*- or *c*-type transitions were observable. The values of the rotational constants of rotamer II obtained after the fit are listed in Table 2.

Table 1. Theoretical spectroscopic parameters for the detected conformers of perillartine.

	<i>e-E-I</i>	<i>e-E-II</i>	<i>a-E-I</i>	<i>e-E-III</i>
<i>A</i> ^[a]	2904	2930	1834	2831
<i>B</i>	374	378	478	382
<i>C</i>	360	350	461	351
$ \mu_a ^{[b]}$	1.0	1.1	1.4	1.0
$ \mu_b $	0.0	0.4	0.2	0.3
$ \mu_c $	0.4	0.2	0.7	0.2
$\Delta E^{[c]}$	0	109	113	185
$\Delta E_{ZPE}^{[d]}$	0	104	161	174

[a] *A*, *B*, and *C* represent the rotational constants (in MHz). [b] μ_a , μ_b and μ_c are the electric dipole moment components (in D). [c] Relative energies (in cm⁻¹) with respect to the global minimum. [d] Relative energies (in cm⁻¹) with respect to the global minimum, taking into account the zero-point energy (ZPE).

Using the same strategy, we removed the lines of the second identified rotamer and searched for other rotamers. Despite its low intensity, we found another two rotamers showing weak progressions. For rotamer III, we measured a total of 11 *a*- type transitions, while for rotamer IV a total of 15 *a*-type transitions were fitted. None of the rotamers showed *b*- or *c*-type transitions. After removing the transitions of these two new rotamers no lines remained in the spectrum indicating that there are no more conformers populated enough after the supersonic expansion to be detected. The resulting rotational constants for the four conformers observed in the experiment are listed in Table 2, while all the lines for the identified species are collected in the Annex I (Tables AI-1 to AI-4).

Conformational identification

The assignment of the rotamers to the corresponding calculated conformer was straightforward thanks to the good consistency between the theoretical and experimental spectroscopic parameters, particularly taking into account the close similarity of the *B* and *C* rotational constants. It can be easily seen in Tables 1 and 2 that rotamers I, II, III and IV correspond to structures *e-E-I*, *e-E-II*, *a-E-I* and *e-E-III*, respectively. Another factor that is in agreement between the calculated values and the experimental observations is the absence of *b*- and *c*- type transitions for all rotamers. This is in good agreement with the predicted dipole moment along these axes for all the conformers. This means that these transitions should be either very weak or non-existence in the rotational

spectrum, particularly when taking into account that they are directly proportional to the dipole moments μ^2 in the broadband spectrum.

Table 2. Experimental spectroscopic parameters for the detected conformers of perillartine.

	ROT. I	ROT. II	ROT. III	ROT. IV
$A^{[a]}$	2893.8(51) ^[e]	2914.31(88)	1776.1(79)	2823.8(13)
B	374.7401(11)	379.22485(83)	487.2553(28)	383.84430(70)
C	361.2711(11)	351.56166(81)	468.6639(29)	351.03516(62)
$ \mu_a ^{[b]}$	Observed	Observed	Observed	Observed
$ \mu_b $	-	Observed	-	-
$ \mu_c $	-	-	-	-
$\sigma^{[c]}$	26	19	31	24
N ^[d]	27	26	11	13

[a] A , B , and C represent the rotational constants (in MHz). [b] μ_a , μ_b and μ_c are the electric dipole moment components. [c] RMS deviation of the fit (in kHz). [d] Number of measured transitions. [e] Standard error in parentheses expressed in units of the last digit.

The detected structures, which are also the most stable ones, are shown in Figure 3. The main difference between the four main conformers is that structures e -E-I, e -E-II, and e -E-III have the allyl group in an *equatorial* position, while structure a -E-I has the allyl group in an *axial* position. It is worth noting that calculations using the MP2 level [33] also predicts the same four structures as the most stable structures but with structure 3 as the global minimum (see Table AI-5) . This fact is interesting as it let us to benchmark current methodologies.

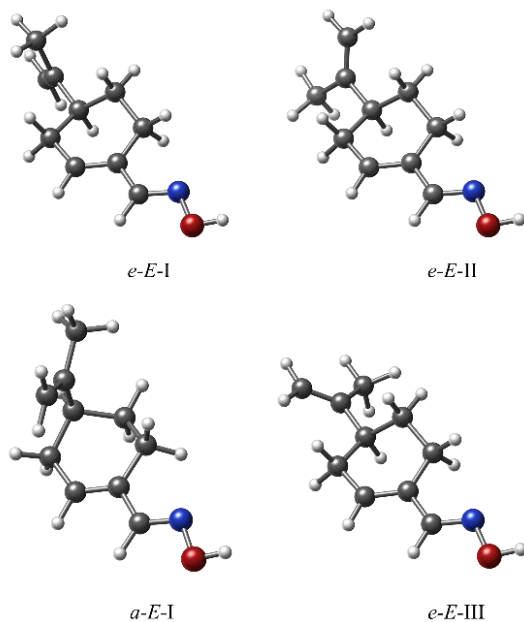


Figure 3. The calculated structures for the four detected species of perillartine. All the observed species have a *trans* configuration of the C=N group with respect to the double bond in the ring and differ in the orientation of the allyl group in either equatorial (structures e -E-I, e -E-II and e -E-III) or axial position (structure a -E-I).

Using selected transitions of the experimental results we can estimate the relative populations of the conformers. Only estimated the relative populations of conformers *e-E-I* and *a-E-I* will be discussed as, due to a possible conformational interconversion between structures *e-E-II* and *e-E-III* (see Figure 4), their population is altered from the original one. Fortunately, the interconversion barrier between structures *e-E-I* and *a-E-I* is large enough to preclude any conformational interconversion and its population is not affected by other conformers. Thus, we can use this information to benchmark the different levels of theories and test which one is correct in the evaluation of the energies. Our estimations based on intensity measurements, which is also evident by a simple look at the experimental spectrum (see Figure 2), set structure *e-E-I* as the global minimum with the *a-E-I* structure at $\sim 100\text{-}200\text{ cm}^{-1}$ higher in energy. Therefore, B3LYP-GD3 gives a better description of the energetics. Finally, we would also like to highlight the importance of adding Grimme Dispersions as the calculations without their inclusion estimate structure *a-E-I* being too high in energy, at 560 cm^{-1} , which would result in a low population of this conformer precluding its detection. The conformational panorama of this molecule is another illustrative case of the robustness of rotational spectroscopy, not only for a definitive structural characterization, but also to contrast and validate the results provided by high-level computational chemistry.

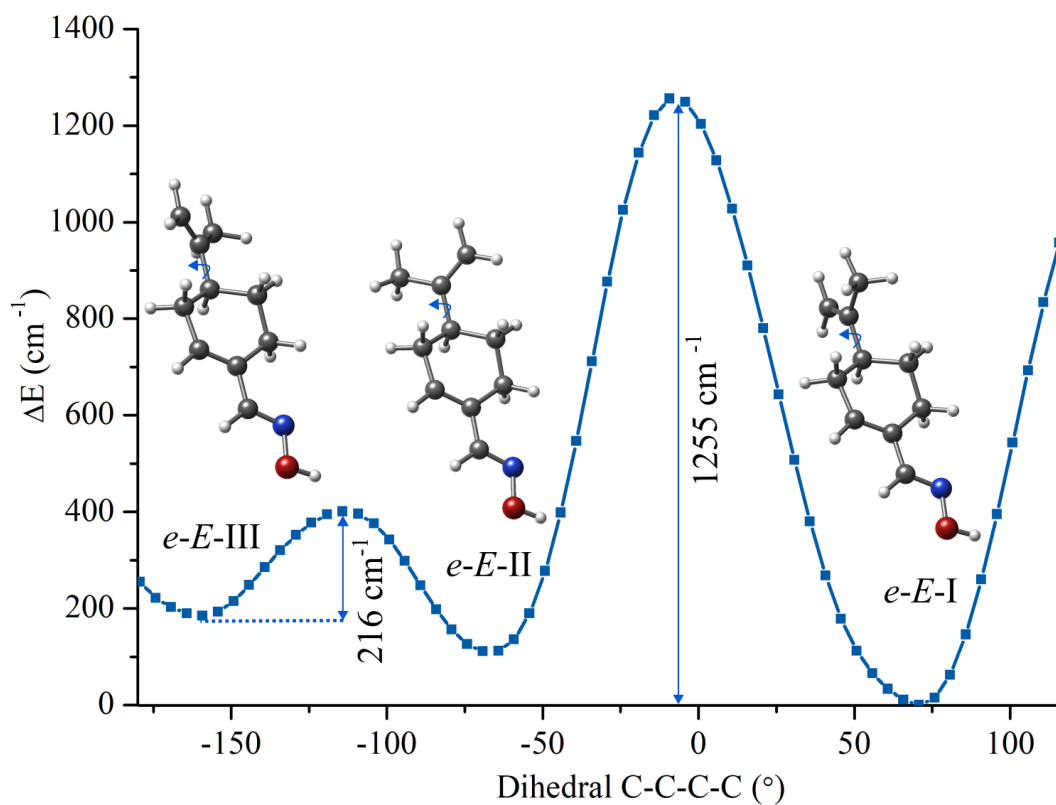


Figure 4. Relaxed Potential Energy Surface scan (PES) between the *e-E-III* / *e-E-II* / *e-E-I* conformers of perillartine computed at the B3LYP-GD3/6-311++G(d,p) level, varying the $\text{CH}_2\text{-C-C-CH}_3$ torsion (as indicated with an arrow).

Internal rotation

Perillartine has a methyl group. Nevertheless, we did not find any sign of internal rotation, meaning that the barrier for this internal motion must be large. In order to confirm it, we estimated the barrier height for the internal rotation of the methyl group. The obtained value for the barrier height is $\sim 550 \text{ cm}^{-1}$ and, therefore, no rotational splitting is expected (see Figure 5), confirming our experimental observation.

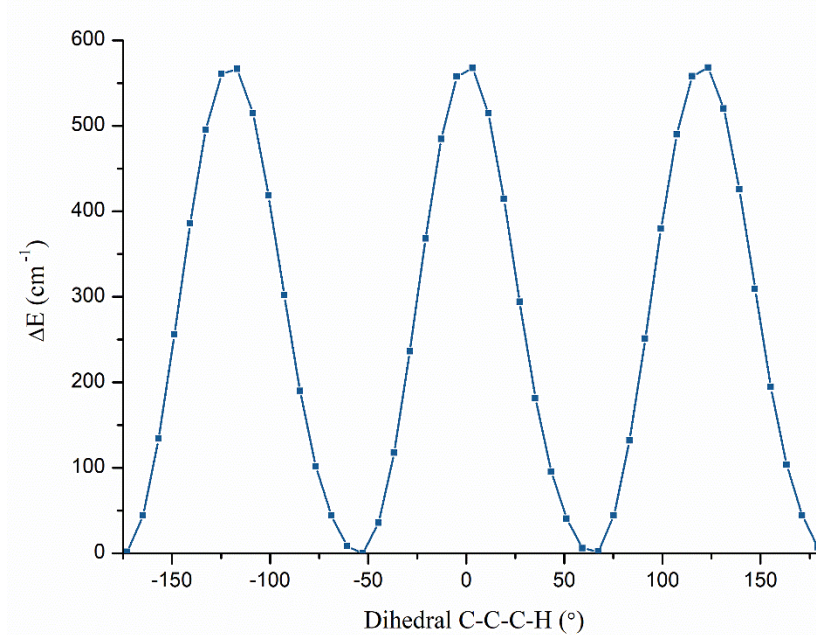


Figure 5. Potential Energy Scan (PES) rotating the methyl group, i.e. the C-C-C-H dihedral angle, of structure *e-E-I*. The barrier height is $\sim 550 \text{ cm}^{-1}$ and, therefore, no splitting is expected due to internal rotation.

Structure-property relationship

Once the structures of perillartine have been discussed, we proceed to compare the geometries of the detected conformers with that of the sweetness theory. We will use the most stable structure as the heart of discussion, because the main conclusions can be extended to all the four structures. It has been proposed [9] that the nitrogen atom corresponds to the proton acceptor point (*B*), while the ring's C-H opposed to the C=C motif is the donor group (*A-H*) since it is an electropositive site of the molecule. The third contact point (γ) should correspond to the allyl group since it is a hydrophobic zone. Figure 6 shows a sketch of the proposed sweetness triangle, i.e. the glucophore tripartite, for the most stable structure, together with its calculated distances for the main contact points. We also note that the γ point is not a point but a region. In fact, this hydrocarbon section is important and can vary drastically as shown for perillartine analogues [22]. As can be seen, the distances agree well with those postulated in the sweetness theory. Interestingly, the Non-Covalent Interaction plot (*NCI plot*) [34] in Figure 6, highlights that the main

points suggested as the “sweetness triangle” are also those involved in the strongest intramolecular interactions. It makes sense that those functional groups involved in the strongest intramolecular interactions would also result into the strongest intermolecular interactions with the receptor.

Needless to say, the same can be applied to the four conformers of perillartine. It is important to note that, for a molecule to be sweet, not only it is the interaction between the molecule and the receptor that needs to be taken into account, but also additional factor such as the propensity of the molecule to “reach” (solvent interactions) or “fit” (molecular size) in the receptor. Interestingly, the axial and equatorial dispositions of perillartine are considerably different allowing more diversity to fit in the receptor. Additionally, the several conformers in the axial position, which some of them may be interconverting continuously at room temperature, gives perillartine several shapes increasing the chance to fit in the receptor, as is they were slightly different pieces of a puzzle. Altogether, these properties could increase the chance of perillartine to interact with the receptor making it a particular sweet molecule.

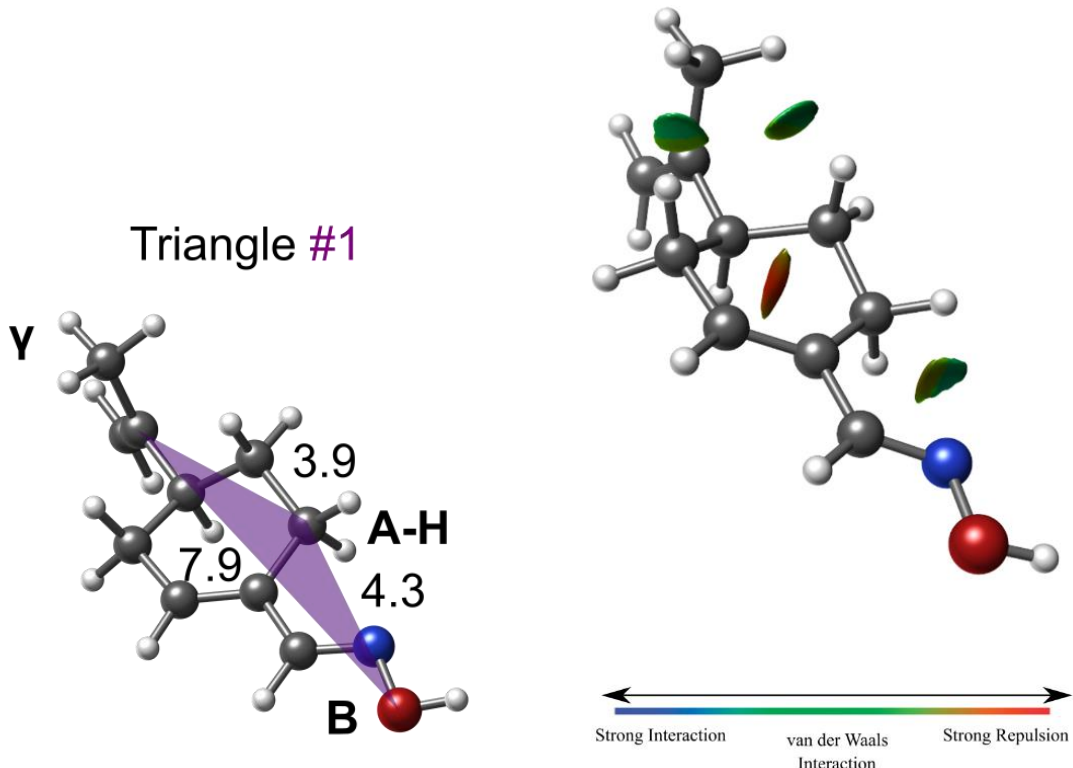


Figure 6. Left: the most stable structure of perillartine showing a possible sweetness-triangle. The distances are given in Armstrong. Right: *NCI plot* of the most stable structure of perillartine.

3.3. Conclusion

The molecular geometry of perillartine has been investigated in the gas phase using rotational spectroscopy. Four structures, which correspond to the most stable structures, have been identified. The four structures show a *trans* configuration of the C=N group with respect to the double bond in the ring. Among them, one of the structures have the allyl group in an axial position, while three structures are in equatorial disposition differing in the orientation of the allyl group.

All the conformers are in accordance with having a three-point contact as proposed by the sweetness theory. In general, our work provides additional support to Shallenberger-Acree-Kier's theory that links the chemical structure of conformers with the sweetness of a molecule.

3.4. References

1. Kinghorn, A.D.; Compadre, C.M. Less common high-potency sweeteners. In *Alternative Sweeteners*; Nabors, L.O., Gelardi, R.C., Eds.; Marcel Dekker: New York, NY, USA, 2001; pp. 209–234.
2. Johnson, R.K.; Appel, L.J.; Brands, M.; Howard, B.V.; Lefevre, M.; Lustig, R.H.; Sacks, F.; Steffen, L.M.; Wylie-Rosett, J. Dietary sugars intake and cardiovascular health a scientific statement from the American heart association. *Circulation* **2009**, *120*, 1011–1020.
3. Tedstone, A.; Targett, V.; Allen, R. Sugar Reduction: The evidence for action About Public Health England. *Public Heal. Engl.* **2015**.
4. Carocho, M.; Morales, P.; Ferreira, I.C.F.R. Sweeteners as food additives in the XXI century: A review of what is known, and what is to come. *Food Chem. Toxicol.* **2017**, *107*, 302–317.
5. Shankar, P.; Ahuja, S.; Sriram, K. Non-nutritive sweeteners: Review and update. *Nutrition* **2013**, *29*, 1293–1299.
6. Oertly, E.; Myers, R.G. A new theory relating constitution to taste. Preliminary paper: Simple relations between the constitution of aliphatic compounds and their sweet taste. *J. Am. Chem. Soc.* **1919**, *41*, 855–867.
7. Cohn, G. Die organischen Geschmacksstoffe. *F. Siemenroth* **1914**, 936.
8. Shallenberger, R.; Acree, T. Molecular Theory of Sweet Taste. *Nature* **1967**, *216*, 480–482.
9. Kier, L.B. A Molecular Theory. **1972**, 1394–1397.
10. Peña, I.; Mata, S.; Martín, A.; Cabezas, C.; Daly, A. M. and Alonso, J. L. Conformations of D-xylose: the pivotal role of the intramolecular hydrogen-bonding., *Phys. Chem. Chem. Phys.*, **2013**, *15*, 18243–8.
11. Bermúdez, C.; Peña, I.; Mata, S.; Alonso, J.L. Sweet Structural Signatures Unveiled in Ketohexoses. *Chem. - A Eur. J.* **2016**, *22*, 16829–16837.
12. Alonso, E.R.; León, I.; Kolesniková, L.; Alonso, J.L. The Structural Signs of Sweetness in Artificial Sweeteners: A Rotational Study of Sorbitol and Dulcitol. *ChemPhysChem* **2018**, *4*, 3334–3340.
13. Alonso, E.R.; León, I.; Kolesniková, L.; Alonso, J.L. Rotational Spectrum of Saccharin: Structure and Sweetness. *J. Phys. Chem. A* **2019**, *123*, 2756–2761.
14. Furukawa, S. . *Tokyo Kagaku Kaishi* **1920**, *41*, 706–728.
15. Shallenberger, R.S. Taste Chemistry; Springer: Berlin/Heidelberg, Germany, 1993; Volume 5. ISBN 978-0751401509.
16. Acton, E.M.; Leafier, M.A.; Oliver, S.M.; Stone, H. Structure-Taste Relationships in Oximes Related to Perillartine. *J. Agric. Food Chem.* **1970**, *18*, 1061–1068.
17. Takahashi, Y.; Miyashita, Y.; Tanaka, Y.; Hayasaka, H.; Abe, H.; Sasaki, S.I. Discriminative Structural Analysis Using Pattern Recognition Techniques in the Structure-Taste Problem of Perillartines. *J. Pharm. Sci.* **1984**, *73*, 737–741.
18. Heijden, A. Van Der; Wei, H. Van Der; Peer, H.G. Structure-activity relationships in sweeteners . **1985**, *10*, 73–88.

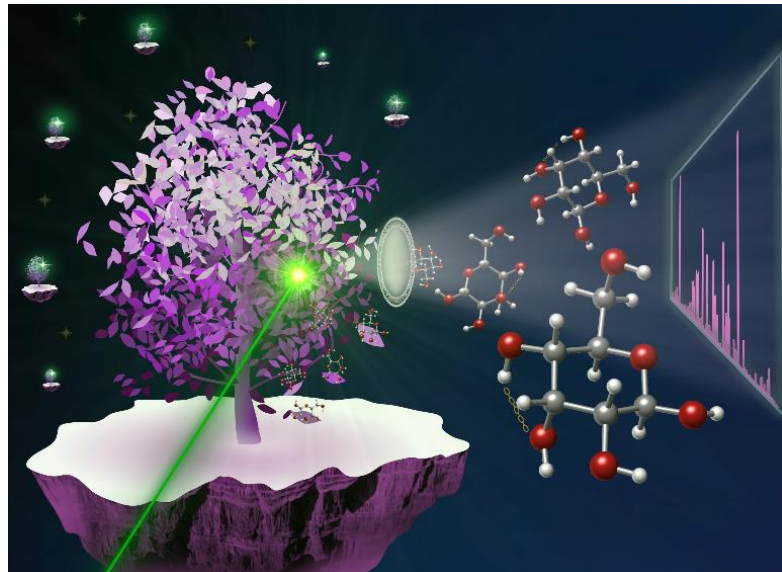
19. Acton, E.M.; Leafier, M.A.; Oliver, S.M.; Stone, H. Structure-Taste Relationships in Oximes Related to Perillartine. *J. Agric. Food Chem.* **1970**, 18, 1061–1068.
20. Acton, E.M.; Stone, H. Potential New Artificial Sweetener from Study of Structure-Taste Relationships. *Science* **1976**, 193, 584–586
21. Iwamura, H. Structure-Taste Relationship of Perillartine and Nitro- and Cyanoaniline Derivative. *J. Med. Chem.* **1980**, 23, 308–312.
22. Venanzi, T.J.; Venanzi, C.A. Ab Initio Molecular Electrostatic Potentials of Perillartine Analogues: Implications for Sweet-Taste Receptor Recognition. *J. Med. Chem.* **1988**, 31, 115077.
23. Hooft, R.W.W.; Van Der Sluis, P.; Kanters, J.A.; Kroon, J. Structure of racemic 4-isopropenyl-1-cyclohexene-1-carbaldehyde oxime (perillartine). *Acta Crystallogr. Sect. C* **1990**, 46, 1133–1135.
24. Grimme, S.; Antony, J.; Ehrlich, S.; Krieg, H. A consistent and accurate ab initio parametrization of density functional dispersion correction (DFT-D) for the 94 elements H-Pu. *J. Chem. Phys.* **2010**, 132, 154104.
25. Grimme, S.; Ehrlich, S.; Goerigk, L.J. Effect of the damping function in dispersion corrected density functional theory. *Comput. Chem.* **2011**, 32, 1456–1465.
26. Frisch, M.J.; Pople, J.A.; Binkley, J.S. Self-consistent molecular orbital methods 25. Supplementary functions for Gaussian basis sets. *J. Chem. Phys.* **1984**, 80, 3265–3269.
27. Cabezas, C.; Varela, M.; Alonso, J.L. The Structure of the Elusive Simplest Dipeptide Gly-Gly. *Angew. Chem. Int. Ed.* **2017**, 129, 6520–6525.
28. Peña, I.; Cabezas, C.; Alonso, J.L. The nucleoside uridine isolated in the gas phase. *Angew. Chem. Int. Ed.* **2015**, 54, 2991–2994.
29. Bermúdez, C.; Mata, S.; Cabezas, C.; Alonso, J.L. Tautomerism in Neutral Histidine. *Angew. Chem. Int. Ed.* **2014**, 53, 11015–11018.
30. Plusquellec, D. F. JB95 Spectral Fitting Program; NIST: Gaithersburg, MD. <http://www.nist.gov/pml/electromagnetics/grp05/jb95.cfm>
31. Gordy, W.; Cook, R.L. *Microwave Molecular Spectroscopy*; John Wiley & Sons, Ed.; New York, **1984**.
32. Pickett, H.M. The fitting and prediction of vibration-rotation spectra with spin interactions. *J. Mol. Spectrosc.* **1991**, 148, 371–377.
33. Møller, C.; Plesset, M.. Note on an Approximation Treatment for Many-Electron Systems. *Phys. Rev.* **1934**, 46, 618–622.
34. Chaudret, R.; De Courcy, B.; Contreras-García, J.; Gloaguen, E.; Zehnacker-Rentien, A.; Mons, M.; Piquemal, J.P. Unraveling non-covalent interactions within flexible biomolecules: From electron density topology to gas phase spectroscopy. *Phys. Chem. Chem. Phys.* **2014**, 16, 9876–9891.

4. Chapter

Understanding the sweetness of the rare sugar β -D-allose

Adapted from: *Phys. Chem. Chem. Phys.*, 2022, 24, 23076-23081.

Abstract: D-allose is a monosaccharide known as 'rare sugar'. In this chapter, we study its conformational landscape using laser ablation in combination with high-resolution rotational spectroscopy. Three species are identified. The three conformers are stabilized through a counter-clockwise intramolecular hydrogen bond network. All the conformers show a similar structural disposition, but differing in the position of the hydroxymethyl group. We study the effect of epimerization on the main aldohexose and find that the main conformers in glucose and allose are very similar and have similar abundances, which could explain the similar sweetness of both molecules.



4.1. Introduction

Carbohydrates are one of the most important class of biomolecules found in our planet. The most basic units are the monosaccharides which are the simplest form of sugar. There are more than 50 types of monosaccharides on Earth, each one with characteristic and extraordinary properties [1,2]. Among them, glucose is an aldohexose that deserves a special mention due to being the most abundant monosaccharide, playing a key role in many processes important to life such as glycogenesis or photosynthesis [3–6]. Glucose, together with mannose and galactose, is found in the human body [3,7–9]. Interestingly, allose, the C₃ epimer of glucose, is rarely found in nature and belongs to the *rare sugars* category [10]. In fact, β-allose has only been isolated from the leaves of the Rubropyl Protea, an African bush,[8] in which it appears bound to two esters. On the other hand, glucose is the structural unit of cellulose, which is the most abundant biopolymer on Earth [11,12].

Despite being a *rare sugar*, D-allose has numerous benefits for human health. For example, it has several benefits as an antioxidant [13–15], it provides anti-tumor properties [16–19], and it has anti-inflammatory effects [20–22]. Additionally, D-allose is perceived with an intensely sweet taste similar to glucose [23], and is 80% sweeter than sucrose [24]. More importantly, allose does not go through the metabolism process, so it is ultra-low calorie making it an ideal table-sugar substitute [25].

Due to the structure-property relationship, all the properties of allose should be strongly related to its structure. Therefore, details at a molecular level could shed some light on its properties. Additionally, the effects of epimerization can be studied: It is very interesting how the variation in the position of a single OH group (see Figure 1) gives rise to similar and different biological implications at the same time: both molecules present a similar sweetness, but while β-D-glucose is among the most abundant organic compounds in the biosphere [12], β-D-allose cannot be metabolized and barely exists in nature. Likewise, the structural determination of allose could allow us to understand the mechanisms underlying the antioxidant or antiproliferative activity.

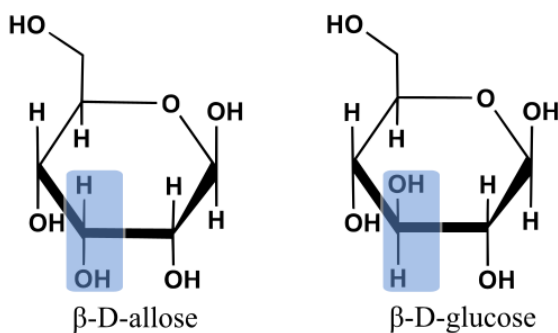


Figure 1. Chemical structures of β-D-allose (left) and β-D-glucose (right).

The conformational preferences of this sugar have so far been experimentally investigated using X-ray crystallography [26], from Vibrational Circular Dichroisms (VCD) measurements [27], from the results using Vibrational Raman Optical Activity

(ROA) [28], and from NMR studies [29,30]. However, the intrinsic conformational nature of the molecule has not been revealed, since these studies have been carried out in a condensed phase. In order to determine the structure of β -D-allose free from any environmental effect, in this chapter we present a rotational spectroscopic study of β -D-allose using Laser Ablation Chirped Pulse Fourier Transform Microwave (LA-CP-FTMW) spectroscopy.

4.2. Results and Discussion

Conformational panorama

In order to ease the experimental characterization of allose, we initially performed a conformational search. As shown in Figure 2, β -D-allose can adopt different configurations depending on the orientation of the hydroxymethyl group. The Newman projection indicates the torsion angle as the angle (having an absolute value between 0° and 180°) between bonds to two specified (fiducial) groups, one from the atom nearer (proximal) to the observer and the other from the further (distal) atom [24]. The resulting conformations around the terminal hydroxymethyl group give rise to the G+ (60°), G- (60°), T (180°), g+ (60°), g- (60°), and t (180°) configurations. We used the symbol *cl* or *cc* to describe the clockwise (*cl*) or counterclockwise (*cc*) arrangement of the cooperative network of intramolecular hydrogen bonds. A total of 8 stable structures of β -D-allose are found within an energetical window of 1000 cm^{-1} relative to the global minimum. The structures are shown in Figure 3, while the relevant spectroscopic parameters are collected in Table 1.

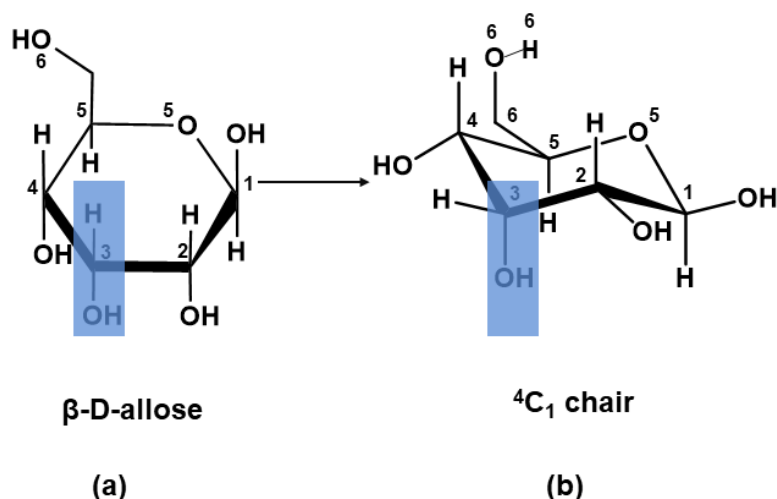


Figure 2. (a) Haworth projection of β -D-allose. (b) ${}^4\text{C}_1$ chair conformation.

As can be seen, the eight most stable structures have a ${}^4\text{C}_1$ ring configuration, which results in a higher stability. Interestingly, the six most stable conformers have a counterclockwise intramolecular hydrogen bond network between the hydroxyl groups, while the clockwise arrangement is energetically less stable. Among the six most stable

structures, the structures differ in the orientation of the hydroxymethyl group, with those positioned towards the molecule (structures G-g+/cc/t, G+g-/cc/t, and Tg+/cc/t), being 800 cm^{-1} more stable than those with the hydroxymethyl group pointing outwards due to the extra hydrogen bond. Only the three most stable structures are expected to be populated enough in a supersonic expansion [23, 33–35].

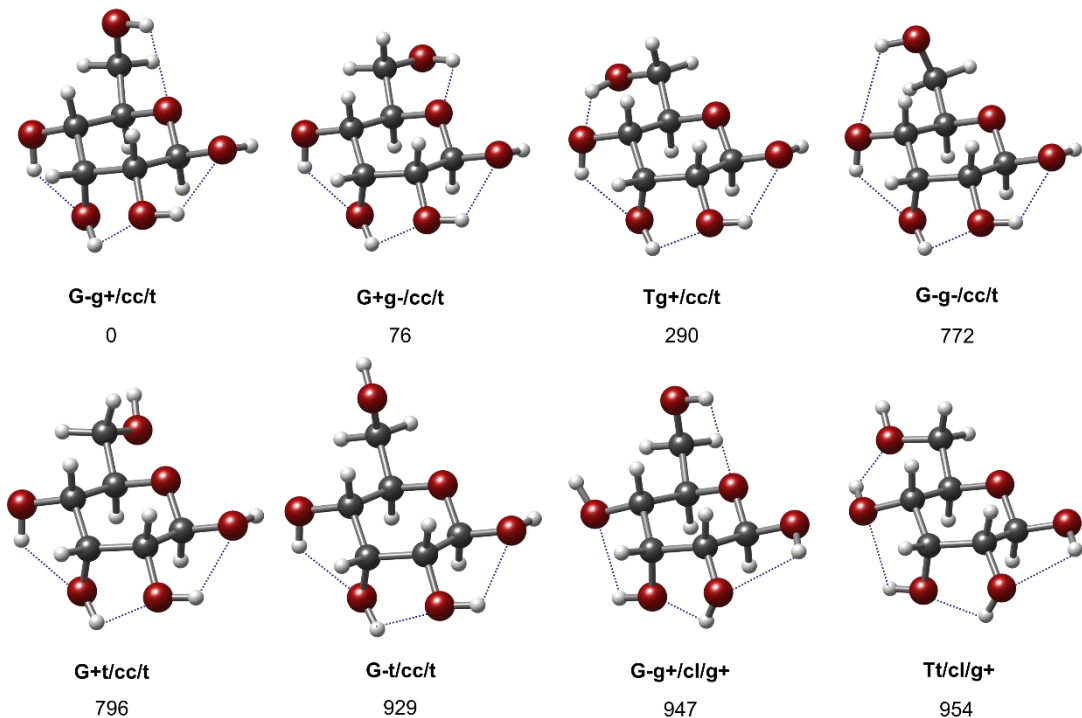


Figure 3. The eight most stable conformers of β -D-allose calculated using the MP2/6-311++G(d,p) methodology. Energies are given in cm^{-1} .

Table 1. Calculated spectroscopic parameters for β -D-allose at MP2/6-311G++(d,p).

	G- g+/cc/t	G+ g-/cc/t	T g+/cc/t	G- g-/cc/t	G+ t/cc/t	G- t/cc/t	G- g+/c/g+	T t/c/g+
A ^[a]	1273.5	1232.9	1466.4	1370.3	1252.5	1315.6	1288.8	1476.7
B	813.3	801.0	723.4	765.0	783.6	792.9	803.7	730.2
C	562.0	533.8	529.6	551.9	533.7	560.2	558.3	530.2
$ \mu_a ^{[b]}$	3.0	2.8	3.3	1.8	0.2	0.3	0.8	3.4
$ \mu_b $	1.6	1.5	0.2	0.3	1.1	1.4	2.6	0.2
$ \mu_c $	2.2	0.4	0.4	2.1	0.1	2.2	0.3	0.3
$\Delta E^{[c]}$	0	103	243	808	958	969	1042	899
$\Delta E_{ZPE}^{[d]}$	0	76	290	772	796	929	947	954
$\Delta G^{[e]}$	0	45	320	701	676	735	826	984

[a] A, B, and C represent the rotational constants (in MHz). [b] μ_a , μ_b and μ_c are the electric dipole moment components (in D). [c] Relative energies (in cm^{-1}) with respect to the global minimum. [d] Relative energies (in cm^{-1}) with respect to the global minimum, taking into account the zero point energy (ZPE). [e] Gibbs energies (in cm^{-1}) calculated at 298 K.

Broadband rotational spectrum

The broadband microwave spectrum of β -D-allose obtained in the 4–8 GHz frequency range is shown in Figure 4. After removing the spectral signatures of known photofragmentation products [31], the spectrum still consisted of several rotational lines, indicating that several species must be present. The identification was done using the calculated spectroscopic parameters, starting from the most energetically-stable ones. As shown in Table 1, all the conformers are prolate asymmetric tops with relatively high values of the electric dipole moment component μ_a . Thus, our strategy was to locate a set of characteristic *a*-type R-branch transitions, with a spacing of $\sim B+C$. It was very easy to observe such pattern for a first rotamer I, due to the intense *a*-type R-branch transitions that were fitted using a rigid rotor Hamiltonian [32,33]. The generated rotational constants allowed us to expand the assignments to the *b*- and *c*-type transitions. A total of 141 transitions were finally assigned, resulting in 65 *a*-type, 29 *b*-type, and 25 *c*-type R-branch transitions added to the fit. Table 2 collects the rotational constants obtained.

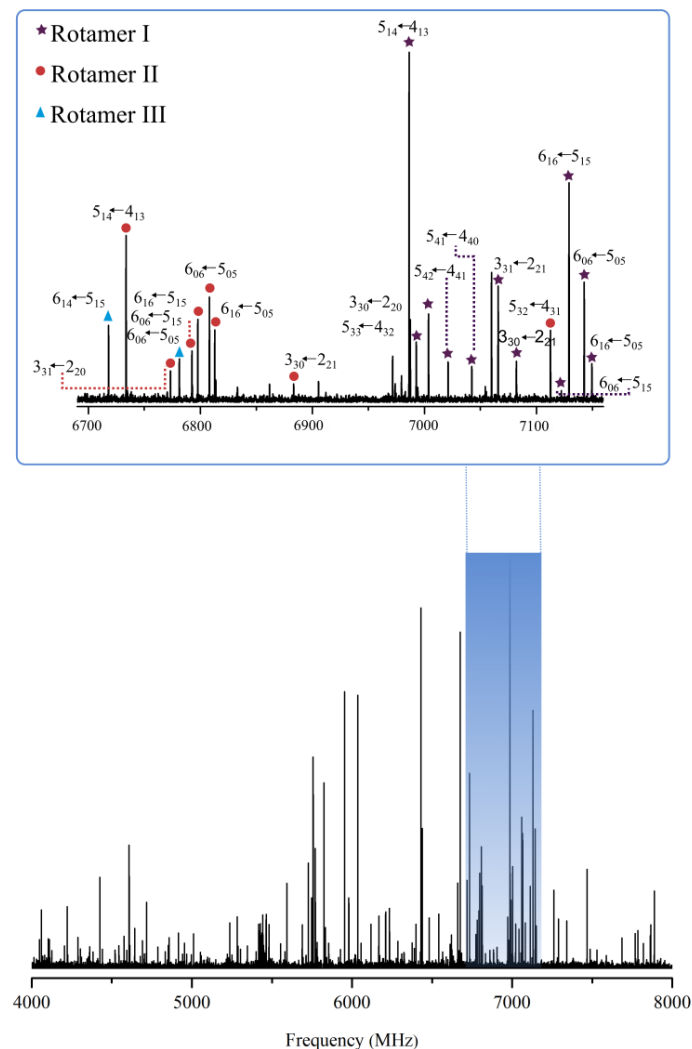


Figure 4. Bottom: Broadband CP-FTMW rotational spectrum of β -D-allose in the 4–8 GHz frequency region. Top: Inset of the CP-FTMW spectrum showing selected rotational transitions ascribed to the three detected rotamers.

After assigning all the rotational lines belonging to the first rotamer, several lines still remained unassigned in the spectrum, so we searched for other candidates. Two additional rotamers were found. 77 transitions, including *a*- and *b*-types, were measured for rotamer II, while only 24 *a*-type rotational transitions were observed for rotamer III. The experimentally obtained spectroscopic parameters for each species are listed in Table 2, while all the lines for the identified species are collected in the Tables AII-1 to AII-3.

Table 2. Experimental and calculated spectroscopic parameters for β -D-allose.

	Experimental			Theory		
	I	II	III	G-g+/cc/t	G+g-/cc/t	Tg+/cc/t
<i>A</i> ^[a]	1267.54158(31) ^[i]	1230.06990(42)	1457.052(17)	1273.5	1232.9	1466.4
<i>B</i>	810.31204(19)	796.28806(22)	721.77324(78)	813.3	801.0	723.4
<i>C</i>	559.37787(22)	530.88028(14)	526.66014(67)	562.0	533.8	529.6
$ \mu_a $ ^[b]	Observed	Observed	Observed	3.0	2.8	3.3
$ \mu_b $	Observed	Observed	-	1.6	1.5	0.2
$ \mu_c $	Observed	-	-	2.2	0.4	0.4
ΔJ ^[c]	0.0150(12)	-	-			
σ ^[d]	10.8	16.8	15.1			
N ^[e]	141	77	24			
ΔE ^[f]				0	103	243
ΔE_{ZPE} ^[g]				0	76	290
ΔG ^[h]				0	45	320

[a] *A*, *B*, and *C* represent the rotational constants (in MHz). [b] μ_a , μ_b and μ_c are the electric dipole moment components (in D). [c] ΔJ is the quartic centrifugal distortion constant (in kHz). [d] RMS deviation of the fit (in kHz). [e] Number of measured transitions [f] Relative energies (in cm^{-1}) with respect to the global minimum. [g] Relative energies (in cm^{-1}) with respect to the global minimum, taking into account the zero point energy (ZPE). [h] Gibbs energies (in cm^{-1}) calculated at 298 K. [i] Standard error in parentheses in units of the last digit.

Conformational identification

Tables 1 and 2 show that there is a good correspondence between the experimental rotational constants of rotamer I with those calculated for the G-g+/cc/t structure. The selection rules further confirm the assignment as the dipole moment in the three axes have a significant value, and all types of rotational transitions were observed. Similarly, the experimental rotational constants and selection rules of rotamer II are in good agreement with those of the G+g-/cc/t structure. Finally, the rotational constants of rotamer III, which are radically different from the other two rotamers, along with the observance of only *c*-type transitions, are in good agreement with the predicted values of the Tg+/cc/t structure. We note how the obtained rotational constants at B3LYP-GD3BJ/6-311++G(d,p) level of theory agree very well with the experimental values. We calculated the scale factors by dividing the experimental rotational constants by the calculated ones. Scale factors ranging from 1.002 to 1.006 brings the predicted values of the rotational constants into coincidence with the experimental ones [34, 35].

We also estimated the relative population of the detected conformers based on the intensities of the rotational transitions and the predicted dipole moments. We found that the G-g+/cc/t and G+g-/cc/t structures have a similar abundance (50% and 40%, respectively), while the Tg+/cc/t structure is only about a 10%. These results are in good agreement with the estimated abundances using the relative energies.

Analysis of the main intramolecular interactions

The structures of the three experimental conformers of β -D-allose are shown in Figure 5. As previously stated, the three conformers of β -D-allose anomer present a 4C_1 arrangement due to the presence of intramolecular interactions between the OH groups, which behave as bifunctional entities, acting as proton donors or proton acceptors. This cooperative hydrogen bonding network observed for all shapes is arranged counterclockwise and is made up of the series O_4H (eq) $\rightarrow O_3H$ (ax) $\rightarrow O_2H$ (eq) $\rightarrow O_1H$ (eq). The three detected conformers, which are also the three most stable structures, only differ in the orientation of the CH_2OH group.

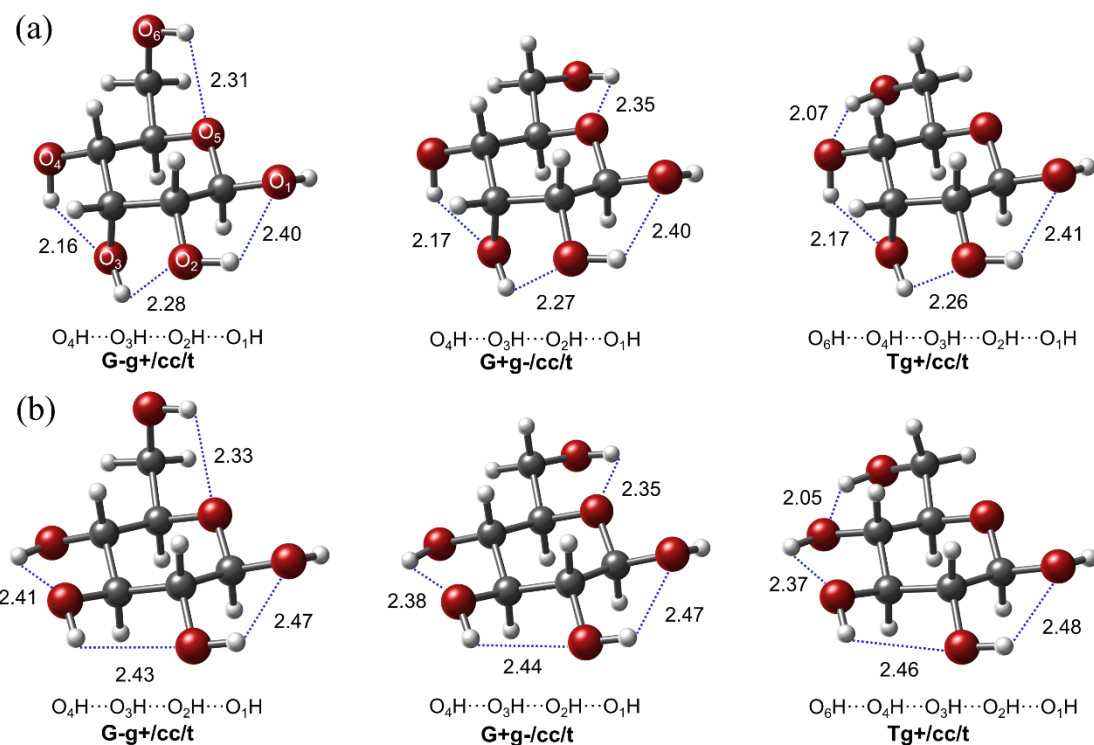


Figure 5. (a) Three-dimensional structures of the three observed conformers of β -D-allose showing the cooperative intramolecular hydrogen-bonding networks. (b) A comparison with the observed structures of β -D-glucose [20]. The distances are given in Å.

Structure-property relationship

We now proceed to analyze the effect of epimerization. As stated in the introduction, both the C₁ and C₄ epimerizations studied so far present some notorious changes: for the C₁ epimerization an extra conformer is observed in α -D-glucopyranose [36], while for the C₄ epimerization it drastically changes the conformational behaviour by altering the abundances of the most stable conformers, as well as the main intramolecular forces that stabilizes them [37]. Figure 5 compares the intramolecular hydrogen bond distances for the detected conformers of β -D-allose and β -D-glucose. Interestingly, the comparison, *a priori*, seems to indicate that both structures behave similarly: for both molecules, three stable conformers have been detected. They all present a cooperative intramolecular network involving the O₄H (eq) \rightarrow O₃H (eq) \rightarrow O₂H (eq) \rightarrow O₁H (eq) functional groups, and the relative population of the two most stable structures is about 45% each, while the third conformer is a minor species (about 10% of the relative population).

Furthermore, a comparison of the sweetness triangle suggested by the Shallenberger for glucose [38,39], by choosing the A/H/B/ γ points for allose, also gives the same outcome (see Figure 6). All the distances are in good agreement with the theory proposed by Shallenberger-Acree-Kier.

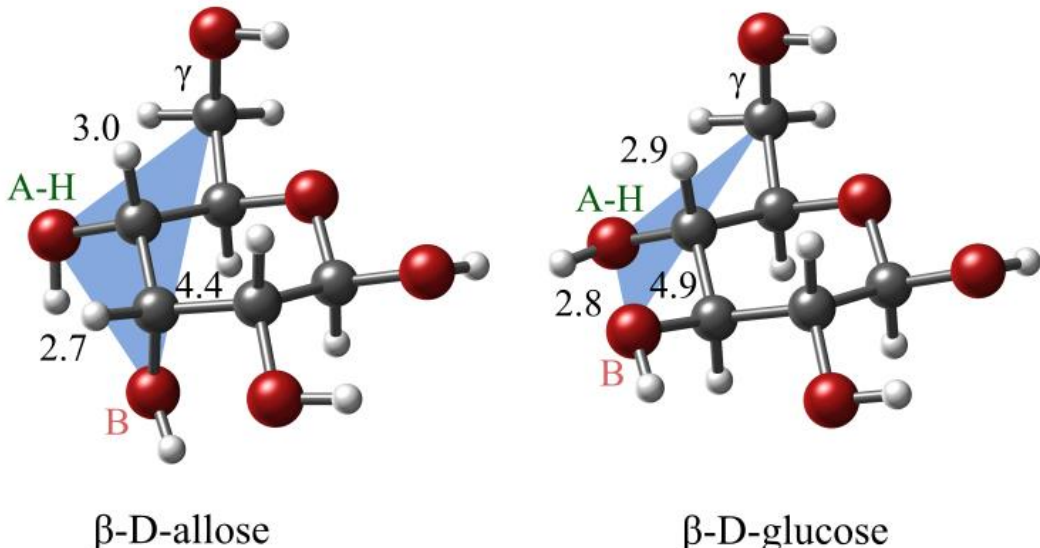


Figure 6. (a) Three-dimensional structures of the three observed conformers of β -D-allose showing the cooperative intramolecular hydrogen-bonding networks. (b) A comparison with the observed structures of β -D-glucose [20]. The distances are given in Å.

To sum up, the fact that both molecules behave similarly and that they meet exactly the same criteria for the sweetness triangle, altogether could explain why both molecules present a similar sweetness.

Influence on their natural abundance

But, why is glucose abundant in nature while allose is barely found commonly? Why does glucose metabolize in the body while allose is not? Understanding the latter is important to synthesize new artificial sweeteners.

A careful inspection of both molecules show that there are some important differences between both epimers. The conformers of β -D-glucose exhibit weaker intramolecular hydrogen bonds than those of β -D-allose. This is due to all hydroxyl groups being in an equatorial arrangement and therefore in alternate positions, enlarging the non-covalent bond distances [36,40,41] the O_4H (eq) $\rightarrow O_3H$ (eq) $\rightarrow O_2H$ (eq) hydrogen bond distances decrease about 0.2 Å when going from β -D-glucose to β -D-allose. In order to evaluate the strength of the intramolecular hydrogen bonds within each sugar, we carried out a computerized numerical analysis and graphic user-assisted interpretation of the electronic density (ρ) and its derivatives using the *NCIplot* program [42,43]. The results are collected in Figure 7. There is indeed a relatively strong cooperative hydrogen bond network for β -D-allose in contrast to β -D-glucose, which shows very weak non-covalent interactions for the $O_4H \rightarrow O_3H$ and $O_3H \rightarrow O_2H$ intramolecular interactions.

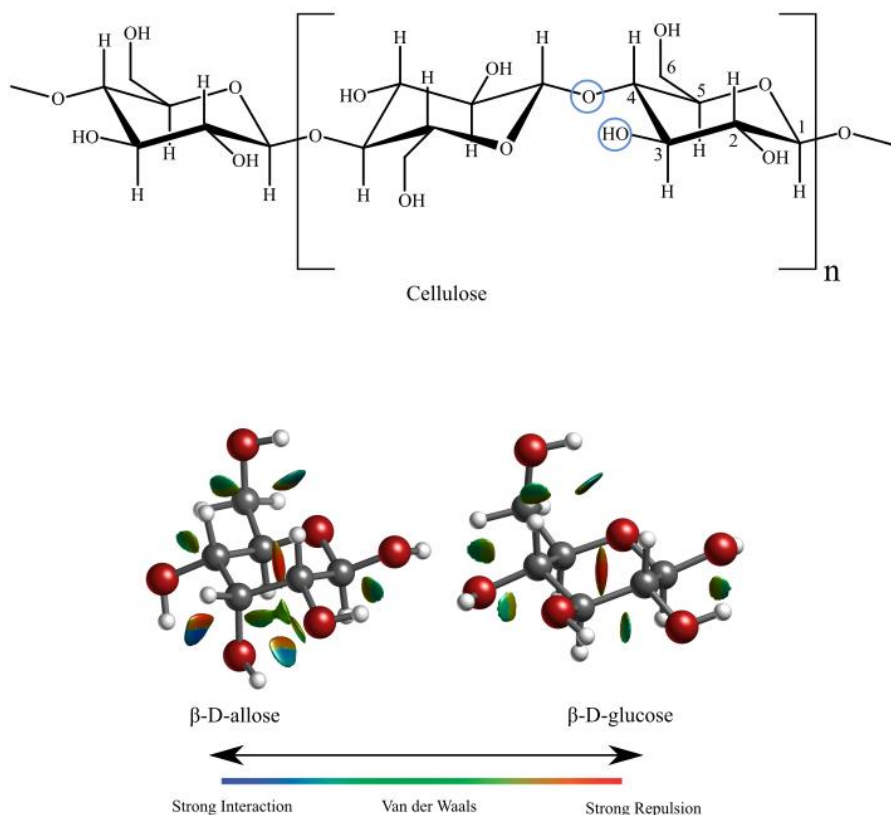


Figure 7. Top: the non-covalent interactions of the most stable conformer (G-g+/cc/t) of β -D-allose and β -D-glucose. Bottom: the unbranched polymer of β -D-glucose occurs through the linkage of $\beta(1 \rightarrow 4)$ D-glucose units. The responsible hydroxyl functional groups (O_3H and O_4H) that have a strong intramolecular hydrogen bond in β -D-allose but weaker in β -D-glucose are encircled.

One exciting outcome about the differences in the intermolecular interactions of allose and glucose is related to their biological function. As explained earlier, glucose is very common in nature and is metabolized by humans and other animals, while allose is scarce and it is not metabolized. One possible interpretation could be that it is due to their differences in the strength of the intramolecular interactions discussed above: the cellulose polysaccharide requires the construction of a linear chain of several hundred to many thousands of $\beta(1\rightarrow4)$ linked D-glucose units (see Figure 6); because this covalent bond happens through the O₄H hydroxyl group of the anomeric C₄ carbon, the formation of such polysaccharides should be statistically more favorable if the O₄H is easier to attack. In β -D-glucose, the hydrogen bond is considerably weaker than in β -D-allose, and thus the energetic cost to polymerize the former should be considerably lower as it requires breaking a weaker bond. The same applies to the energetic cost required to breaking the bonds during the metabolisms, leading the evolution to design more specific enzymes towards glucose rather than for allose.

4.3. Conclusion

The combination between laser ablation and rotational spectroscopy has allowed us to identify the conformational preferences of the β -D-allose carbohydrate unequivocally. Three conformers have been identified showing a cooperative network of hydrogen bonds in a O₄H (eq) → O₃H (ax) → O₂H (eq) → O₁H (eq) disposition and in a counterclockwise (cc) arrangement. The three conformers only differ in the orientation of the hydroxymethyl group.

The effect of epimerization on the C₃ atom has also been investigated by comparing the results of β -D-allose and β -D-glucose. On the one hand, both molecules behave similarly as they present the same number of conformers, the interaction that stabilizes them are alike, and the population of the main conformers is similar. Additionally, all the conformers are in accordance with the sweetness theory and both molecules have the same glucophore sites. All this similarity could explain why both molecules present a similar sweetness.

On the other hand, despite the main conformers being very similar, the cooperative hydrogen bond network in allose is considerably stronger than that in glucose. This could be the reason why cellulose, an unbranched polymer of β -D-glucose, is among the most abundant organic compounds in the biosphere, while β -D-allose is scarce.

4.4. References

1. Izumori, K. Bioproduction strategies for rare hexose sugars. *Naturwissenschaften* **2002**, *89*, 120–124.
2. Izumori, K. Izumoring: A strategy for bioproduction of all hexoses. *J. Biotechnol.* **2006**, *124*, 717–722.
3. Lemieux, R. U. Explorations with Sugars: How Sweet It Was, Washington, DC, American C., **1990**.
4. Collins, P. M. and Ferrier, R. J. Monosaccharides: their chemistry and their roles in natural products, Wiley & Sons, New York, **1995**.
5. Blanco, Antonio, and G.B. Medical Biochemistry . Academic Press, 2018. **2017**, 283–323.
6. Cushman, J.C.; Taybi, T.; Bohnert, H.J. Photosynthesis: Physiology and Metabolism 2000, 551–582.
7. Wild, J.; Robinson, D.; Winchester, B. Isolation of mannose-binding proteins from human and rat liver. *Biochem. J.* **1983**, *210*, 167–174.
8. Weis, W.I.; Drickamer, K.; Hendrickson, W.A. Structure of a C-type mannose-binding protein complexed with an oligosaccharide. *Nature* **1992**, *360*, 127–134,
9. Coelho, A.I.; Berry, G.T.; Rubio-Gozalbo, M.E. Galactose metabolism and health. *Curr. Opin. Clin. Nutr. Metab. Care* **2015**, *18*, 422–427
10. Yamaguchi, F.; Takata, M.; Kamitori, K.; Nonaka, M.; Dong, Y.; Sui, L.; Tokuda, M. Rare sugar D-allose induces specific up-regulation of TXNIP and subsequent G1 cell cycle arrest in hepatocellular carcinoma cells by stabilization of p27kip1. *Int. J. Oncol.* **2008**, *32*, 377–385.
11. Beylis, B. P. and Perold, G. W. The Occurrence of D- (+) -Allose in Nature, **1971**, *11*, 1971.
12. Ragauskas, A.J.; Williams, C.K.; Davison, B.H.; Britovsek, G.; Cairney, J.; Eckert, C.A.; Frederick, W.J.; Hallett, J.P.; Leak, D.J.; Liotta, C.L.; et al. The path forward for biofuels and biomaterials. *Science (80-.).* **2006**, *311*, 484–489.
13. Ishihara, Y.; Katayama, K.; Sakabe, M.; Kitamura, M.; Aizawa, M.; Takara, M.; Itoh, K. Antioxidant properties of rare sugar D-allose: Effects on mitochondrial reactive oxygen species production in Neuro2A cells. *J. Biosci. Bioeng.* **2011**, *112*, 638–642.
14. Murata, A.; Sekiya, K.; Watanabe, Y.; Yamaguchi, F.; Hatano, N.; Izumori, K.; Tokuda, M. A novel inhibitory effect of D-allose on production of reactive oxygen species from neutrophils. *J. Biosci. Bioeng.* **2003**, *96*, 89–91.
15. Nakamura, T.; Tanaka, S.; Hirooka, K.; Toyoshima, T.; Kawai, N.; Tamiya, T.; Shiraga, F.; Tokuda, M.; Keep, R.F.; Itano, T.; et al. Anti-oxidative effects of d-allose, a rare sugar, on ischemia-reperfusion damage following focal cerebral ischemia in rat. *Neurosci. Lett.* **2011**, *487*, 103–106.
16. Jeong, R.U.; Lim, S.; Kim, M.O.; Moon, M.H. Effect of d-allose on prostate cancer cell lines: Phospholipid profiling by nanoflow liquid chromatography-tandem mass spectrometry. *Anal. Bioanal. Chem.* **2011**, *401*, 689–698.
17. Hoshikawa, H.; Indo, K.; Mori, T.; Mori, N. Enhancement of the radiation effects

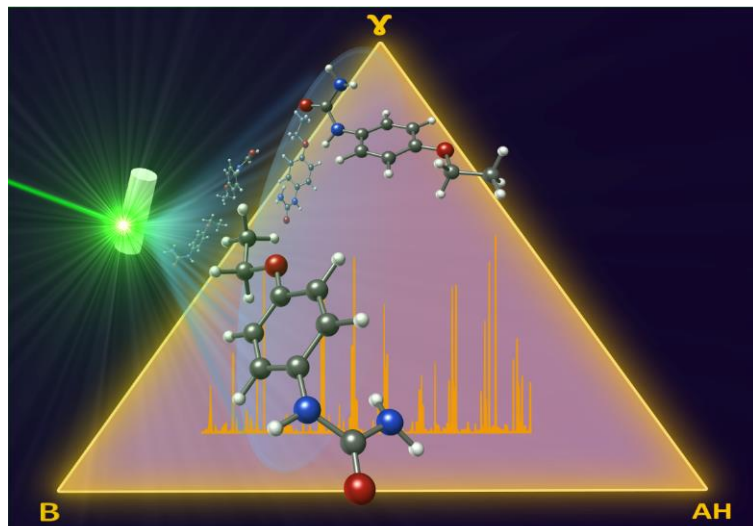
- by d-allose in head and neck cancer cells. *Cancer Lett.* **2011**, *306*, 60–66.
- 18. Malm, S.W.; Hanke, N.T.; Gill, A.; Carbalal, L.; Baker, A.F. The anti-tumor efficacy of 2-deoxyglucose and D-allose are enhanced with p38 inhibition in pancreatic and ovarian cell lines. *J. Exp. Clin. Cancer Res.* **2015**, *34*, 1–12.
 - 19. Noguchi, C.; Kamitori, K.; Hossain, A.; Hoshikawa, H.; Katagi, A.; Dong, Y.; Sui, L.; Tokuda, M.; Yamaguchi, F. D-allose inhibits cancer cell growth by reducing GLUT1 expression. *Tohoku J. Exp. Med.* **2016**, *238*, 131–141.
 - 20. Huang, T.; Gao, D.; Hei, Y.; Zhang, X.; Chen, X.; Fei, Z. D-allose protects the blood brain barrier through PPAR γ -mediated anti-inflammatory pathway in the mice model of ischemia reperfusion injury. *Brain Res.* **2016**, *1642*, 478–486.
 - 21. Gao, D.; Kawai, N.; Tamiya, T. The anti-inflammatory effects of d-allose contribute to attenuation of cerebral ischemia-reperfusion injury. *Med. Hypotheses* **2011**, *76*, 911–913.
 - 22. Yamada, K.; Noguchi, C.; Kamitori, K.; Dong, Y.; Hirata, Y.; Hossain, M.A.; Tsukamoto, I.; Tokuda, M.; Yamaguchi, F. Rare sugar d-allose strongly induces thioredoxin-interacting protein and inhibits osteoclast differentiation in Raw264 cells. *Nutr. Res.* **2012**, *32*, 116–123.
 - 23. Lindley, M.G.; Birch, G.G. Structural functions of taste in the sugar series. *J. Sci. Food Agric.* **1975**, *26*, 117–124.
 - 24. Chen, Z.; Chen, J.; Zhang, W.; Zhang, T.; Guang, C.; Mu, W. Recent research on the physiological functions, applications, and biotechnological production of d-allose. *Appl. Microbiol. Biotechnol.* **2018**, *102*, 4269–4278.
 - 25. Mooradian, A.D.; Smith, M.; Tokuda, M. The role of artificial and natural sweeteners in reducing the consumption of table sugar: A narrative review. *Clin. Nutr. ESPEN* **2017**, *18*, 1–8.
 - 26. Kroon-Batenburg, L. M. J. P. Van der Sluis and J. A. Kanters, Structure of β -D-Allose, C₆H₁₂O₆, *Acta Cryst.*, **1984**, *2*, 1863–1865.
 - 27. Bose, P.K.; Polavarapu, P.L. Vibrational circular dichroism of monosaccharides. *Carbohydr. Res.* **1999**, *319*, 172–183.
 - 28. Barron, L.D.; Wen, Z.Q.; Hecht, L. Vibrational Raman Optical Activity of Proteins. *J. Am. Chem. Soc.* **1992**, *114*, 784–786.
 - 29. Hobley, P.; Howarth, O.; Ibbett, R.N. ¹H and ¹³C NMR shifts for aldopyranose and aldonofuranose monosaccharides: Conformational analysis and solvent dependence. *Magn. Reson. Chem.* **1996**, *34*, 755–760.
 - 30. Angyal, S.J. The Composition and Conformation of Sugars in Solution. *Angew. Chemie Int. Ed. English* **1969**, *8*, 157–166.
 - 31. Kolesniková, L.; León, I.; Alonso, E.R.; Mata, S.; Alonso, J.L. Laser Ablation Assists Cyclization Reactions of Hydantoic Acid: A Proof for the Near-Attack Conformation Theory? *J. Phys. Chem. Lett.* **2019**, *10*, 1325–1330.
 - 32. Gordy, W. and Cook, R. L. Microwave Molecular Spectroscopy, New York, **1984**.
 - 33. Pickett, H.M. The fitting and prediction of vibration-rotation spectra with spin interactions. *J. Mol. Spectrosc.* **1991**, *148*, 371–377.
 - 34. Sanz-Novo, M.; Alonso, E.R.; León, I.; Alonso, J.L. The Shape of the Archetypical Oxocarbon Squaric Acid and Its Water Clusters. *Chem. - A Eur. J.* **2019**, *25*,

- 10748–10755.
35. Juárez, G.; Sanz-Novo, M.; Alonso, J.L.; Alonso, E.R.; León, I. Rotational Spectrum and Conformational Analysis of Perillartine: Insights into the Structure–Sweetness Relationship. *Molecules* **2022**, *27*, 1924.
 36. Alonso, J.L.; Lozoya, M.A.; Peña, I.; López, J.C.; Cabezas, C.; Mata, S.; Blanco, S. The conformational behaviour of free d -glucose—at last. *Chem. Sci.* **2014**, *5*, 515–522.
 37. Alonso, E.R.; León, I.; Alonso, J.L. *The role of the intramolecular interactions in the structural behavior of biomolecules: Insights from rotational spectroscopy* Elsevier, **2021**, 93–141.
 38. Shallenberger, R.S. *Taste Chemistry*; 1993.
 39. Mathlouthi, M.; Seuvre, A.-M.; Birch, G.G. Relationship between the structure and the properties of carbohydrates in aqueous solutions: Sweetness of chlorinated sugars. *Carbohydr. Res.* **1986**, *152*, 47–61.
 40. Peña, I.; Cabezas, C.; Alonso, J.L. Unveiling epimerization effects: a rotational study of α-d-galactose. *Chem. Commun.* **2015**, *51*, 10115–10118.
 41. Peña, I.; Mata, S.; Martín, A.; Cabezas, C.; Daly, A.M.; Alonso, J.L. Conformations of D-xylose: the pivotal role of the intramolecular hydrogen-bonding. *Phys. Chem. Chem. Phys.* **2013**, *15*, 18243–8.
 42. Contreras-García, J.; Johnson, E.R.; Keinan, S.; Chaudret, R.; Piquemal, J.-P.; Beratan, D.N.; Yang, W. NCIPILOT: a program for plotting non-covalent interaction regions.
 43. Chaudret, R.; De Courcy, B.; Contreras-García, J.; Gloaguen, E.; Zehnacker-Rentien, A.; Mons, M.; Piquemal, J.P. Unraveling non-covalent interactions within flexible biomolecules: From electron density topology to gas phase spectroscopy. *Phys. Chem. Chem. Phys.* **2014**, *16*, 9876–9891.

5. Chapter

The Structural Sign of Sweetness in the Artificial Sweetener Dulcin: A Rotational Study

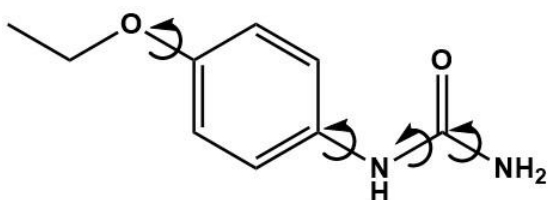
Abstract: This chapter reports on the structure of dulcin, an artificial sweetener. Its solid compound is vaporized by laser ablation and characterized under jet-cooled conditions using a chirped-pulsed Fourier transform microwave spectrometer. Two conformers are identified by comparing the experimental spectroscopic parameters with the theoretical ones. Both structures are stabilized by an N-H $\cdots\pi$ intramolecular hydrogen bond between the -NH₂ and the phenyl ring. A third conformer is also predicted but not detected due to conformational interconversion. All the observed conformers have a glucophore and are in good agreement with the theory of sweet taste proposed by Shallenberger-Acree-Kier's.



5.1. Introduction

Carbohydrates, such as the well-known glucose or allose studied in the previous chapter, are known for their sweet taste. They have polyhydroxy functional groups, a carbonyl group, and four different chiral centers. In fact, most of the early works about the structure and sweetness relationship were based on the most distinctive chemical and physical properties of common saccharides. To further confirm the theory of sweetness in compounds with different functional groups, in this chapter we study dulcin (Scheme 1), a molecule that belongs to the polyurea family. In this family, the position of the alkoxy group substituent in the ring is thought to influence the taste of the compound [1]. Interestingly, while the *ortho* disposition is tasteless, the *meta* substitution leads to bitterness and replacement of the *para* position provides a sweet taste.

Dulcin was discovered in 1884 by Joseph Berlinerblau during a reaction between chlorine cyanide and p-phenetidine ($p\text{-C}_2\text{H}_5\text{O-C}_6\text{H}_4\text{-NH}_2$). The intermediate product was treated with water and isolated as a new compound named as p-ethoxyphenylurea (dulcin) [2,3]. Interestingly, dulcin is the second artificial sweetener ever synthesized and has a sweet taste 250 times larger than sucrose [4]. In regard to the sweetness triangle theory, the *AH* and *B* groups could correspond to the amine and carbonyl groups, respectively [1,5]. The γ point is speculated to be the second carbon of alkoxy group since the 4-methoxyphenylurea compound is considerably less sweet, and since its propoxy derivative is slightly sweet [5]. Despite that dulcin was considered as a perfect sweetener for diabetics [6,7], it was banned in 1950 for using it as a food additive due to its adverse effects [8–10] such as carcinogenesis [11]. Nevertheless, due to its intense sweet capacity it is still being researched and used as a model compound for stimulating the taste buds of the human tongue [12,13]. Its unique properties must be related to its structure, so it can be used to synthesize similar molecules more suitable for consumption but with no adverse effect.



Scheme 1. Chemical structure of dulcin. The arrows indicate the torsional degrees of freedom.

While some derivatives of polyureas have been studied using different techniques such as X-rays, NMR spectroscopy, or semi-empirical calculations, there is no accurate structural determination for dulcin [14]. Consequently, there is no precise data to corroborate the theory of sweetness for this molecule. In this chapter, we present a rotational spectroscopic study of dulcin using Laser Ablation Chirped Pulse Fourier Transform Microwave (LA-CP-FTMW) spectroscopy. As we will show, dulcin presents four stable conformers for which two of them are detected and one is missing due to conformational interconversion. All the conformers meet the requirement suggested by

the theory of sweetness. We provide accurate structural information and propose the possible glucophore sites [15,16].

5.2. Results and Discussion

Conformational panorama

Figure 1 shows that dulcin has several torsions, so a rich conformational panorama is expected. Thus, we conducted a conformational search using Molecular Mechanics and obtained 17 structures within a 25 kJ/mol energy window. Afterwards, we used high-level quantum-chemical calculations at the MP2 and B3LYP-GD3BJ levels obtaining a total of 13 different structures. The structures are shown in Figure 1 and the energetics and relevant rotational parameters are collected in Table 1.

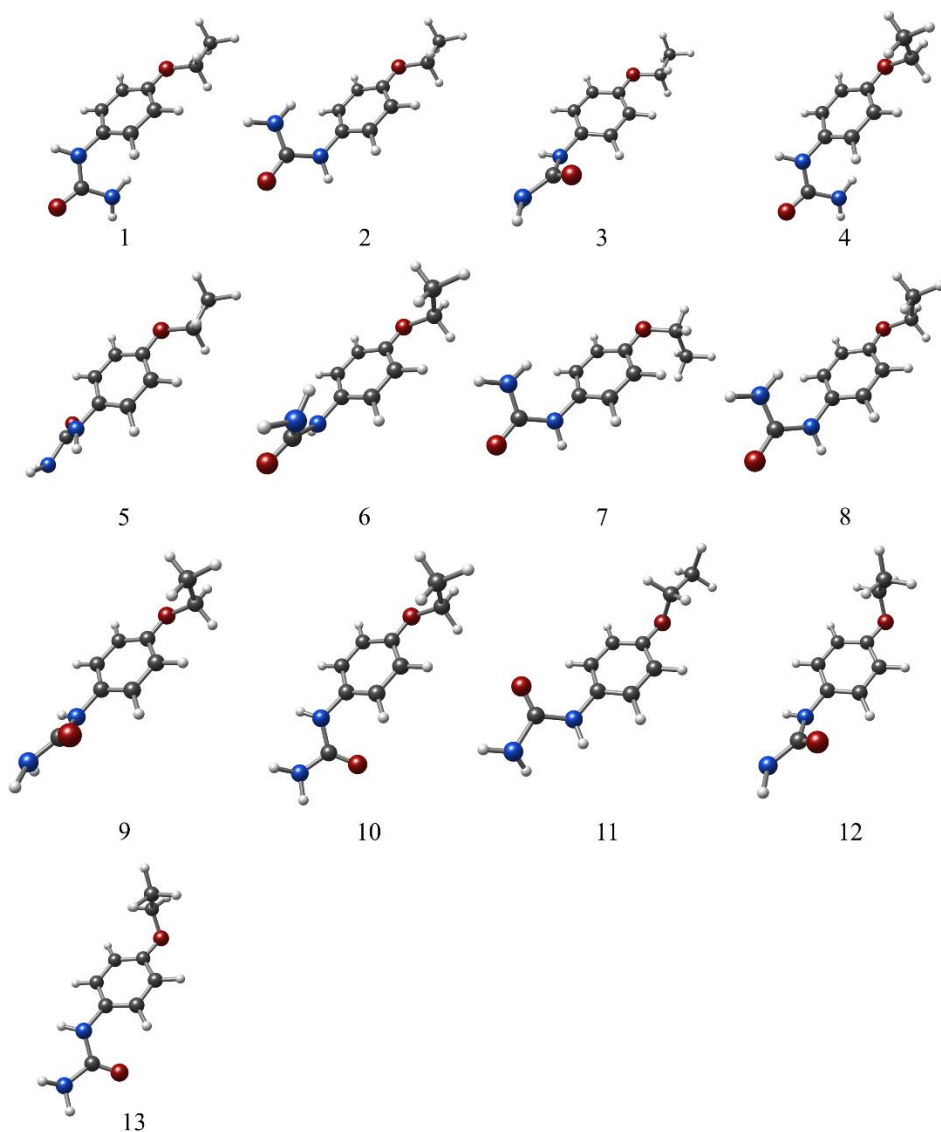


Figure 1. The 13 low-lying structures of dulcin.

Table 1. Calculated spectroscopic parameters for the dulcin conformers at the MP2/ 6-311++G (d,p) level of theory.

	1	2	3	4	5	6	7	8	9	10	11	12	13
A ^a	2787	3068	2832	2394	3205	2122	2691	2321	2143	2361	2726	2172	2584
B	312	304	311	339	302	357	332	337	356	341	311	352	334
C	293	290	286	322	284	326	313	329	321	315	295	335	320
μ_a	4.9	5.1	0.6	4.6	0.0	5.0	5.0	5.2	1.0	0.4	1.4	1.3	0.3
μ_b	0.9	0.8	1.4	1.2	3.7	0.4	0.5	0.2	1.4	1.0	2.6	2.8	3.9
μ_c	0.9	1.5	1.9	1.1	1.6	1.0	1.5	1.3	1.0	2.8	0.2	1.1	2.7
ΔE^c	0	21	399	356	452	399	386	394	733	752	888	850	924
ΔE_{zpe}^d	0	6	374	414	421	438	442	450	786	805	882	909	964
ΔG^e	9	0	399	489	442	497	530	534	875	916	446	895	807

[a] A, B, and C represent the rotational constants (in MHz). [b] μ_a , μ_b and μ_c are the electric dipole moment components (in D). [c] Relative energies (in cm^{-1}) with respect to the global minimum. [d] Relative energies (in cm^{-1}) with respect to the global minimum, taking into account the zero-point energy (ZPE). [e] Gibbs energies (in cm^{-1}) calculated at 298 K.

Rotational spectrum

Figure 2 shows the broadband rotational spectrum of dulcin in the 2-8 GHz range obtained with our LA-CP-FTMW spectrometer. Initially, lines corresponding to known photofragment species and water clusters were identified and removed [14,15]. The remaining spectrum consisted in very intense lines, most likely due to a predominant conformer. To ease the search for the rotameric species, the calculated rotational constants in Table 1 were used as a starting point. Our first search started from the most stable species, which also has a strong μ_a dipole moment. It was easy to observe intense R-branch *a*-type transitions of a first rotamer (see Figures 2 and 3), separated approximately *B* + *C* with an approximate spacing of 590 MHz, and corresponding to values of *J* ranging from *J*=3 to *J*=12 [19]. Tentative assignments were made on the basis of the close match-up of several strong lines in the spectrum, and a total of 59 *a*-type transitions were fitted using a rigid rotor Hamiltonian by using the nonlinear least-squares fit program developed by Picket [20,21]. In the next step, the newly obtained rotational constants were used to predict a more precise simulated spectrum. Weak *c*-type transitions were located and included in the fit. The obtained rotational constants for this first rotamer are collected in Table 2, and all the lines are collected in the Table AIII-1.

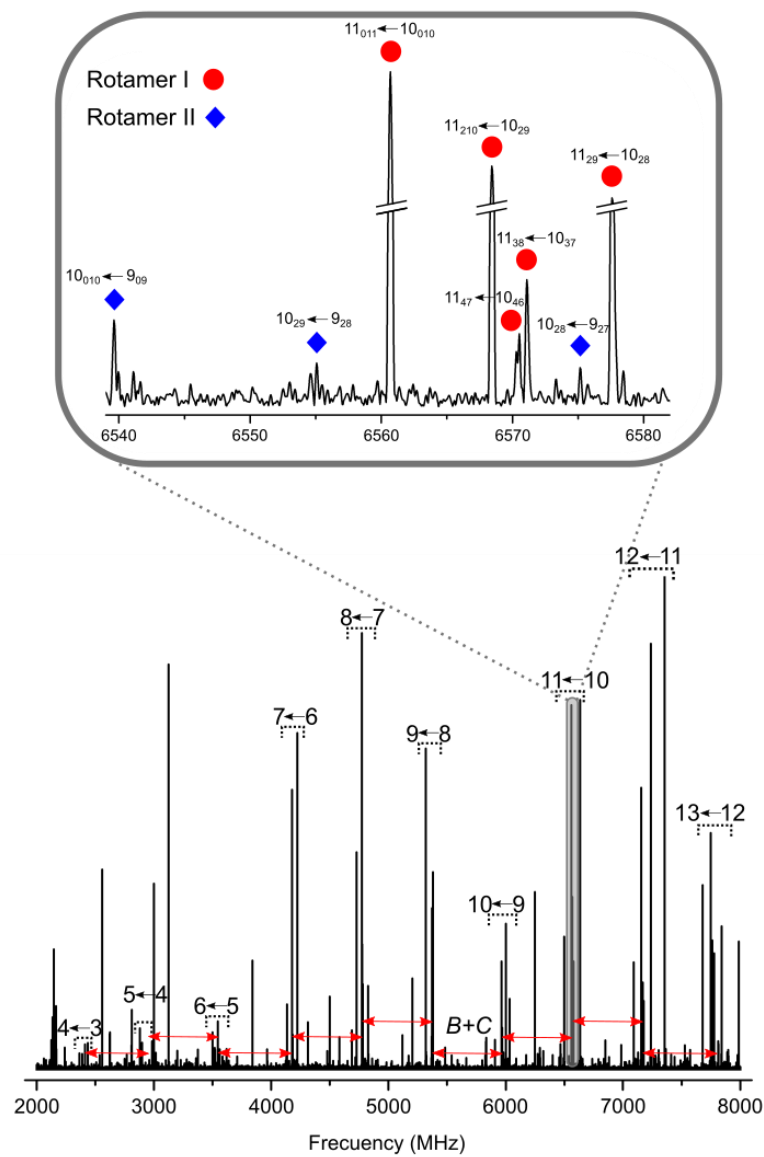


Figure 2. Broadband rotational spectrum of dulcin from 2 to 8 GHz. The *a*-type R-branch transitions separated approximately *B*+*C* are highlighted. The upper part details a zoomed-in section of rotational spectrum in the 6540 to 6580 MHz range showing some selected transitions for the two rotamers observed.

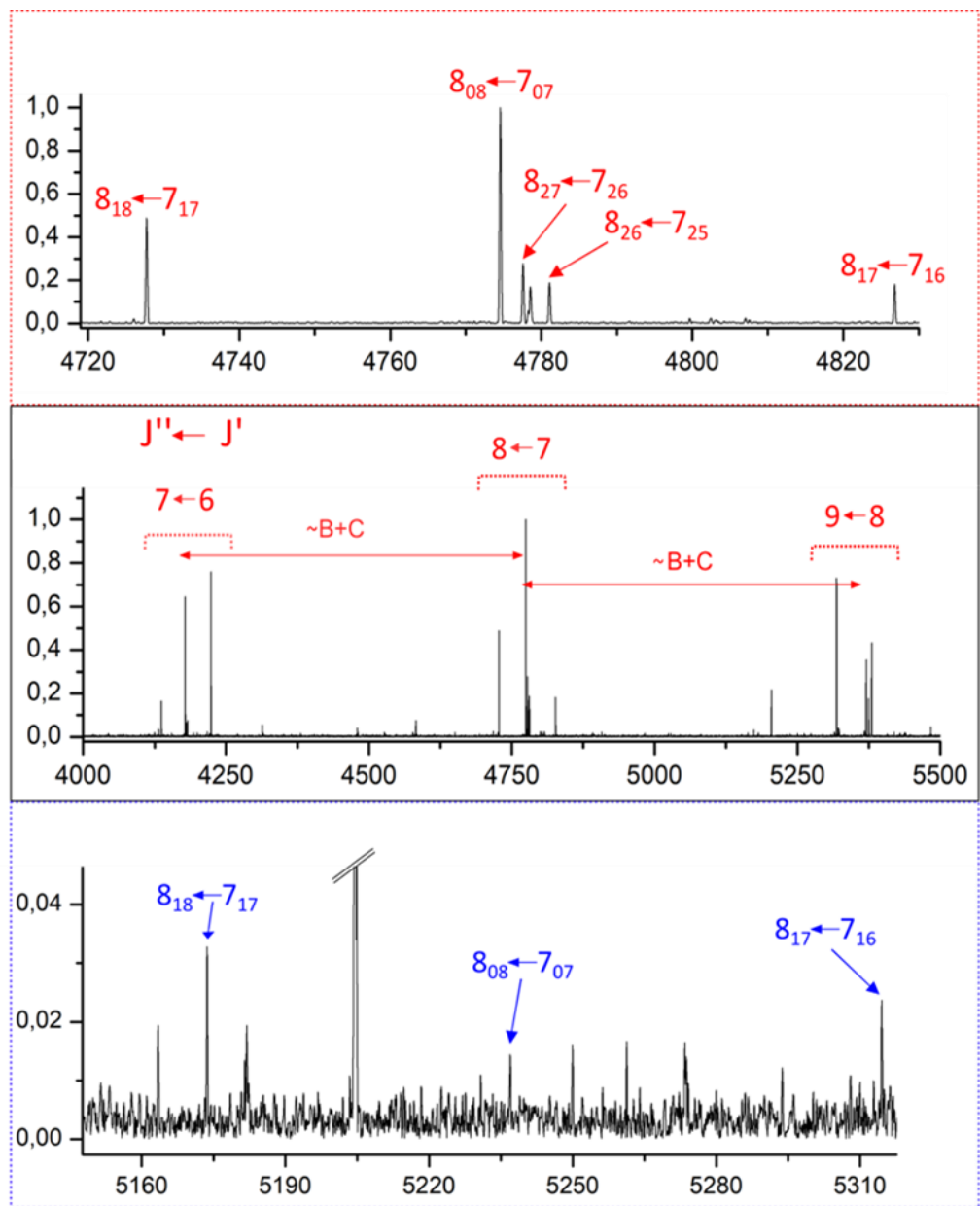


Figure 3. Top panel: Section of the broadband rotational spectrum of rotamer II in the 4 to 5.5 GHz range. The μ_a -type R-branch transitions are highlighted in red and show a spacing corresponding to the $B+C$ value. Middle panel: zoomed-in section of the $J''=8 \leftarrow J'=7$ μ_a -type R-branch transition (in red) for conformer II. Lower panel: zoomed-in section of the $J''=8 \leftarrow J'=7$ μ_a -type R-branch transition (in blue) for rotamer IV.

After identifying all the lines corresponding to rotamer I, several weak lines were still present in the spectrum, so we continued searching for other conformers. Another a -type progression was observed, and a total of 12 transitions were fitted obtaining the rotational constants for a second rotameric species shown in the Table 2 and all the lines are collected in the Table AIII-2. No b or c -type transitions were observed. After removing their corresponding peaks, no more lines remained in the spectrum indicating the absence of more species in the rotational spectrum.

Table 2. Experimental and calculated spectroscopic parameters for the dulcin at the MP2/B3LYP-D3 level of theory and using the 6-311++G (d,p) basis set.

	Experimental		Theory			
	Rotamer I	Rotamer II	1	2	3	4
<i>A</i> ^[a]	3052.1532(53) ^[h]	2413.98(76)	2787/2814	3068/3113	2832/2893	2394/2387
<i>B</i>	304.82621(33)	336.70893(42)	312/310	304/303	311/307	339/336
<i>C</i>	292.43629(32)	319.08422(42)	292/290	290/288	286/279	322/316
ΔJ ^[b]	0.00589(93)	-0.0117(17)				
Δ_{JK}	0.128(17)	0.135(84)				
$ \mu_a $	Observed	Observed	4.9/5.1	5.1/5.4	0.6/0.5	4.6/5.1
$ \mu_b $	0.9/1.2	0.8/0.5	1.4/2.3	1.2/0.9
$ \mu_c $	Observed	...	0.9/1.0	1.5/1.5	1.9/1.1	1.1/1.3
$\sigma^{[c]}$	9.1	6.3				
<i>N</i> ^[d]	52	12				
ΔE ^[e]		0/0	21/7	399/331	356/339	
ΔE_{ZPE} ^[f]		0/2.4	6/0	374/337	414/375	
ΔG ^[g]		9/2	0/2	399/333	489/333	

[a] *A*, *B*, and *C* represent the rotational constants (in MHz). [b] Δ_J and Δ_{JK} are the quartic centrifugal distortion constants (in KHz); μ_a , μ_b and μ_c are the electric dipole moment components (in D). [c] RMS deviation of the fit (in kHz). [d] Number of measured transitions [e] Relative energies (in cm^{-1}) with respect to the global minimum. [f] Relative energies (in cm^{-1}) with respect to the global minimum, taking into account the zero-point energy (ZPE). [g] Gibbs energies (in cm^{-1}) calculated at 298 K. [h] Standard error in parentheses in units of the last digit.

Conformational identification

Conformational identification can be achieved by comparing the experimental and theoretical spectroscopic parameters. Table 2 shows a comparison between the experimental rotational constants of the two rotamers detected and the values predicted for the four most stable species below 500 cm^{-1} . The conformational identification was straightforward: as can be seen, there is an excellent agreement between the experimental rotational constants of rotamer I and the conformer labeled as conformer 2. This structure is predicted as one of the most stable species. Additionally, the values of the dipole moment are consistent with the observation of strong *a*-type lines and weaker *c*-type transitions. Regarding to rotamer II, its rotational constants are in good agreement with conformer 4, which is considerably higher in energy. The selection rules and energetics confirm such assignment: its population is predicted to be low and it has a high dipole moment for the *a*-type transitions. This is in good agreement with the weak lines observed for the *a*-type transition, as well as with the non-detection of the *b*- and *c*-type transitions.

Conformational relaxation

As can be seen in Table 2, calculations point to two stable species (isoenergetic) and another two weak conformers. Because only two species are present in the rotational spectrum, one showing intense lines and another one with weak transitions, we looked for an explanation for the absence of structures I and III. Structure I is isoenergetic with structure II and has a strong μ_a dipole moment so its population should be high. Thus, strong *a*-type rotational transitions should be expected. In order to rule out theoretical

inaccuracies, the structures were optimized using B3LYP-GD3. Using this methodology, structures 1 and 2 are still predicted as isoenergetic (see Table 2), but the energetics values are reversed and structure 2 appears as the global minimum in good agreement with the experiment. Nevertheless, this fact only explains the correct energetically ordering but does not explain the absence of structure 1, which should be considerably populated.

It is well known that a supersonic expansion can change the conformational distribution during the cooling process. Due to the collisions with the carrier gas, some or all of the population of a higher-energy conformer can interconvert to a lower-energy conformer, distorting the thermodynamic data obtained from the experiment and giving rise to *missing conformers* [22]. This conformational lost usually happens when the isomerization barrier is low enough [23]. To test whether isomerization from conformer 1 into 2 is taking place, the potential energy surface connecting both structures was explored by rotating the CCNC and NCNH torsional angles using the B3LYP-GD3 method. As shown in Figure 4, the calculated interconversion barrier is very low, about 140 cm^{-1} , indicating that there is a large transfer from the population of conformer 1 into conformer 2, which most likely precludes its detection.

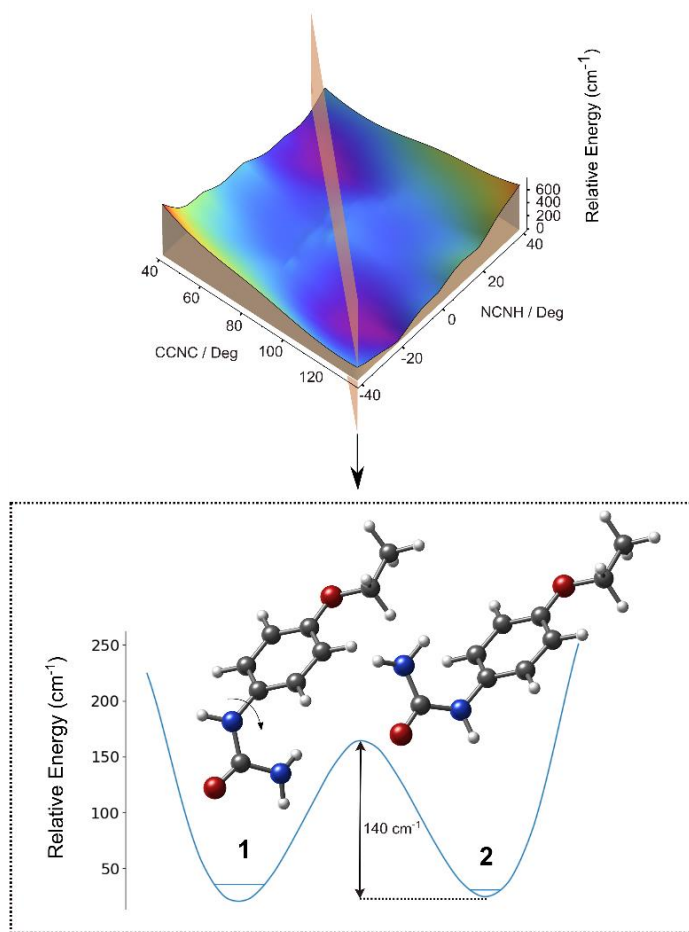


Figure 4. The potential energy surface (PES) of dulcin rotating the torsional angles C-N-C and N-C-N-H, calculated using the B3LYP-GD3 method. The interconversion barrier is low, resulting in a relaxation of conformer 1 to 2.

Regarding to conformer 3, we did not find any obvious interconversion barrier and, therefore, the explanation for its non-detection must be due to other facts. Taking into accounts its energetics, the population in the jet should be very close to that of conformer 4. But because its dipole moment is significantly lower than that of conformer 4, which already showed very weak rotational transitions, altogether its signal probably falls below the sensitivity of the instrument.

Structure-property relationship of dulcin and its sweetness

In order to study the relationship between the observed structures of dulcin with its sweetness, we rationalized the geometries in terms of the sweetness theory. Assuming a total conformational interconversion between conformers I and II, the experimental population of both conformers make up ~81.1 % of the abundance of the conformational landscape of dulcin. This is in good agreement with the calculated populations of the two most stable structures (~45% for each). Thus, despite that conformer I has not been detected, it should be taken into account. Furthermore, it is very likely that, at room temperature, both conformers would be interconverting between them continuously. The most stable conformer of dulcin is stabilized through an intramolecular interaction between the -NH₂ and the phenyl ring. Additionally, the -NH-CO-NH₂ group is disposed almost perpendicular to the aromatic ring. This geometry is also affected by the donor contribution of the alkoxy group. Regarding the other stable conformer, conformer I, its structure is similar to conformer II but with the urea group located opposite to the alkoxy group.

As shown in Figure 5, the AH-B pair could correspond to the -CO-NH₂ group: the proton accepting species (B) would be the -CO- group, and the donor entity (AH) would be NH₂ group. Alternatively, a second glucophore unit is proposed with the -NH-CO-moiety of the molecule. The calculated distance for the AH-B system is 2.3 Å in good agreement with the proposed distances for the AH-B pair according to the sweetness theory. Therefore, both possibilities are consistent with the contact points and distances proposed by this theory. Regarding to the γ point, which is a critical point for stereo-selectivity, is the alkoxy group and should distinguish between the two positions of the urea group. This contact point is in good agreement with that proposed by Peer and coworkers [5]. It is also interesting to note that, as explained above, at room temperature these two structures should interconvert continuously due to the low interconversion barrier. This maximizes the probability of interacting with the receptor and could explain why this molecule has such a degree of sweetness. Thus, the structures of dulcin meet the requirements of the sweetness theory proposed by Shallenberger-Acree-Kier.

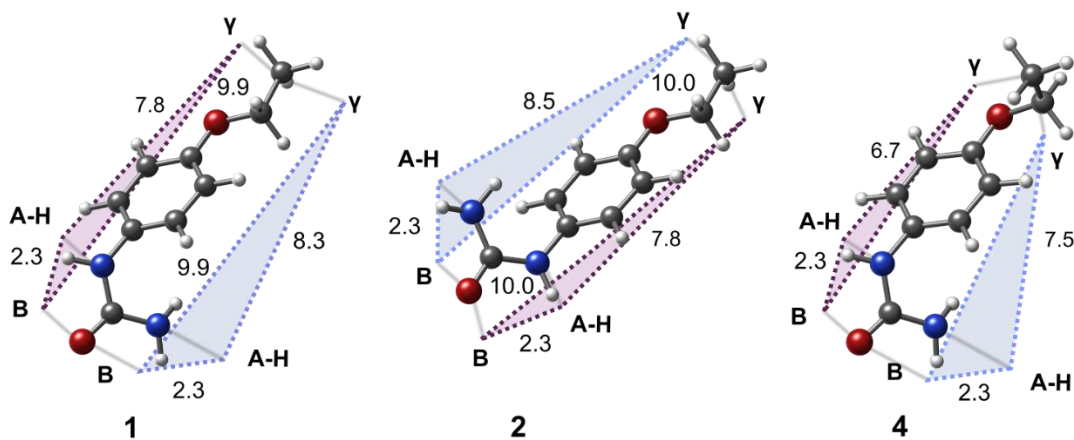


Figure 5. The three detected conformers of dulcin. The sweetness triangle is detailed for each conformer. The numbers (given in Angstrom) indicate the distances between the atoms in the triangle.

5.3. Conclusion

The conformational panorama of dulcin has been investigated using LA-CP-FTMW spectroscopy in the isolated conditions of a supersonic expansion. Out of the four stable conformers, two of them have been unequivocally identified in the rotational spectra. One of the structures is “missing” due to conformational interconversion. The other conformer probably falls below the sensitivity due to its low abundance and low dipole moments. The two most stable structures are stabilized through an intramolecular interaction between the NH_2 group and the π electronic cloud of the phenyl ring group. The second detected conformer presents a similar arrangement but with the alkoxy group rotated out-of-plane from the phenyl group.

Two triangles of sweetness are proposed for the conformers of dulcin that are in accordance with the theory of sweetness proposed of Shallenberger Acree-Kier. We observe a good correspondence between the $AH/B/\gamma$ point in the detected conformers and the distances proposed in the sweetness theory. This knowledge in the polyurea families could serve to validate the sweetness theory and to help in the design of new artificial sweeteners

5.4. References

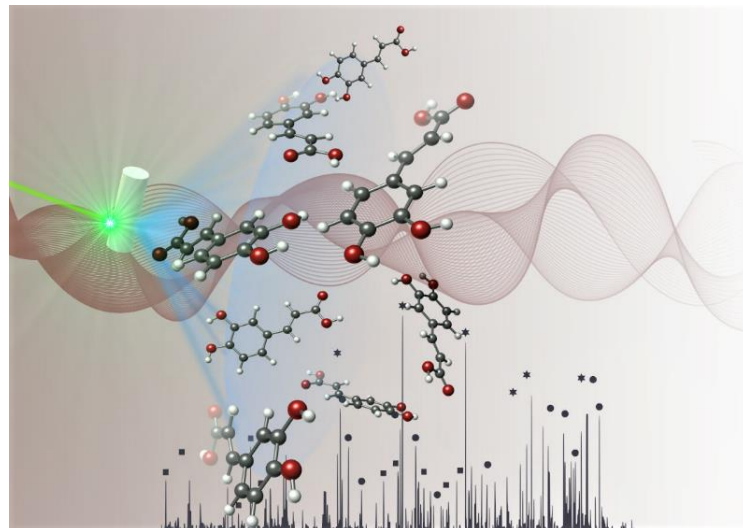
1. Van Der Wel, H.; Van Der Heijden, A.; Peer, H.G. Sweeteners. *Food Rev. Int.* **1987**, *3*, 193–268.
2. Berlinerblau, J. Über Der Einwirkung von Chlorcyan Auf Ortho Und Para-Amidophenetole. *Teubner: Dresden* **1884**, *11*.
3. Berlinerblau, J. J. Prakt. Chemie. **1884**, *30*, 103.
4. Siedler, P. Artificial Sweeteners, Especially Dulcin. *Chemiker-Zeitung* **1916**, *40*, 853–855.
5. Heijden, A. Van Der; Wei, H. Van Der; Peer, H.G. Structure-Activity Relationships in Sweeteners . **1985**, *10*, 73–88.
6. Shallenberger, R.S. *Taste Chemistry*; **1993**.
7. Goldsmith, R.H. Dulcin: A Centennial Perspective. *J. Forensic Sci.* **1986**, *31*.
8. Fitzhugh, O.G.; Nelson, A.A.; Frawley, J.P. A Comparison of the Chronic Toxicities of Synthetic Sweetening Agents. *J. Am. Pharm. Assoc. Am. Pharm. Assoc. (Baltim).* **1951**, *40*, 583–586.
9. Ikeda, I.; Omori, Y.; Ika, S.; Shinoda, M.; Tsuzi, K. Studies on Chronic. Toxicity of Dulcin. *Food Hyg. Saf. Sci. (Shokuhin Eiseigaku Zasshi)* **1960**, *62*–69.
10. *Alternative Sweetners*; Nabors, L.O., Ed.; Fourth Edition.; **2011**.
11. Uesawa, Y.; Staines, A.G.; Lockley, D.; Mohri, K.; Burchell, B. Identification of the Human Liver UDP-Glucuronosyltransferase Involved in the Metabolism of p-Ethoxyphenylurea (Dulcin). *Arch. Toxicol.* **2007**, *81*, 163–168.
12. Frollo, N.; Lloret, E.; Martinez, J.-M.; Faurion, A. Cross-Adaptation and Molecular Modeling Study of Receptor Mechanisms Common to Four Taste Stimuli in Humans. *Chem. Senses* **1998**, *23*, 197–206.
13. Nelson, G.; Hoon, M.A.; Chandrashekar, J.; Zhang, Y.; Ryba, N.J.P.; Zuker, C.S. Mammalian Sweet Taste Receptors Insight to Our Understanding of Chemosensory Discrimination of Two Novel Families of G Protein-Coupled Receptors Lastly, We Show That the Patterns of T1R Expression. *Cell* **2001**, *106*, 381–390.
14. Ciajolo, M.R.; Lelj, F.; Tancredi, T.; Temussi, P.A.; Tuzi, A. Interaction of Conformationally Flexible Agonists with the Active Site of Sweet Taste. A Study of Arylureas. *J. Med. Chem.* **1983**, *26*, 1060–1065.
15. Brown, G.G.; Dian, B.C.; Douglass, K.O.; Geyer, S.M.; Pate, B.H. The Rotational Spectrum of Epifluorohydrin Measured by Chirped-Pulse Fourier Transform Microwave Spectroscopy. *J. Mol. Spectrosc.* **2006**, *238*, 200–212.
16. Park, G.B.; Field, R.W.; Park, G.B.; Field, R.W. Perspective : The First Ten Years of Broadband Chirped Pulse Fourier Transform Microwave. **2016**, *200901*.
17. León, I.; Alonso, E.R.; Mata, S.; Alonso, J.L. Shape of Testosterone. *J. Phys. Chem. Lett.* **2021**, *12*, 6983–6987.
18. Kolesniková, L.; León, I.; Alonso, E.R.; Mata, S.; Alonso, J.L. An Innovative Approach for the Generation of Species of the Interstellar Medium. *Angew. Chemie* **2021**, *133*, 24666–24671.
19. Plusquellic, D.F. JB95 Spectral Fitting Program Available online: <https://www.nist.gov/services-resources/software/jb95-spectral-fitting-program>.

20. Gordy, W.; Cook, R.L. *Microwave Molecular Spectroscopy*; John Wiley & Sons, Ed.; New York, 1984;
21. Pickett, H.M. The Fitting and Prediction of Vibration-Rotation Spectra with Spin Interactions. *J. Mol. Spectrosc.* **1991**, *148*, 371–377, doi:10.1016/0022-2852(91)90393-O.
22. Miller, T.F.; Clary, D.C.; Meijer, A.J.H.M. Collision-Induced Conformational Changes in Glycine. *J. Chem. Phys* **2005**, *122*, 244323.
23. Cabezas, C.; Varela, M.; Alonso, J.L. The Structure of the Elusive Simplest Dipeptide Gly-Gly. *Angew. Chemie Int. Ed.* **2017**, *56*, 6420–6425.

6. Chapter

Unveiling the Eight Forms of Caffeic Acid

Abstract: In this chapter the complete conformational analysis of caffeic acid, an exceptionally versatile pharmacophore, is studied by means of laser ablation chirped-pulse Fourier transform microwave spectroscopy. The whole conformational space consists of eight distinct rotameric species, and is fully deciphered based on a thorough inquiry of the trend of the rotational constants supported by high-level computations. Additionally, this structural information should help to elucidate the mechanisms underlying the biological and pharmacological activity shown by this archetypal hydroxycinnamic acid.



6.1. Introduction

In the last decades, natural products have been presented as essential scaffolds in the drug design and discovery process [1]. Despite a myriad of small organic and biomolecules have been employed in the search for potential therapeutical agents, phenolic acids stand above the rest [2–5]. This family of compounds is widespread in nature with over 50,000 diverse species identified so far [6]. They are originated mainly in plants, which synthesize them in large quantities as a product of their secondary metabolism [7].

Owing to their noticeable chemical heterogeneity, these molecules are classified into different groups according to their molecular structure [8]. Among them, of paramount importance are hydroxycinnamic acids, which are present in nearly all plants [9–11]. The major representative hydroxycinnamic acid is caffeic acid (trans- 3-(3,4-dihydroxyphenyl)prop-2-enoic acid). Despite it is not used as a sweetener, it is commonly found in food as several simple derivatives such as esters and a mides [12,13], and can be used as a dietary antioxidant. Therefore, it is interesting to include it in the prese

nts thesis. Additionally, the pharmacological profile of this molecule and their derivatives is quite broad, highlighting their potential use as anti-cancerogenous [14–17] and anti-inflammatory agents [18–20], as well as their remarkable antioxidant and scavenging activity [21–24].

It is well known that the aforementioned biomedical properties mainly rely on the corresponding structure-activity relationship [25]. Hence, deciphering the shape of these species at the molecular scale appears as a very stimulating target to better understand the mechanisms underlying the biological activity shown by certain phenolic acids. In this context, several theoretical and experimental structural studies have been devoted to the study of this archetypal hydroxycinnamic acid [26–30]. However, these investigations are limited to the condensed phase and, therefore, the structural information might be altered due to the formation of intermolecular interactions with the surrounding media. Thus, a thorough investigation under the isolation conditions of the gas phase should provide compelling information regarding the shape, but most importantly, the intrinsic conformational features of caffeic acid. Within this framework, while some dietary antioxidants (i.e., vitamin C) have received considerable attention [31], relatively little is known about the three-dimensional structure of several plant-derived polyphenolic compounds, such as caffeic acid.

High-resolution microwave spectroscopy coupled with an ultra-fast laser ablation vaporization system has demonstrated to be a robust tool in the investigation of the conformational landscape of other phenolic acids, such as *trans*-cinnamic and *trans-p*-coumaric [32]. In the current chapter, we aim to perform a comprehensive rotational spectroscopic study of caffeic acid, which has remained as an elusive target so far due to its high melting point (213 °C). These findings should be of interest to unveil its role as a versatile pharmacophore and could lead to a search for more effective caffeic acid derivatives.

6.2. Results and Discussion

Conformational panorama

The complete conformational panorama consists of eight distinct conformations of remarkable stability, all of them below 400 cm^{-1} relative to the global minimum. The structures are collected in Figure 1, and we list the theoretical spectroscopic constants for all plausible conformers of caffeic acid in Table 1. The eight candidate structures can be sorted in two different groups or families, labelled as *syn* and *anti*, according to the different orientation of the pendant ring with respect to the *meta*-OH group (see Figure 1). This event gives rise to a distinctive and substantial change in their moments of inertia, which is further transferred into the rotational constants. Moreover, for each family, four different conformers arise from a variation in the disposition of the terminal carboxyl group (*cis* or *trans*) or a change in the orientation of the catechol hydroxyl group (clockwise, *a*, and counterclockwise, *b*). These subtle structural changes are expected to yield a slight yet specific variation in the values of the rotational constants, significant enough to allow conclusive discrimination in case all the structures are irrefutably characterized.

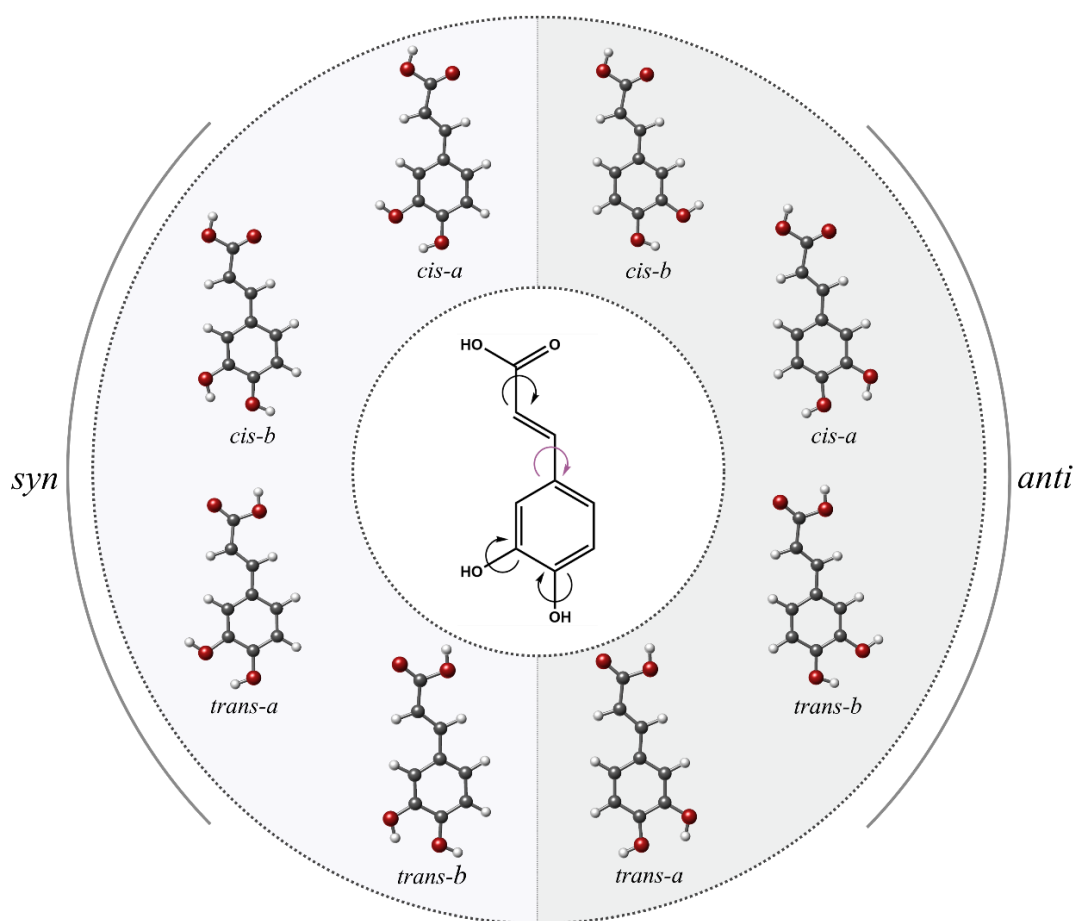


Figure 1. The eight lowest-in-energy conformers of caffeic acid predicted by theoretical calculations.

Table 1. Calculated spectroscopic parameters for the caffeic acid conformers.

Parameters	Syn-				Anti-			
	<i>cis-a</i>	<i>cis-b</i>	<i>trans-a</i>	<i>trans-b</i>	<i>cis-b</i>	<i>cis-a</i>	<i>trans-b</i>	<i>trans-a</i>
<i>A</i> ^[a]	2269.4	2269.4	2279.1	2279.6	2479.6	2479.1	2463.5	2463.4
<i>B</i>	321.5	322.1	323.1	323.7	309.6	309.9	312.2	312.5
<i>C</i>	281.6	282.1	283.0	283.4	275.2	275.4	277.1	277.3
μ_a	1.7	4.2	2.1	4.6	2.0	3.3	2.8	4.2
μ_b	3.0	1.2	0.2	4.0	0.9	3.8	3.5	1.2
μ_c	0.0	0.0	0.0	0.0	0.0	0.0	0.0	0.0
$\Delta E_{ZPE}^{[b]}$	0	139	145	334	65	213	276	364
$\Delta G^{[c]}$	0	161	133	336	44	135	223	364

[a] *A*, *B*, and *C* represent the rotational constants (in MHz); μ_a , μ_b and μ_c are the electric dipole moment components (in D). [b] Relative energies (in cm⁻¹) with respect to the global minimum, taking into account the zero point energy (ZPE). [c] Gibbs energies (in cm⁻¹) were calculated at 298 K. Theoretical computations were carried out at the B3LYP-GD3/ 6-311++G (d, p) level of theory

Broadband rotational spectrum

Figure 2 shows the rotational spectrum of the caffeic acid obtained in the 2.75-6.5 GHz range. As can be seen, the spectrum is extremely dense. We first removed the known electronic lines from the spectra as they hindered our analysis [32, 33]. Then, after a careful inspection, we manage to identify strong *b*-type *R*-branch progressions, which clearly dominate the spectra, and were ascribed to a first rotamer (rotamer I). We extended the analysis to other *b*-type *Q*-branches and weaker *a*-type *R*-branch lines and performed the corresponding fit to a rigid-rotor Hamiltonian. The resulting experimental spectroscopic constants are presented in the first column of Table 2.

Table 2. Experimental spectroscopic parameters for the caffeic acid rotamers I-IV.

	Experimental			
	Rotamer I	Rotamer II	Rotamer III	Rotamer IV
<i>A</i> ^[a]	2262.22348 (78) ^[f]	2263.95 (20)	2271.20 (49)	2272.9750 (10)
<i>B</i>	321.88280 (31)	322.45623 (55)	323.51160 (12)	324.00522 (45)
<i>C</i>	281.96625 (23)	282.4286 (54)	283.36153 (98)	283.77359 (41)
$ \mu_a $	Observed	Observed	Observed	Observed
$ \mu_b $	Observed	-	-	Observed
$ \mu_c $	-	-	-	-
$\Delta^{[c]}$	-1.1	-1.1	-1.2	-1.2
$\sigma^{[d]}$	14.4	11.6	18.2	14.9
<i>N</i> ^[e]	55	16	14	27

[a] *A*, *B*, and *C* represent the rotational constants (in MHz). [b] μ_a , μ_b , and μ_c are the electric dipole moment components. [c] $\Delta = I_c - I_a - I_b$ in uÅ². Conversion factor: 505379,07 uÅ² MHz. [d] rms deviation of the fit (in KHz). [e] Number of fitted transitions. [f] Standard error in parentheses in units of the last digit.

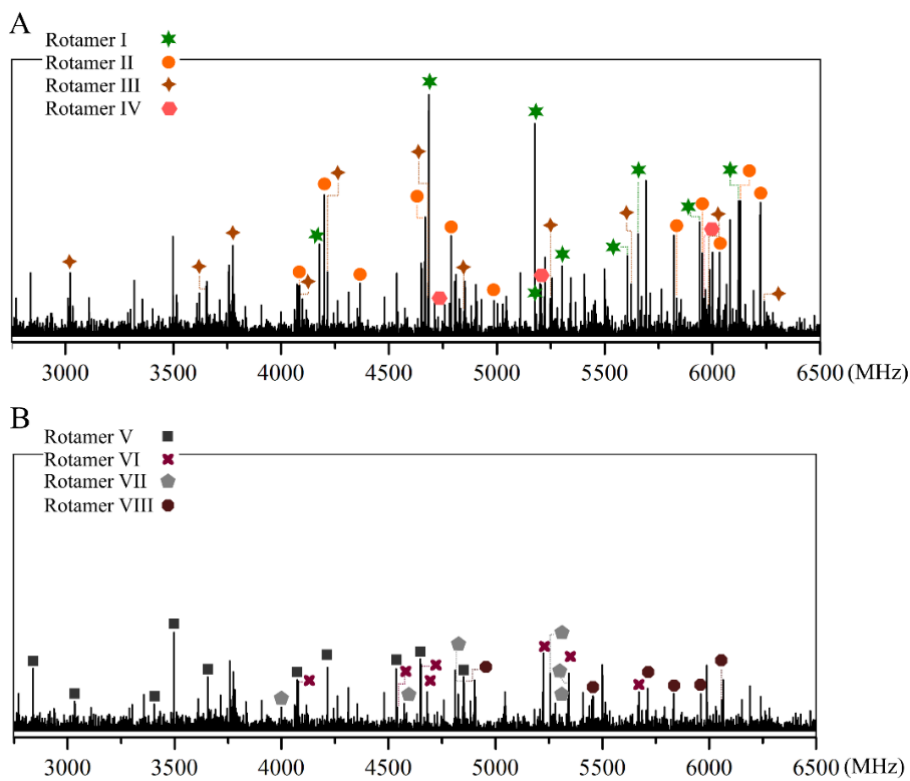


Figure 2. a) Broadband CP-FTMW rotational spectrum of caffeic acid from 2.75 to 6.5 GHz showing characteristic *R*-branch progressions for rotamers I-IV; b) Remaining spectrum resulting from removing the lines ascribable to rotamers I-IV. Transitions belonging to rotamers V-VIII are depicted. Intensity is given in arbitrary units.

We then searched for lines that fall in the vicinity of those belonging to rotamer I, and succeeded to identify several progressions of *a*-type transitions attributable to three different rotamers, labelled as II, III and IV. After a careful exploration of the spectrum, several *b*-type transitions were also measured for rotamer IV. Nevertheless, it was not possible to locate *c*-type transitions, which is in accordance with the $\mu_c = 0$ predicted dipole moment component for all plausible conformers of caffeic acid (see Table 1). The rotational constants derived from the corresponding rigid rotor analyses are listed in the second, third and fourth columns of Table 2, respectively. Additionally, all the lines for those rotamers are collected in the Tables AIV-1 to AIV-4.

Afterward, we removed the lines belonging to the four rotamers. After a closer examination of the remaining spectrum, we were able to identify several *a*-type progressions ascribable to four new rotamers, labelled as V, VI, VII and VIII. For rotamers VI and VII, we extended the analysis to other *b*-type lines; however, no *c*-type spectrum was observed for any of the rotameric species. We list in the four last columns of Table 3 the experimental spectroscopic parameters obtained for rotamers V-VIII, while all the lines for those species are collected in the Tables AIV-5 to AIV-8.

Table 3. Experimental spectroscopic parameters for the caffeic acid rotamers V-VIII.

	Experimental			
	Rotamer V	Rotamer VI	Rotamer VII	Rotamer VIII
$A^{[a]}$	2473.82 (67) ^[f]	2474.36056 (90)	2456.980 (13)	2458.81 (93)
B	309.7585 (85)	310.02508 (40)	312.2982 (48)	312.6236 (11)
C	275.4663 (83)	275.70948 (25)	277.28203 (49)	277.5706 (12)
$ \mu_a $	Observed	Observed	Observed	Observed
$ \mu_b $	-	Observed	Observed	-
$ \mu_c $	-	-	-	-
$\Delta^{[c]}$	-1.2	-1.4	-1.3	-1.4
$\sigma^{[d]}$	13.9	14.3	15.4	16.1
$N^{[e]}$	14	40	22	7

[a] A , B , and C represent the rotational constants (in MHz). [b] μ_a , μ_b , and μ_c are the electric dipole moment components. [c] $\Delta = I_c - I_a - I_b$ in $\text{u}\text{\AA}^2$. Conversion factor: 505379,07 $\text{u}\text{\AA}^2$ MHz. [d] rms deviation of the fit (in KHz). [e] Number of fitted transitions. [f] Standard error in parentheses in units of the last digit.

Conformational assignment

At first glance, the values of the rotational constants of the eight rotamers are coherent with those for a sizeable molecular species such as caffeic acid. In fact, it is easy to distinguish that rotamers I to IV correspond to the *syn* family, while rotamers V-VIII belong to the *anti*-species. However, within each group, no immediate conclusion can be obtained from the values of the rotational constants alone, since they are extremely close for the conformers belonging to each category. Nevertheless, we can achieve a complete conformational identification of the observed rotamers based on a thorough investigation of the trend of the rotational constant's values compared to the predicted changes. Hence, when going from rotamer I to rotamer II, the experimental changes in the rotational constants are $\Delta A = 1.7$ MHz, $\Delta B = 0.6$ MHz, and $\Delta C = 0.5$ MHz, which perfectly match with the theoretically predicted ones of $\Delta A = 0.0$ MHz, $\Delta B = 0.6$ MHz, and $\Delta C = 0.5$ MHz in going from *syn-cis-a* to *syn-cis-b* (see Figure 3). Therefore, it points to the identification of rotamer I as *syn-cis-a* and rotamer II as *syn-cis-b*, respectively. Note that the slightly higher difference in the value of the A rotational constant can be easily rationalized in terms of the nearly prolate nature of caffeic acid. Afterward, in Figure 3 it is shown that the predicted changes in rotational constants when going from the *syn-cis-b* to *syn-trans-a* conformer are in excellent accordance with those derived from the experimental values of Table 2 when going from rotamer II to rotamer III, thus leading again to the conclusion that rotamer II is *syn-cis-b*. What is more, the experimental changes in rotational constants between rotamers III and IV are only coherent with those calculated between the *syn-trans-a* and *syn-trans-b* caffeic acid. Additionally, the dipole moment selection rules allow us to further corroborate the identification of rotamer I and IV as conformers *syn-cis-a* and *syn-trans-b*.

For all four *anti*-conformers, these structures differ from the *syn*-conformers in the orientation of the carboxylic group (see Figure 1), which is translated into a significant change in the rotational constant's values. However, similar to the *syn* conformers, we need to inspect firstly the trend of the rotational constant's values to decipher the subtle structural modifications between each *anti*-conformer and, therefore, attain a definite conformational identification (see Table 3). For the *anti*-family, these minimal differences (i.e. the reorganization of the OH groups) produces once more distinctive shifts in rotational constants, which serve as a conclusive proof to decode each structure while “travelling” between conformers. Therefore, we can identify the relative *anti*-energy minimum, *anti-cis-b*, as rotamer V and, subsequently, tie rotamers VI, VII and VIII to conformers *anti-cis-a*, *anti-trans-b* and *anti-trans-a*, respectively. The small experimental changes observed in the values of the rotational constants are again fully in harmony with the calculated shifts at the B3LYP-GD3 level (see Tables 1 to 3), irrefutably corroborating the conformational identification.

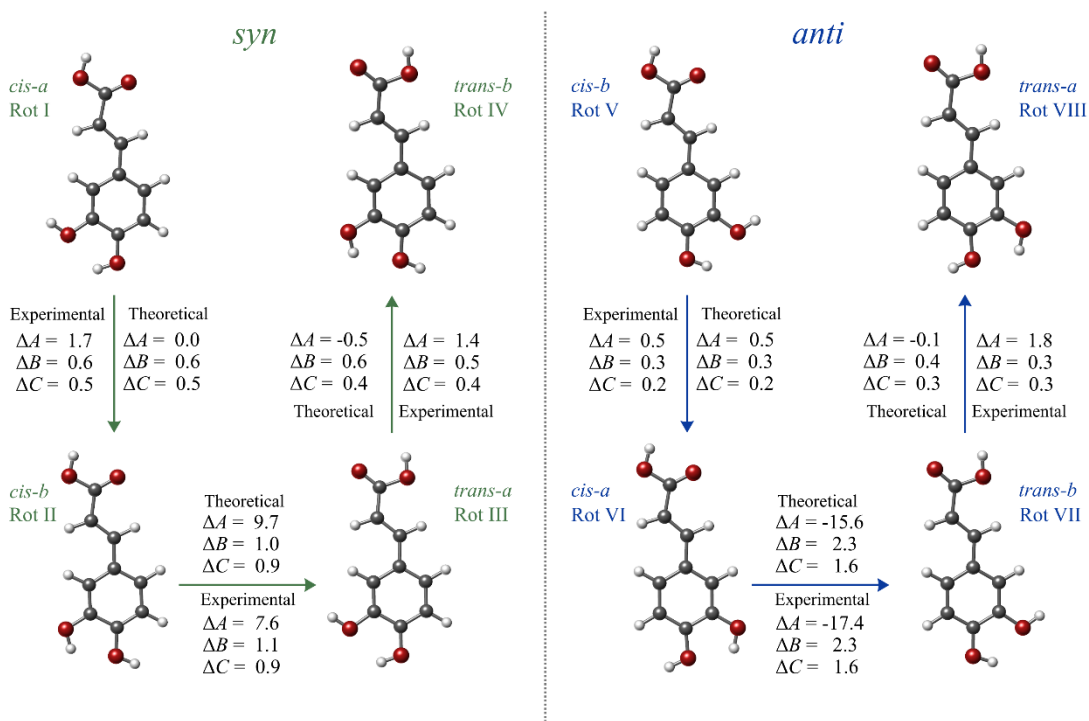


Figure 3. Experimental and calculated changes in the values of the rotational constants (in MHz) induced by different orientations of the catechol hydroxyl groups or the carboxylic group.

Structure-property relationship

A final remark regarding the structure-activity relationship of caffeic acid can be derived on the basis of the observation of its complete conformational panorama. All the observed conformers exhibit small negative values of the inertial defect, varying between -1.389 and -1.104 $\text{u}\text{\AA}^2$, which implies that all species are actually planar but exhibit a low

out-of-plane vibration. This small variation in the planarity of the conformers is mainly due to the C(ph)-C-C-COOH torsion [34–37].

It is known that some of the most important features of potent antioxidants consist on the presence of catechol hydroxyl groups (OH groups attached to a benzene ring) as well as planar phenylopropanoic moieties stabilized by resonance (mainly in radical and radical cation forms). Moreover, they can be reinforced by the presence of additional electron donating functional groups such as hydroxyl and methoxyl groups. All of these features are indeed present in all the experimental structures - the eight plausible conformers- highlighting a deluge of possibilities for the caffeic acid scaffold to act as a pharmacophore.

6.3. Conclusion

In summary, we have transferred the caffeic acid scaffold into the gas phase and probed it in isolation conditions by laser ablation chirp pulsed Fourier transform microwave spectroscopy (LA-CP-FTMW). We have undoubtedly deciphered the complete conformational landscape of this versatile pharmacophore, which consist of a total of eight distinct conformers. A unique set of rotational parameters have been provided for each of them. Two different skeletal frames (*syn*- and *anti*- forms) can be differentiated for caffeic acid based on a torsion of the pendant ring, which produces a distinctive change in the moments of inertia. Moreover, all the feasible spatial arrangements have been unleashed thorough an inquiry of the trend of the rotational constants supported by high-level theoretical computations, showing a broad intrinsic conformational space.

We have observed that all the observed conformers are practically planar, which is reflected in the values of the inertial defect. The three-dimensional structural information provided in this work should be of great interest to comprehend the physical-chemical properties shown by this archetypal hydroxycinnamic acid and shall ultimately shed light on the mechanisms underlying its biological and pharmacological activity.

Additionally, our investigation may perhaps help as a preliminar step on the design of new caffeic acid-based pharmacophores. We are currently pushing the limits of rotational spectroscopy, highlighting its potential as an outstanding characterization technique for the investigation of very similar structures exhibiting analogous rotational constants. Within this framework, we plan to extend our research to unveil the shape of more natural products that have remained, until now, elusive for high-resolution rotational studies.

6.4. References

1. Kumar, N.; Goel, N. Phenolic acids: Natural versatile molecules with promising therapeutic applications. *Biotechnol. Reports* **2019**, *24*, e00370,
2. Touaibia, M.; Jean-Francois, J.; Doiron, J. Caffeic Acid, A Versatile Pharmacophore: An Overview. *Mini-Reviews Med. Chem.* **2012**, *11*, 695–713.
3. Gross, G.G. *Biosynthesis and Metabolism of Phenolic Acids and Monolignols*; ACADEMIC PRESS, INC., 1985.
4. Clé, C.; Hill, L.M.; Niggeweg, R.; Martin, C.R.; Guisez, Y.; Prinsen, E.; Jansen, M.A.K. Modulation of chlorogenic acid biosynthesis in Solanum lycopersicum; consequences for phenolic accumulation and UV-tolerance. *Phytochemistry* **2008**, *69*, 2149–2156.
5. Ravn, H.; Andary, C.; Kovács, G.; Mølgaard, P. Caffeic acid esters as in vitro inhibitors of plant pathogenic bacteria and fungi. *Biochem. Syst. Ecol.* **1989**, *17*, 175–184.
6. Ávila-Román, J.; Soliz-Rueda, J.R.; Bravo, F.I.; Aragonès, G.; Suárez, M.; Arola-Arnal, A.; Mulero, M.; Salvador, M.J.; Arola, L.; Torres-Fuentes, C.; et al. Phenolic compounds and biological rhythms: Who takes the lead? *Trends Food Sci. Technol.* **2021**, *113*, 77–85.
7. Boudet, A.M. Evolution and current status of research in phenolic compounds. *Phytochemistry* **2007**, *68*, 2722–2735.
8. Dixon, R.A. Natural products and plant disease resistance. *Nature* **2001**, *411*, 1–5.
9. Clifford, M.N. Chlorogenic acids and other cinnamates - Nature, occurrence and dietary burden. *J. Sci. Food Agric.* **1999**, *79*, 362–372.
10. Li, L.; Shewry, P.R.; Ward, J.L. Phenolic acids in wheat varieties in the healthgrain diversity screen. *J. Agric. Food Chem.* **2008**, *56*, 9732–9739.
11. Nyström, L.; Mäkinen, M.; Lampi, A.M.; Piironen, V. Antioxidant activity of steryl ferulate extracts from rye and wheat bran. *J. Agric. Food Chem.* **2005**, *53*, 2503–2510.
12. Vernon, L.S.; Zaya, J.; Trousdale, E.K. Caftaric and Coutaric Acids in Fruit of *Vitis*. *Phytochemistry* **1986**, *25*, 2127–2133.
13. Clifford, M.N. Chlorogenic acids and other cinnamates - nature, occurrence, dietary burden, absorption and metabolism. *J. Sci. Food Agric.* **2000**, *80*, 1033–1043.
14. Michaluart, P.; Masferrer, J.L.; Carothers, A.M.; Subbaramaiah, K.; Zweifel, B.S.; Koboldt, C.; Mestre, J.R.; Grunberger, D.; Sacks, P.G.; Tanabe, T.; et al. Inhibitory effects of caffeic acid phenethyl ester on the activity and expression of cyclooxygenase-2 in human oral epithelial cells and in a rat model of inflammation. *Cancer Res.* **1999**, *59*, 2347–2352.
15. Huang, W.Y.; Cai, Y.Z.; Zhang, Y. Natural phenolic compounds from medicinal herbs and dietary plants: Potential use for cancer prevention. *Nutr. Cancer* **2010**, *62*, 1–20.
16. Slavin, J.L. Mechanisms for the Impact of Whole Grain Foods on Cancer Risk. *J. Am. Coll. Nutr.* **2000**, *19*, 300S–307S.

17. Mirzaei, S.; Gholami, M.H.; Zabolian, A.; Saleki, H.; Farahani, M.V.; Hamzehlou, S.; Far, F.B.; Sharifzadeh, S.O.; Samarghandian, S.; Khan, H.; et al. Caffeic acid and its derivatives as potential modulators of oncogenic molecular pathways: New hope in the fight against cancer. *Pharmacol. Res.* **2021**, *171*, 105759.
18. Chao, P.C.; Hsu, C.C.; Yin, M.C. Anti-inflammatory and anti-coagulatory activities of caffeic acid and ellagic acid in cardiac tissue of diabetic mice. *Nutr. Metab.* **2009**, *6*, 1–8.
19. Kırkızbekmez, H.; İnan, Y.; Reis, R.; Sipahi, H.; Gören, A.C.; Yeşilada, E. Phenolic compounds from the aerial parts of Clematis viticella L. and their in vitro anti-inflammatory activities*. *Nat. Prod. Res.* **2019**, *33*, 2541–2544.
20. Paciello, F.; Di Pino, A.; Rolesi, R.; Troiani, D.; Paludetti, G.; Grassi, C.; Fetoni, A.R. Anti-oxidant and anti-inflammatory effects of caffeic acid: in vivo evidences in a model of noise-induced hearing loss. *Food Chem. Toxicol.* **2020**, *143*, 111555.
21. Gülcin, I. Antioxidant activity of caffeic acid (3,4-dihydroxycinnamic acid). *Toxicology* **2006**, *217*, 213–220.
22. Agunloye, O.M.; Oboh, G.; Ademiluyi, A.O.; Ademosun, A.O.; Akindahunsi, A.A.; Oyagbemi, A.A.; Omobowale, T.O.; Ajibade, T.O.; Adedapo, A.A. Cardio-protective and antioxidant properties of caffeic acid and chlorogenic acid: Mechanistic role of angiotensin converting enzyme, cholinesterase and arginase activities in cyclosporine induced hypertensive rats. *Biomed. Pharmacother.* **2019**, *109*, 450–458.
23. Spiegel, M.; Gamian, A.; Sroka, Z. A statistically supported antioxidant activity DFT benchmark—the effects of hartree–fock exchange and basis set selection on accuracy and resources uptake. *Molecules* **2021**, *26*.
24. Veeren, B.; Bringart, M.; Turpin, C.; Rondeau, P.; Planesse, C.; Ait-Arsa, I.; Gimé, F.; Marodon, C.; Meilhac, O.; Gonthier, M.P.; et al. Caffeic acid, one of the Major Phenolic Acids of the Medicinal Plant Antirhea borbonica, Reduces Renal Tubulointerstitial Fibrosis. *Biomedicines* **2021**, *9*.
25. Morales, J.C.; Lucas, R. *Structure-Activity Relationship of Phenolic Antioxidants and Olive Components*; Elsevier Inc., 2010.
26. Bakalbassis, E.G.; Nenadis, N.; Tsimidou, M. A density functional theory study of structure-activity relationships in caffeic and dihydrocaffeic acids and related monophenols. *JAOCs, J. Am. Oil Chem. Soc.* **2003**, *80*, 459–466.
27. VanBesien, E.; Marques, M.P.M. Ab initio conformational study of caffeic acid. *J. Mol. Struct. Theochem* **2003**, *625*, 265–275.
28. Garcia-granda, S.; Beurskens, G.; Beurskens, P.T. Structure of 3 , 4-Dihydroxy-trans-cinnamic Acid (Caffeic Acid) and its Lack of Solid-State. *Acta Cryst* **1987**, *43*, 683–685.
29. Świsłocka, R. Spectroscopic (FT-IR, FT-Raman, UV absorption, ^1H and ^{13}C NMR) and theoretical (in B3LYP/6-311++G** level) studies on alkali metal salts of caffeic acid. *Spectrochim. Acta - Part A Mol. Biomol. Spectrosc.* **2013**, *100*, 21–30.
30. Chen, T.; Huang, Y.; Tang, Z.; Liang, D.; Yin, X. Terahertz spectral vibrational properties and weak interactions analysis of caffeic acid and ferulic acid. *J. Mol.*

- Struct.* **2022**, *1270*, 133960 and references therein.
31. Peña, I.; Daly, A.M.; Cabezas, C.; Mata, S.; Bermúdez, C.; Niño, A.; López, J.C.; Grabow, J.U.; Alonso, J.L. Disentangling the puzzle of hydrogen bonding in vitamin C. *J. Phys. Chem. Lett.* **2013**, *4*, 65–69.
 32. Cortijo, V.; Alonso, E.R.; Mata, S.; Alonso, J.L. Conformational Map of Phenolic Acids. *J. Phys. Chem. A* **2018**, *122*, 646–651.
 33. Kolesniková, L.; León, I.; Alonso, E.R.; Mata, S.; Alonso, J.L. An Innovative Approach for the Generation of Species of the Interstellar Medium. *Angew. Chemie* **2021**, *133*, 24666–24671.5.
 34. Oka, T. On negative inertial defect. *J. Mol. Struct.* **1995**, *352–353*, 225–233.
 35. Alonso, J.L.; Villamañan, M.R. Rotational Isomerism in Monofluorobenzaldehydes. *J. Chem. Soc.* **1989**, *85*, 137–149.
 36. Villamañan, R.M.; López, J.C.; Alonso, J.L. On the Planarity of 2-Fluorostyrene. *Am. Chem. Soc.* **1989**.
 37. Sanz-Novo, M.; Alonso, E.R.; León, I.; Alonso, J.L. The Shape of the Archetypical Oxocarbon Squaric Acid and Its Water Clusters. *Chem. - A Eur. J.* **2019**, *25*, 10748–10755.

7. Conclusions and Future Perspectives

All the work collected in this Memory have been carried out during the Ph.D. period. In general terms, structural studies of sweet molecules with different functionalities, Perillartine (Chapter 3), D-allose (Chapter 4) and Dulcin (Chapter 5), have been addressed in the gas phase by rotational spectroscopy with the aim of shedding light into the sweetness-structure relationship, supporting the old sweetness theories postulated by Shallenberger, Acree and Kier. Furthermore, the structural study of caffeic acid (Chapter 6), a hydroxycinnamic acid with important pharmacological profile and used as an additive, is also presented.

The following conclusions have been extracted from the experimental work presented in this Memory:

- **In Chapter 3**, after investigating the molecular geometry of perillartine by means of rotational spectroscopy, the predicted four most stable structures have been characterized. All of them present a *trans* configuration of the C=N group with respect to the double bond in the ring. Among them, one of the structures have the allyl group in an *axial* position, while three structures are in an *equatorial* disposition differing in the orientation of the allyl group. Attending the sweetness-structure relationship, all the conformers seem to be in accordance with having a three-point contact as proposed by the sweetness theory. In general, our work provides additional support to Shallenberger-Acree-Kier's theory that links the chemical structure of conformers and sweetness.

- **In Chapter 4**, the conformational preferences of the β -D-allose carbohydrate and the effect of the C₃ epimerization have been unveiled. Three conformers have been characterized showing a cooperative network of hydrogen bonds (O₄H (eq) - O₃H (ax) - O₂H (eq) - O₁H (eq)) in a counterclockwise (cc) arrangement, only differing in the orientation of the hydroxymethyl group. A comparison of the results of β -D-allose and β -D-glucose have been carried out, concluding that the main conformers and their abundance is very similar. This results could explain the similar sweetness of both molecules.

- **In Chapter 5**, the conformational panorama of dulcin has been explored. Among the four most stable conformers, it was possible to unequivocally characterize two of them. However, of the remaining two, one is “missing” due to conformational interconversion in a relaxation process, while the other conformer probably falls below the sensitivity due to its low abundance and low dipole moments. In order to rationalize the sweetness-structure relationship for this molecule, the sweetness triangle is proposed for the two conformers using the theory of sweetness proposed of Shallenberger Acree-Kier. A good match between the glucophore pattern (AH/B/ γ points) proposed in the sweetness theory, with the observed structure in the detected conformers and their distances, is revealed in this work. This knowledge in the polyurea families could serve to validate the sweetness theory and help in the design of new artificial sweeteners.

- In Chapter 6, the conformational panorama of caffeic acid has been experimentally unraveled. A total of eight structures have been caught within the supersonic expansion. In terms of the structure, two different skeletal frames (syn- and anti- forms) can be differentiated for caffeic acid, altogether with a planar structure. The presented three-dimensional structural information provide support to comprehend the physical-chemical properties and the mechanisms underlying its biological and pharmacological activity. Furthermore, the results can be useful in future investigations on the design of new caffeic acid-based pharmacophores.

With the information above, a general conclusion can be extracted. According to the results of the three sweet molecules studied in this Thesis, all the molecules present the three required contact points, i.e. the glucophore, proposed by Shallenberger, Acree and Kier in their sweetness theory. This information could be useful for food chemistry in order to help in the design and synthetization of a large variety of custom-made sweeteners. The results obtained for cafeic acid could be helpful for designing new additives employed both in food and drugs.

Future Perspective

Among all the flavors of the taste sense, sweetness provides sensations that make it one of the most desired ones for mankind. The natural occurring molecules responsible for it are ubiquitous in the food industry, and are strongly related to adverse health conditions caused, to a large extend, due to an excess consumption.

To avoid the caloric intake that involves the consumption of carbohydrates, different artificial sweeteners have been introduced in our diet. The problems don't finish here. Although artificial sweeteners may help with diabetes and weight control, it is noteworthy that in the last years its use has been intensely scrutinized. The side effects of its inclusion in our eating habits have begun to manifest, including cancer.

In this thesis, in continuation with previous works, have been carried out a intensively structural study of the sweetness pattern responsible for the sweet taste produced by both natural, with monosaccharide β -D-allose, and artificial sweeteners, with perillartine and dulcin, according to the old theories of sweetness. Note that, despite dulcin was removed from the market due to health concerns, it is a very sweet molecule and the results can be used to elaborate new sweeteners.

The results obtained in this thesis, that shed light into the atomic structural disposition that a molecule needs to be sweet, could pave the way for different future studies on this matter. Knowing the structural pattern responsible for the sweet taste may have an important implication in the design of new artificial sweeteners with improved properties, in order to obtain a better sweet taste performance, which could lead to a decrease in the amount used for food manufacturing. Nevertheless, it could be even more significant being able to design an artificial sweetener free from any health

contraindication in the future, as we learn the impact it is having on our health the now used artificial sweeteners in the industry. This is why the use of rotational spectroscopy to continue to structurally study these family of artificial sweeteners, in addition to other new synthesized ones that may arise from the information extracted from this thesis, is an unique tool that will provide valuable data for the food industry.

In the following years, we plan to extend our knowledge on sweetness based on several topics:

- The sweetness theory proposed by Shallerberger-Acree-Kier is based on the main three contact points. These points are the minimum contact points that a molecules must have in order to interact with a receptor. On the other hand, nowadays new and more complex theories have emerged. Some of these theories introduce new contact points. We will study new sweeteners and explore some of these theories. This will allow gaining new knowledge about sweetness.
- The whole docking between the ligand (sweetener in this case) and receptor, not only relies in their interactions, but also in the interactions with the environment. In fact, biological processes are a result of minimizing the Gibbs free energies as a whole. Therefore, we plan on studying the interactions between sweeteners and water.
- Finally, in order to mimic the interactions between the sweetener and the protein, we will use a reductionist approach and study the interactions between different sweeteners and the main amino acids that are responsible of the docking procedure.

Conclusiones y

Perspectivas Futuras

Esta tesis doctoral reúne cuatro estudios recopilados en cuatro capítulos. Los capítulos 3, 4, y 5 abordan la caracterización estructural por espectroscopía de rotación de tres moléculas percibidas como dulces: perillartina, alosa y dulcina. El capítulo 6 recoge un estudio del ácido cafeico que, además de un aditivo, es un compuesto orgánico con excelentes propiedades farmacológicas. Estos estudios nos han permitido obtener las siguientes conclusiones que se detallan a continuación:

- **Capítulo 3:** En el estudio de la perillartina se pudieron identificar de manera inequívoca cuatro especies, las cuales presentan una disposición *E* del grupo C=N con respecto al doble enlace en el anillo. Una de las estructuras contiene el grupo alilo en posición axial, mientras que las tres muestran diferentes orientaciones del grupo alilo en configuración ecuatorial. Todos estos confórmeros parecen contener los tres puntos de anclaje que propone la teoría del dulzor. La caracterización estructural que nos brinda este estudio sugiere que la entidad dadora se encuentra localizada en el carbono opuesto al doble enlace conjugado, mientras que el punto *B* se sitúa en el oxígeno. Asimismo, el amplio abanico conformacional de este edulcorante y la doble posibilidad de recepción con el punto *AH* podría explicar su intenso sabor dulce. Este trabajo ofrece un apoyo adicional para verificar la teoría de Shallenberger-Acree-Kier, la cual vincula el sabor dulce con la estructura molecular.
- **Capítulo 4:** En la investigación de la β -D-alosa se pudieron localizar tres confórmeros, los cuales muestran una red cooperativa de enlace de hidrógeno O_4H (eq) $\rightarrow O_3H$ (ax) $\rightarrow O_2H$ (eq) $\rightarrow O_1H$ (eq) y en una disposición en sentido antihorario (cc). Las tres especies solo difieren en la orientación del grupo hidroximetilo. Estos resultados fueron comparados con la β -D-glucosa, dado que la alosa es el epímero C₃. Por un lado, se observa que las dos moléculas presentan confórmeros con estructuras similares y con las mismas abundancias relativas en su población. Esta semejanza estructural podría explicar que las dos sean moléculas que se perciben como dulces, contiendo el patrón glucóforo AH/B/ γ .
- **Capítulo 5:** Con respecto a la investigación de la dulcina, se pudieron identificar inequívocamente dos estructuras de las cuatro estables. No obstante, una de las especies más estables energéticamente, no se pudo localizar debido al fenómeno de interconversión conformacional. La cuarta estructura no se pudo detectar dada la baja abundancia y sus bajos momentos dipolares. En cuanto a las dos estructuras más estables, ambas presentan una interacción intramolecular entre el grupo NH₂ y la nube electrónica π del grupo del anillo fenilo. El segundo confórmero detectado presenta una disposición similar, pero con el grupo alcoxi fuera del plano con respecto al grupo fenilo. Se proponen dos triángulos de dulzor para los confórmeros de dulcina, donde ambos triángulos cumplen las características de la teoría del dulzor propuesta por Shallenberger-Acree-Kier.

• **Capítulo 6:** En la investigación del ácido cafeico se pudo descifrar el panorama conformacional completo, el cual está conformado por ocho especies isoméricas. Estos confórmeros se pueden clasificar en dos familias: *syn* y *anti*, dependiendo de la torsión de grupo fenilo, el cual produce un cambio significativo en los momentos de inercia. Asimismo, hemos observado que todas las estructuras son planas, lo cual se ha materializado con los valores de los momentos de inercia. La información estructural tridimensional presentada brinda apoyo para comprender las propiedades físico-químicas y los mecanismos que subyacen a su actividad biológica y farmacológica. Además, los resultados pueden ser útiles en futuras investigaciones sobre el diseño de nuevos farmacóforos basados en ácido cafeico.

Por tanto, en relación a las conclusiones de cada capítulo se puede decir que los puntos propuestos por Shallenberger- Acree y Kier, de las moléculas percibidas como dulces, se han podido verificar gracias a la caracterización estructural en 3D. Esta información es muy valiosa, dado que, permitiría diseñar y sintetizar un amplio abanico de edulcorantes, lo que resulta muy atractivo para la industria farmacéutica y alimentaria. Por otra parte, los datos obtenidos del ácido cafeico nos ayudarían a comprender cómo actúa esta molécula en los seres humanos, lo cual sería clave para el diseño de nuevos fármacos.

Perspectivas futuras

El consumo excesivo de alimentos dulces ha provocado que un número significativo de personas sufra obesidad, hipertensión, diabetes, entre otras enfermedades. Como consecuencia, un mercado de edulcorantes no calóricos ha surgido para intentar responder a las necesidades millones de personas. No obstante, la investigación y desarrollo de nuevos edulcorantes es una tarea compleja que requiere de conocimientos sólidos sobre el mecanismo de quimiorrecepción del sabor dulce.

Una teoría que correlaciona el dulzor de las moléculas con su estructura es la postulada por Shallenberger, Acree y Kier. Desafortunadamente, la disposición sápida que proponían en los compuestos dulces no se había podido comprobar pese a las numerosas investigaciones realizadas. Tales estudios para comprender la interacción de la molécula objetivo con el receptor, fueron llevados a cabo en fase condensada. Por consiguiente, la geometría de las “moléculas dulces” se encuentra distorsionada con el medio que la rodea, no pudiendo obtener las distancias concretas de la tripartita glucófora.

Esta tesis doctoral abordó el estudio estructural en 3D de tres moléculas percibidas como dulces: perillartina, alosa y dulcina, con el fin de verificar el patrón glucóforo. Los resultados que se obtuvieron en estas investigaciones, verificaron la teoría del dulzor. Esta nueva información obtenida podría emplearse para el diseño de nuevos edulcorantes artificiales con mejores propiedades: mayor intensidad de dulzor, propiedades beneficiosas para el ser humano o que aporten un menor contenido energético.

Durante los siguientes años, se extenderá la información obtenida sobre los edulcorantes, mediante los siguientes estudios:

- La teoría del dulzor propuesta por Shallerberger-Acree-Kier se basa en tres puntos de contacto principales. Estos puntos de contactos son los mínimos necesarios para que una molécula dulce interactúe con el receptor. No obstante, hoy en día existen teorías más complejas que introducen nuevos puntos de contacto. Por lo tanto, además de estudiar nuevos edulcorantes, se contrastarán los resultados con algunas de estas teorías. Esto nos permitirá extender nuestro conocimiento actual sobre los edulcorantes.
- El proceso de *docking* molecular entre un ligando (en este caso un edulcorante) y un receptor, no solo necesita de las interacciones intermoleculares entre ambos, sino que también con el entorno. De hecho, los procesos biológicos son un resultado de la minimización de la energía libre de Gibbs en su conjunto. Por ello, es lógico extender nuestros estudios a los complejos formados entre moléculas dulces y agua.
- Por último, con objeto de modelar las interacciones entre los edulcorantes y las proteínas de los receptores, se pretende emplear un modelo reduccionista estudiando las interacciones entre distintas moléculas dulces y los aminoácidos claves en la unión ligando-proteína.

Annex

Annex I

Table AI-1. Measured frequencies and residuals (in MHz) for the transitions of rotamer I of perillartine (in MHz).

<i>J'</i>	<i>K'_{-1}</i>	<i>K'_{+1}</i>	<i>J''</i>	<i>K''_{-1}</i>	<i>K''_{+1}</i>	v_{obs}	v_{obs - v_{cal}}
4	0	4	3	0	3	2943.525	0.019
5	1	5	4	1	4	3646.145	-0.004
5	0	5	4	0	4	3678.973	-0.006
5	1	4	4	1	3	3713.514	0.022
6	1	6	5	1	5	4375.226	-0.008
6	0	6	5	0	5	4414.146	-0.037
6	3	3	5	3	2	4416.320	-0.048
6	1	5	5	1	4	4456.089	0.049
7	1	7	6	1	6	5104.256	0.018
7	0	7	6	0	6	5149.059	-0.006
7	2	6	6	2	5	5151.683	0.023
7	2	5	6	2	4	5154.663	-0.010
7	1	6	6	1	5	5198.561	0.057
8	1	8	7	1	7	5833.192	0.038
8	0	8	7	0	7	5883.568	-0.004
8	2	7	7	2	6	5887.386	-0.045
8	2	6	7	2	5	5891.953	0.004
8	1	7	7	1	6	5940.871	0.000
9	1	9	8	1	8	6561.983	0.017
9	0	9	8	0	8	6617.625	-0.029
9	2	8	8	2	7	6623.117	-0.014
9	2	7	8	2	6	6629.548	-0.031
9	1	8	8	1	7	6683.123	-0.001
10	1	10	9	1	9	7290.697	0.032
10	0	10	9	0	9	7351.251	-0.008
10	2	9	9	2	8	7358.735	-0.016
10	1	9	9	1	8	7425.254	0.005

Table AI-2. Measured frequencies and residuals (in MHz) for the transitions of rotamer II of perillartine (in MHz).

<i>J'</i>	<i>K'</i>₋₁	<i>K'</i>₊₁	<i>J''</i>	<i>K''</i>₋₁	<i>K''</i>₊₁	v_{obs}	v_{obs} - v_{cal}
4	0	4	3	0	3	2920.931	0.036
5	1	5	4	1	4	3583.791	-0.014
5	0	5	4	0	4	3649.433	0.003
5	1	4	4	1	3	3722.105	0.014
2	1	2	1	0	1	3966.178	0.007
6	1	6	5	1	5	4299.960	-0.003
6	0	6	5	0	5	4376.815	-0.033
6	2	4	5	2	3	4391.526	-0.053
3	1	3	2	0	2	4655.549	0.000
7	1	7	6	1	6	5015.805	0.001
7	0	7	6	0	6	5102.907	-0.028
7	2	6	6	2	5	5113.751	-0.004
7	2	5	6	2	4	5126.338	0.010
7	1	6	6	1	5	5209.311	0.017
4	1	4	3	0	3	5331.472	0.006
8	1	8	7	1	7	5731.280	-0.001
8	0	8	7	0	7	5827.494	0.008
8	2	7	7	2	6	5843.498	-0.043
8	2	6	7	2	5	5862.347	-0.001
8	1	7	7	1	6	5952.314	0.024
5	1	5	4	0	4	5994.362	-0.014
9	1	9	8	1	8	6446.368	0.013
9	0	9	8	0	8	6550.346	0.029
9	2	8	8	2	7	6573.023	-0.002
9	3	7	8	3	6	6580.599	0.018
9	3	6	8	3	5	6581.110	-0.001
9	1	8	8	1	7	6694.795	0.010
10	1	10	9	1	9	7160.998	0.009
10	0	10	9	0	9	7271.299	0.033
10	2	8	9	2	7	7338.716	-0.053
10	1	9	9	1	8	7436.706	0.004

Table AI-3. Measured frequencies and residuals (in MHz) for the transitions of rotamer III of perillartine (in MHz).

J'	K'_{-1}	K'_{+1}	J''	K''_{-1}	K''_{+1}	ν_{obs}	$\nu_{\text{obs}} - \nu_{\text{cal}}$
3	1	3	2	1	2	2839.691	-0.056
4	0	4	3	0	3	3821.708	0.032
5	0	5	4	0	4	4775.607	0.000
5	1	4	4	1	3	4825.170	0.013
6	1	6	5	1	5	5678.206	0.021
6	0	6	5	0	5	5728.539	-0.018
6	2	5	5	2	4	5734.581	-0.019
7	1	7	6	1	6	6623.841	0.006
7	0	7	6	0	6	6680.353	0.010
7	2	6	6	2	5	6689.888	0.024
7	2	5	6	2	4	6700.932	0.001
7	1	6	6	1	5	6753.772	0.010
8	1	8	7	1	7	7569.163	-0.010
8	1	7	7	1	6	7717.491	-0.026

Table AI-4. Measured frequencies and residuals (in MHz) for the transitions of rotamer IV of perillartine (in MHz).

J'	K'_{-1}	K'_{+1}	J''	K''_{-1}	K''_{+1}	ν_{obs}	$\nu_{\text{obs}} - \nu_{\text{cal}}$
4	0	4	3	0	3	2936.217	-0.017
5	1	5	4	1	4	3590.951	-0.008
5	0	5	4	0	4	3667.831	-0.004
5	1	4	4	1	3	3754.997	0.035
6	1	6	5	1	5	4308.292	0.014
6	0	6	5	0	5	4397.759	-0.052
6	1	5	5	1	4	4505.066	0.047
7	1	7	6	1	6	5025.151	0.012
7	1	6	6	1	5	5254.529	-0.017
8	1	8	7	1	7	5741.488	0.006
8	0	8	7	0	7	5851.713	0.010
8	1	7	7	1	6	6003.428	-0.012
9	1	9	8	1	8	6457.264	0.012

Additional Information: B3LYP vs MP2

The main difference between the four main conformers is that structures *e*-*E*-I, *e*-II, and *a*-*E*-III have the allyl group in an equatorial position, while structure *a*-*E*-I has the allyl group in an axial position. It is worth noting that calculations using the MP2 level also predicts the same four structures as the most stable structures, but with structure *a*-*E*-I which is the third most stable structure with B3LYP, as the global minimum (see Table S9). This fact is interesting as it let us to benchmark current methodologies. As described in the main manuscript, using selected transitions of the experimental results we can estimate the relative populations of the conformers, and set structure 1 as the global minimum, with structure 3 being slightly less populated. Therefore, B3LYP-GD3 gives a better description of the energetics. Finally, we would also like to highlight the importance of adding Grimme Dispersions with Becke-Johnson damping as the calculations without including them estimate structure *a*-*E*-I being too high in energy, at 560 cm⁻¹, which would result in a low population of this conformer to allow its detection. The conformational panorama of this molecule is another illustrative case of the robustness of rotational spectroscopy, not only for a definitive structural characterization, but also to contrast, benchmark, and validate the results provided by high-level computational chemistry.

Table AI-5. Theoretical spectroscopic parameters for low-energy conformers of perillartine computed at the MP2/6-311++G(d,p) level of theory.

Parameters	<i>a</i> - <i>E</i> -I	<i>e</i> - <i>E</i> -I	<i>e</i> - <i>E</i> -II	<i>e</i> - <i>E</i> -III	<i>a</i> - <i>E</i> -II	<i>a</i> - <i>E</i> -III
<i>A</i> ^[a]	1750	2878	2908	2794	1852	1636
<i>B</i>	497	376	380	383	490	508
<i>C</i>	476	362	352	354	475	497
$ \mu_a $ ^[b]	1.1	0.8	0.9	0.9	0.7	1.1
$ \mu_b $	0.1	0.1	0.2	0.3	0.4	0.4
$ \mu_c $	0.6	0.4	0.2	0.1	0.0	0.3
ΔE ^[c]	0	99	270	359	538	713
ΔE_{ZPE} ^[d]	0	40	208	295	583	790
ΔG ^[e]	37	0	135	223	676	859

[a] *A*, *B*, and *C* represent the rotational constants (in MHz). [b] $|\mu_a|$, $|\mu_b|$ and $|\mu_c|$ are the absolute values of the electric dipole moment components (in D). [c] Relative energies (in cm⁻¹) concerning the global minimum. [d] Relative energies (in cm⁻¹) with respect to the global minimum, taking into account the zero-point energy (ZPE). [e] Gibbs energies (in cm⁻¹)

Table AI-5. Theoretical spectroscopic parameters for low-energy conformers of perillartine computed at the MP2/6-311++G(d,p) level of theory.

Parameters	<i>a</i> -Z-I	<i>e</i> -Z-I	<i>e</i> -Z-II	<i>e</i> -Z-III	<i>e</i> -E-IV	<i>e</i> -E-V
<i>A</i> ^[a]	1809	2806	2743	2768	2870	2900
<i>B</i>	491	375	384	378	376	380
<i>C</i>	478	361	352	357	362	352
$ \mu_a ^{[b]}$	1.2	0.8	0.8	0.8	1.7	1.8
$ \mu_b $	0.4	0.2	0.2	0.4	2.7	2.9
$ \mu_c $	0.1	0.2	0.2	0.2	0.7	0.7
$\Delta E^{[c]}$	1138	1307	1459	1578	1916	2089
$\Delta E_{ZPE}^{[d]}$	1114	1223	1374	1489	1751	1922
$\Delta G^{[e]}$	1102	1149	1273	1377	1718	1856

[a] *A*, *B*, and *C* represent the rotational constants (in MHz). [b] $|\mu_a|$, $|\mu_b|$ and $|\mu_c|$ are the absolute values of the electric dipole moment components (in D). [c] Relative energies (in cm $^{-1}$) concerning the global minimum. [d] Relative energies (in cm $^{-1}$) with respect to the global minimum, taking into account the zero-point energy (ZPE). [e] Gibbs energies (in cm $^{-1}$)

Annex II

Table AII-1. Fitted rotational transitions of rotamer I of β -D-allose (in MHz).

J'	K'_{-1}	K'_{+1}	J''	K''_{-1}	K''_{+1}	ν_{obs}	$\nu_{\text{obs}} - \nu_{\text{cal}}$
5	4	1	5	3	3	4030.508	-0.028
6	3	4	6	1	5	4103.292	0.003
3	2	2	2	2	1	4109.065	0.007
6	4	2	6	3	4	4225.489	-0.025
7	4	4	7	3	5	4343.884	-0.008
6	1	5	6	1	6	4353.598	-0.006
6	1	5	6	0	6	4360.495	0.016
2	2	1	1	1	0	4362.007	0.012
3	2	1	2	2	0	4382.723	0.012
3	1	2	2	1	1	4425.971	0.013
2	2	0	1	1	0	4440.417	0.012
7	3	5	7	2	6	4520.138	-0.017
6	2	5	6	0	6	4543.806	0.007
2	2	1	1	1	1	4612.941	0.010
7	5	3	7	4	3	4677.041	-0.024
2	2	0	1	1	1	4691.364	0.023
4	1	3	3	2	2	4715.589	0.001
4	0	4	3	1	3	4800.796	0.026
4	1	4	3	1	3	4857.034	0.028
6	5	2	6	4	2	4937.746	-0.029
4	0	4	3	0	3	4939.448	-0.008
6	5	1	6	4	2	4942.268	-0.031
4	1	4	3	0	3	4995.734	0.043
6	5	2	6	4	3	5048.371	-0.002
6	5	1	6	4	3	5052.866	-0.031
8	5	4	8	4	5	5076.549	0.038
7	4	4	7	2	5	5108.928	0.024
5	2	3	4	3	1	5109.931	-0.010
2	2	0	1	0	1	5148.577	0.007
5	2	3	4	3	2	5216.561	0.009
8	3	6	8	2	7	5228.461	-0.029
8	3	6	8	1	7	5257.324	-0.003
7	1	6	7	1	7	5267.800	0.000
7	1	6	7	0	7	5269.979	-0.036
7	2	6	7	0	7	5345.901	-0.003
6	4	3	6	2	4	5366.174	0.010
5	1	4	4	2	2	5397.078	-0.004
4	2	3	3	2	2	5416.278	0.012
3	1	2	2	0	2	5463.475	0.007
3	2	2	2	1	1	5480.760	0.015
4	3	2	3	3	1	5598.641	0.028
4	3	1	3	3	0	5689.003	0.017
4	1	3	3	1	2	5770.388	0.012
3	2	1	2	1	1	5832.827	0.019
4	2	2	3	2	1	5952.798	0.009
10	4	7	10	2	8	5971.665	-0.022
5	0	5	4	1	4	5979.714	0.017

J'	K'_{-1}	K'_{+1}	J''	K''_{-1}	K''_{+1}	ν_{obs}	$\nu_{\text{obs}} - \nu_{\text{cal}}$
5	1	5	4	1	4	6000.062	0.005
5	0	5	4	0	4	6035.947	0.016
5	1	5	4	0	4	6056.312	0.021
3	2	2	2	1	2	6233.568	0.015
5	1	4	4	2	3	6285.673	0.006
3	2	1	2	1	2	6585.637	0.021
5	2	4	4	2	3	6675.700	0.021
6	2	4	5	3	2	6724.957	0.000
3	2	1	2	0	2	6870.354	0.035
5	1	4	4	1	3	6986.357	0.013
3	3	1	2	2	0	6987.406	0.008
5	3	3	4	3	2	6992.765	0.015
3	3	0	2	2	0	7003.648	0.011
5	4	2	4	4	1	7021.202	0.018
5	4	1	4	4	0	7042.306	0.008
3	3	1	2	2	1	7065.820	0.012
3	3	0	2	2	1	7082.068	0.020
6	2	4	5	3	3	7099.519	-0.015
6	0	6	5	1	5	7122.240	0.011
6	1	6	5	1	5	7129.118	0.015
6	0	6	5	0	5	7142.607	0.019
6	1	6	5	0	5	7149.488	0.025
5	3	2	4	3	1	7260.730	0.014
4	2	2	3	1	2	7359.672	0.032
5	2	4	4	1	3	7376.377	0.021
5	2	3	4	2	2	7467.074	0.010
6	2	5	5	2	4	7886.989	0.008
6	1	5	5	1	4	8093.676	0.003
7	1	7	6	1	6	8251.654	0.009
4	3	1	3	2	1	8309.931	0.019
6	3	4	5	3	3	8350.805	0.023
6	4	3	5	4	2	8459.057	0.014
4	3	1	3	2	2	8661.983	0.009
6	2	4	5	2	3	8875.747	0.015
6	3	3	5	3	2	8887.724	-0.003
5	2	3	4	1	3	9056.369	0.042
7	2	6	6	2	5	9058.430	0.021
7	1	6	6	1	5	9165.851	0.011
8	0	8	7	1	7	9370.914	-0.001
8	1	8	7	1	7	9371.622	0.017
8	0	8	7	0	7	9373.143	0.013
8	1	8	7	0	7	9373.838	0.018
5	1	4	4	0	4	9445.315	-0.011
4	4	1	3	3	0	9560.605	0.009
4	4	0	3	3	0	9563.377	0.015
4	4	1	3	3	1	9576.832	-0.003
7	3	5	6	3	4	9658.593	-0.002
5	2	4	4	1	4	9779.115	0.011
12	6	7	11	7	5	10089.989	-0.017

J'	K'_{-1}	K'_{+1}	J''	K''_{-1}	K''_{+1}	ν_{obs}	$\nu_{\text{obs}} - \nu_{\text{cal}}$
6	3	4	5	2	3	10126.992	0.013
7	4	3	6	4	2	10131.968	0.032
7	2	5	6	2	4	10144.837	0.006
8	1	7	7	1	6	10249.918	0.016
9	1	9	8	1	8	10490.670	0.007
9	0	9	8	0	8	10491.149	0.006
8	3	6	7	3	5	10911.175	-0.010
6	2	4	5	1	4	10945.736	0.021
5	4	2	4	3	2	10999.416	0.010
6	3	3	5	2	3	11038.502	0.000
8	6	3	7	6	2	11266.304	-0.025
8	6	2	7	6	1	11270.753	0.002
8	2	6	7	2	5	11274.806	-0.007
8	4	5	7	4	4	11286.100	-0.017
8	5	4	7	5	3	11330.582	-0.017
9	2	8	8	2	7	11332.258	0.010
9	1	8	8	1	7	11350.753	-0.003
8	5	3	7	5	2	11407.445	-0.022
10	1	10	9	1	9	11609.514	-0.014
10	0	10	9	0	9	11609.514	-0.014
8	4	4	7	4	3	11794.063	-0.027
6	3	4	5	2	4	11806.931	-0.019
5	5	1	4	4	0	12104.159	-0.015
5	5	0	4	4	0	12104.602	0.004
5	5	1	4	4	1	12106.937	-0.002
5	5	0	4	4	1	12107.373	0.010
9	3	7	8	3	6	12113.310	-0.011
9	2	7	8	2	6	12330.150	-0.042
10	1	9	9	2	8	12451.058	0.001
10	2	9	9	2	8	12454.585	-0.014
10	1	9	9	1	8	12461.365	-0.020
10	2	9	9	1	8	12464.899	-0.029
6	4	3	5	3	3	12465.686	-0.013
9	3	7	8	2	6	12514.669	-0.035
6	4	2	5	3	3	12576.304	0.007
11	1	11	10	1	10	12728.169	-0.008
11	0	11	10	0	10	12728.169	-0.008
10	2	8	9	3	7	13199.992	0.003
10	3	8	9	3	7	13276.958	-0.021
9	3	6	8	3	5	13298.509	-0.032
10	2	8	9	2	7	13384.453	-0.049
11	2	10	10	2	9	13574.101	-0.031
11	1	10	10	1	9	13576.467	-0.031
12	1	12	11	1	11	13846.851	-0.031
12	0	12	11	0	11	13846.851	-0.031

Table AII-2. Fitted rotational transitions of rotamer II of β -D-allose (in MHz).

J'	K'_{-1}	K'_{+1}	J''	K''_{-1}	K''_{+1}	ν_{obs}	$\nu_{\text{obs}} - \nu_{\text{cal}}$
6	3	4	6	1	5	4091.775	0.033
2	2	1	1	1	0	4221.091	0.000
3	2	1	2	2	0	4288.619	0.009
6	1	5	6	1	6	4499.800	0.023
2	2	0	1	1	1	4576.204	-0.005
4	0	4	3	1	3	4598.741	0.025
7	3	5	7	2	6	4600.542	-0.024
4	1	4	3	1	3	4643.366	-0.007
4	0	4	3	0	3	4716.687	0.019
7	4	4	7	2	5	4918.621	0.003
2	2	0	1	0	1	5009.992	0.002
5	2	3	4	3	2	5186.211	-0.008
4	2	3	3	2	2	5236.907	0.013
3	2	2	2	1	1	5282.858	0.007
8	3	6	8	1	7	5372.077	0.011
7	1	6	7	0	7	5421.203	0.015
4	3	2	3	3	1	5443.141	-0.013
4	3	1	3	3	0	5554.447	0.014
4	1	3	3	1	2	5593.745	0.018
5	0	5	4	1	4	5712.174	0.027
5	0	5	4	0	4	5756.815	0.011
5	1	5	4	0	4	5771.925	0.015
4	2	2	3	2	1	5825.127	0.002
5	1	4	4	2	3	6117.877	0.011
4	2	3	3	1	2	6209.554	0.005
5	2	4	4	2	3	6438.497	0.007
3	2	1	2	1	2	6475.910	0.020
5	1	4	4	1	3	6733.698	0.010
3	3	1	2	2	0	6773.352	0.001
5	3	3	4	3	2	6792.510	0.016
6	0	6	5	1	5	6792.958	-0.003
6	1	6	5	1	5	6797.742	0.012
6	0	6	5	0	5	6808.073	0.006
6	1	6	5	0	5	6812.848	0.011
5	4	2	4	4	1	6833.212	0.022
5	4	1	4	4	0	6861.753	0.026
3	3	1	2	2	1	6863.039	-0.021
3	3	0	2	2	1	6883.354	-0.003
5	2	4	4	1	3	7054.320	0.008
5	3	2	4	3	1	7112.483	0.012
5	2	3	4	2	2	7289.002	0.012
6	1	5	5	2	4	7447.957	0.016
6	2	5	5	2	4	7587.888	0.017
6	1	5	5	1	4	7768.584	0.017
7	0	7	6	1	6	7861.024	0.016
7	1	7	6	1	6	7862.448	0.001
7	0	7	6	0	6	7865.782	0.005

J'	K'_{-1}	K'_{+1}	J''	K''_{-1}	K''_{+1}	ν_{obs}	$\nu_{\text{obs}} - \nu_{\text{cal}}$
7	1	7	6	0	6	7867.207	-0.009
6	2	5	5	1	4	7908.502	0.007
6	3	4	5	3	3	8097.840	-0.021
6	4	2	5	4	1	8349.028	-0.006
4	3	1	3	2	2	8456.278	-0.009
6	2	4	5	2	3	8627.801	0.004
7	1	6	6	2	5	8642.464	-0.027
7	2	6	6	2	5	8696.356	0.000
6	3	3	5	3	2	8713.432	0.014
7	1	6	6	1	5	8782.438	0.019
8	1	8	7	1	7	8925.056	0.000
8	0	8	7	0	7	8926.066	-0.008
4	4	0	3	3	1	9300.494	-0.009
7	3	5	6	3	4	9345.105	-0.004
5	2	4	4	1	4	9576.832	0.012
8	2	7	7	2	6	9779.115	-0.023
7	2	5	6	2	4	9807.536	0.022
8	1	7	7	1	6	9813.902	-0.018
9	1	9	8	1	8	9986.950	-0.039
9	0	9	8	0	8	9987.270	-0.019
7	3	4	6	3	3	10252.012	0.017
8	4	5	7	4	4	10964.773	-0.049
5	5	1	4	4	0	11747.047	-0.030
5	5	0	4	4	1	11751.453	-0.028
11	0	11	10	1	10	12110.448	0.014
11	1	11	10	1	10	12110.449	-0.006
11	0	11	10	0	10	12110.449	-0.006
9	6	4	8	6	3	12407.779	-0.064
9	6	3	8	6	2	12438.142	-0.036
9	5	5	8	5	4	12453.432	-0.055

Table AII-3. Fitted rotational transitions of rotamer III of β -D-allose (in MHz).

J'	K'_{-1}	K'_{+1}	J''	K''_{-1}	K''_{+1}	ν_{obs}	$\nu_{\text{obs}} - \nu_{\text{cal}}$
4	1	4	3	1	3	4545.419	-0.024
4	0	4	3	0	3	4702.383	0.044
4	2	3	3	2	2	4967.127	-0.013
4	3	2	3	3	1	5051.810	0.011
4	3	1	3	3	0	5073.861	-0.017
4	1	3	3	1	2	5303.830	0.014
5	0	5	4	0	4	5747.263	-0.008
5	2	4	4	2	3	6166.949	0.000
5	3	3	4	3	2	6324.875	-0.006
5	3	2	4	3	1	6398.732	0.019
5	1	4	4	1	3	6541.128	-0.004
5	2	3	4	2	2	6659.144	0.016
6	1	6	5	1	5	6718.127	0.002
6	0	6	5	0	5	6781.211	-0.012
6	2	5	5	2	4	7341.023	-0.004
6	3	4	5	3	3	7591.822	0.014
6	4	3	5	4	2	7602.326	-0.004
6	1	5	5	1	4	7708.113	0.002
6	3	3	5	3	2	7772.235	0.016
7	1	7	6	1	6	7785.900	-0.009
7	0	7	6	0	6	7819.113	-0.006
8	2	6	7	2	5	10634.589	-0.009
8	3	5	7	3	4	10639.478	-0.022
10	0	10	9	0	9	10962.328	0.013

Annex III

Table AIII-1. Observed frequencies for rotational transition of rotamer I of dulcin (in MHz).

<i>J'</i>	<i>K'_{-1}</i>	<i>K'_{+1}</i>	<i>J''</i>	<i>K''_{-1}</i>	<i>K''_{+1}</i>	ν_{obs}	$\nu_{\text{obs}} - \nu_{\text{cal}}$
4	0	4	3	0	3	2388.61	-0.02
5	1	5	4	1	4	2955.14	-0.01
5	0	5	4	0	4	2985.46	-0.01
6	1	6	5	1	5	3546.07	0.01
6	1	5	5	1	4	3620.40	-0.01
2	1	1	1	0	1	3966.65	0.01
7	1	7	6	1	6	4136.93	0.01
7	0	7	6	0	6	4178.49	0.01
7	1	6	6	1	5	4223.64	0.00
3	1	2	2	0	2	4582.50	0.01
8	1	8	7	1	7	4727.71	0.01
8	0	8	7	0	7	4774.58	0.00
8	2	7	7	2	6	4777.57	-0.01
8	2	6	7	2	5	4781.08	-0.02
8	1	7	7	1	6	4826.79	-0.01
4	1	3	3	0	3	5204.60	-0.02
9	1	9	8	1	8	5318.41	0.01
9	0	9	8	0	8	5370.34	0.01
9	2	8	8	2	7	5374.61	0.00
9	2	7	8	2	6	5379.61	0.00
9	1	8	8	1	7	5429.89	0.02
5	1	4	4	0	4	5833.09	0.00
10	1	10	9	1	9	5909.02	0.00
10	0	10	9	0	9	5965.72	0.00
10	2	9	9	2	8	5971.56	0.01
10	2	8	9	2	7	5978.44	0.00
10	1	9	9	1	8	6032.85	0.01
11	1	11	10	1	10	6499.53	0.00
11	0	11	10	0	10	6560.69	0.00
11	2	10	10	2	9	6568.44	0.00
11	3	8	10	3	7	6571.10	-0.07
11	3	9	10	3	8	6571.10	0.04
11	2	9	10	2	8	6577.60	0.00
11	1	10	10	1	9	6635.71	0.00
12	1	12	11	1	11	7089.93	0.00
12	0	12	11	0	11	7155.21	-0.01
12	2	11	11	2	10	7165.25	0.01
12	4	8	11	4	7	7168.04	-0.01
12	4	9	11	4	8	7168.04	-0.01
12	3	10	11	3	9	7168.73	0.09
12	3	9	11	3	8	7168.73	-0.09
12	2	10	11	2	9	7177.13	0.00
12	1	11	11	1	10	7238.44	0.00
13	1	13	12	1	12	7680.20	-0.02
13	0	13	12	0	12	7749.26	0.00
13	2	12	12	2	11	7761.96	0.00

J'	K'_{-1}	K'_{+1}	J''	K''_{-1}	K''_{+1}	ν_{obs}	$\nu_{\text{obs}} - \nu_{\text{cal}}$
13	4	10	12	4	9	7765.53	0.00
13	4	9	12	4	8	7765.53	0.01
13	3	11	12	3	10	7766.28	0.00
13	3	10	12	3	9	7766.52	0.02
13	2	11	12	2	10	7777.05	-0.01
13	1	12	12	1	11	7841.02	-0.01

Table AIII-2. Observed frequencies for rotational transition of rotamer II of dulcin (in MHz).

J'	K'_{-1}	K'_{+1}	J''	K''_{-1}	K''_{+1}	ν_{obs}	$\nu_{\text{obs}} - \nu_{\text{cal}}$
7	1	7	6	1	6	4527.41	0.00
7	1	6	6	1	5	4650.74	0.01
8	1	8	7	1	7	5173.64	-0.01
8	0	8	7	0	7	5236.97	-0.01
8	1	7	7	1	6	5314.54	0.01
10	1	10	9	1	9	6465.48	0.01
10	0	10	9	0	9	6539.64	0.00
10	2	9	9	2	8	6555.08	0.00
10	1	9	9	1	8	6641.36	-0.01
11	1	11	10	1	10	7111.02	0.00
11	2	10	10	2	9	7209.85	-0.01
11	1	10	10	1	9	7304.33	0.00
12	1	12	11	1	11	7756.31	0.00
12	0	12	11	0	11	7838.13	0.00
12	2	11	11	2	10	7864.43	0.00
12	1	11	11	1	10	7966.92	0.00

Annex IV

Table AIV-1. Observed frequencies and residuals (in MHz) for the rotational transitions of rotamer I of caffeic acid (in MHz).

<i>J'</i>	<i>K'_{-1}</i>	<i>K'_{+1}</i>	<i>J''</i>	<i>K''_{-1}</i>	<i>K''_{+1}</i>	v_{obs}	v_{obs} - v_{cal}
4	2	3	3	2	2	2414.907	-0.016
5	2	4	4	2	3	3017.883	-0.008
2	1	2	1	0	1	3108.121	-0.001
8	0	8	7	1	7	3319.684	0.004
6	1	6	5	1	5	3498.642	0.013
6	2	5	5	2	4	3620.351	-0.001
3	1	3	2	0	2	3652.310	-0.018
4	1	4	3	0	3	4177.565	-0.014
7	0	7	6	0	6	4193.245	-0.021
7	1	6	6	1	5	4358.270	-0.010
8	1	8	7	1	7	4659.631	-0.022
5	1	5	4	0	4	4685.122	0.005
8	0	8	7	0	7	4780.744	0.001
13	2	11	13	1	12	4928.498	-0.027
11	2	9	11	1	10	5028.626	-0.019
10	2	8	10	1	9	5108.413	-0.011
6	1	6	5	0	5	5176.645	-0.004
9	2	7	9	1	8	5201.407	-0.010
8	2	6	8	1	7	5302.479	-0.026
9	0	9	8	0	8	5364.045	-0.033
7	2	5	7	1	6	5406.638	-0.009
9	2	8	8	2	7	5423.661	-0.023
6	2	4	6	1	5	5509.051	0.000
9	1	8	8	1	7	5595.278	-0.021
5	2	3	5	1	4	5605.322	-0.003
7	1	7	6	0	6	5654.329	0.000
4	2	2	4	1	3	5691.579	-0.015
3	2	1	3	1	2	5764.579	0.001
2	2	0	2	1	1	5821.615	-0.017
2	2	1	2	1	2	5940.752	-0.020
3	2	2	3	1	3	6001.010	-0.015
10	2	9	9	2	8	6023.113	-0.002
4	2	3	4	1	4	6081.564	-0.021
8	1	8	7	0	7	6120.717	0.001
10	1	10	9	0	9	7031.401	0.034
2	2	1	1	1	0	7068.638	0.002
2	2	0	1	1	1	7109.173	0.011
3	2	2	2	1	1	7632.583	0.013
3	2	1	2	1	2	7755.377	0.011
4	2	3	3	1	2	8176.473	0.020
4	2	2	3	1	3	8425.095	0.015
5	2	4	4	1	3	8700.359	0.008
5	2	3	4	1	4	9120.772	0.015
6	2	5	5	1	4	9204.413	0.019
7	2	6	6	1	5	9688.804	0.008
6	2	4	5	1	5	9845.451	0.012

J'	K'_{-1}	K'_{+1}	J''	K''_{-1}	K''_{+1}	ν_{obs}	$\nu_{\text{obs}} - \nu_{\text{cal}}$
8	2	7	7	1	6	10153.888	0.024
3	3	1	2	2	0	11612.819	0.008
3	3	0	2	2	1	11613.431	0.005
4	3	2	3	2	1	12215.420	-0.004
4	3	1	3	2	2	12218.517	0.005
5	3	2	4	2	3	12824.992	0.000
6	3	4	5	2	3	13411.946	0.004
6	3	3	5	2	4	13433.713	0.000

Table AIV-2. Observed frequencies and residuals (in MHz) for the rotational transitions of rotamer II of caffeic acid (in MHz).

<i>J'</i>	<i>K'_{-1}</i>	<i>K'_{+1}</i>	<i>J''</i>	<i>K''_{-1}</i>	<i>K''_{+1}</i>	v_{obs}	v_{obs - v_{cal}}
5	0	5	4	0	4	3012.195	-0.021
7	1	7	6	1	6	4086.434	0.013
7	0	7	6	0	6	4200.362	0.010
7	1	6	6	1	5	4365.874	-0.003
8	1	8	7	1	7	4667.451	0.011
8	0	8	7	0	7	4788.789	0.001
8	2	7	7	2	6	4831.605	0.007
8	1	7	7	1	6	4986.196	0.007
9	1	9	8	1	8	5247.471	0.002
9	2	7	8	2	6	5503.807	-0.011
9	1	8	8	1	7	5605.014	-0.010
10	1	10	9	1	9	5826.421	-0.028
10	0	10	9	0	9	5953.083	0.002
10	2	9	9	2	8	6033.408	0.011
10	2	8	9	2	7	6129.094	0.009
10	1	9	9	1	8	6222.120	-0.002

Table AIV-3. Observed frequencies and residuals (in MHz) for the rotational transitions of rotamer III of caffeic acid (in MHz).

<i>J'</i>	<i>K'_{-1}</i>	<i>K'_{+1}</i>	<i>J''</i>	<i>K''_{-1}</i>	<i>K''_{+1}</i>	v_{obs}	v_{obs - v_{cal}}
5	1	5	4	1	4	2931.355	-0.009
5	0	5	4	0	4	3022.140	0.018
6	1	6	5	1	5	3516.024	-0.013
6	0	6	5	0	5	3619.870	-0.023
6	1	5	5	1	4	3756.577	-0.031
7	1	7	6	1	6	4099.929	0.041
8	1	8	7	1	7	4682.827	0.005
8	0	8	7	0	7	4804.550	0.005
8	1	7	7	1	6	5002.565	0.018
9	0	9	8	0	8	5390.749	0.001
9	1	8	8	1	7	5623.425	0.011
10	1	10	9	1	9	5845.638	-0.015
10	0	10	9	0	9	5972.679	-0.002
10	2	9	9	2	8	6053.224	-0.010

Table AIV-4. Observed frequencies and residuals (in MHz) for the rotational transitions of rotamer IV of caffeic acid (in MHz).

<i>J'</i>	<i>K'_{-1}</i>	<i>K'_{+1}</i>	<i>J''</i>	<i>K''_{-1}</i>	<i>K''_{+1}</i>	v_{obs}	v_{obs - v_{cal}}
5	1	5	4	0	4	4711.237	-0.010
6	1	6	5	0	5	5205.826	-0.021
9	2	8	8	2	7	5458.911	-0.017
2	2	0	2	1	1	5847.515	-0.011
10	1	10	9	1	9	5854.232	0.003
2	2	1	2	1	2	5967.589	-0.015
10	0	10	9	0	9	5981.419	-0.006
3	2	2	3	1	3	6028.315	-0.019
10	5	5	9	5	4	6083.089	-0.009
10	3	7	9	3	6	6094.050	0.014
4	2	3	4	1	4	6109.487	-0.046
10	1	9	9	1	8	6251.899	-0.009
2	2	1	1	1	0	7102.698	-0.001
2	2	0	1	1	1	7143.541	-0.006
3	2	2	2	1	1	7670.259	0.013
3	2	1	2	1	2	7794.023	0.001
4	2	3	3	1	2	8217.607	0.021
4	2	2	3	1	3	8468.209	0.002
5	2	4	4	1	3	8744.797	0.015
5	2	3	4	1	4	9168.572	-0.008
6	2	4	5	1	5	9898.238	0.023
7	2	5	6	1	6	10660.714	0.000
3	3	1	2	2	0	11668.531	0.000
4	3	2	3	2	1	12275.072	0.012
4	3	1	3	2	2	12278.185	0.002
5	3	3	4	2	2	12879.212	-0.008
5	3	2	4	2	3	12888.638	0.016

Table AIV-5. Observed frequencies and residuals (in MHz) for the rotational transitions of rotamer V of caffeic acid (in MHz).

<i>J'</i>	<i>K'</i>₋₁	<i>K'</i>₊₁	<i>J''</i>	<i>K''</i>₋₁	<i>K''</i>₊₁	v_{obs}	v_{obs} - v_{cal}
4	1	4	3	1	3	2271.550	0.035
4	0	4	3	0	3	2336.888	0.029
4	1	3	3	1	2	2408.660	-0.005
5	1	5	4	1	4	2838.663	0.008
6	0	6	5	0	5	3497.260	0.002
6	1	5	5	1	4	3610.897	-0.007
7	0	7	6	0	6	4074.112	-0.001
7	2	5	6	2	4	4115.885	-0.001
8	1	8	7	1	7	4536.898	-0.014
8	0	8	7	0	7	4648.296	0.000
8	1	7	7	1	6	4810.503	0.005
9	0	9	8	0	8	5219.552	0.004
9	1	8	8	1	7	5408.956	-0.006
10	1	10	9	1	9	5665.749	-0.014

Table AIV-6. Observed frequencies and residuals (in MHz) for the rotational transitions of rotamer VI of caffeic acid (in MHz).

<i>J'</i>	<i>K'_{-1}</i>	<i>K'_{+1}</i>	<i>J''</i>	<i>K''_{-1}</i>	<i>K''_{+1}</i>	v_{obs}	v_{obs} - v_{cal}
5	1	4	4	1	3	3012.649	-0.010
2	1	2	1	0	1	3301.486	-0.003
7	0	7	6	0	6	4077.656	0.000
7	1	6	6	1	5	4214.761	0.017
4	1	4	3	0	3	4353.796	-0.029
8	1	8	7	1	7	4540.888	0.000
8	0	8	7	0	7	4652.326	-0.009
8	2	7	7	2	6	4680.928	-0.003
8	2	6	7	2	5	4714.462	-0.005
5	1	5	4	0	4	4856.054	-0.021
9	1	9	8	1	8	5106.180	0.003
9	0	9	8	0	8	5224.071	-0.009
6	1	6	5	0	5	5343.785	-0.002
10	1	10	9	1	9	5670.721	-0.006
7	1	7	6	0	6	5818.437	0.041
8	1	8	7	0	7	6281.615	-0.014
3	2	2	3	1	3	6647.676	-0.002
4	2	3	4	1	4	6716.768	-0.027
5	2	4	5	1	5	6803.415	-0.010
7	2	6	7	1	7	7029.784	-0.006
2	2	1	1	1	0	7698.804	0.013
2	2	0	1	1	1	7733.516	0.005
3	2	2	2	1	1	8250.220	0.010
3	2	1	2	1	2	8355.193	0.012
4	2	3	3	1	2	8784.421	0.010
4	2	2	3	1	3	8996.366	-0.004
5	2	4	4	1	3	9301.431	-0.002
5	2	3	4	1	4	9658.723	0.006
6	2	5	5	1	4	9801.364	0.004
7	2	6	6	1	5	10284.318	-0.005
6	2	4	5	1	5	10344.287	0.022
8	2	7	7	1	6	10750.517	0.006
7	2	5	6	1	6	11055.444	0.004
3	3	1	2	2	0	12664.505	-0.012
3	3	1	2	2	1	12664.937	0.015
4	3	1	3	2	1	13249.436	-0.018
4	3	2	3	2	2	13251.481	0.025
5	3	3	4	2	2	13832.768	-0.030
5	3	2	4	2	3	13838.955	0.004

Table AIV-7. Observed frequencies and residuals (in MHz) for the rotational transitions of rotamer VII of caffeic acid (in MHz).

<i>J'</i>	<i>K'_{-1}</i>	<i>K'_{+1}</i>	<i>J''</i>	<i>K''_{-1}</i>	<i>K''_{+1}</i>	v_{obs}	v_{obs - v_{cal}}
5	1	4	4	1	3	3033.537	-0.005
2	1	2	1	0	1	3288.840	0.005
7	1	7	6	1	6	3999.145	0.024
8	1	7	7	1	6	4847.753	-0.029
5	1	5	4	0	4	4850.921	0.000
9	0	9	8	0	8	5256.347	0.000
6	1	6	5	0	5	5340.612	-0.016
10	1	10	9	1	9	5704.948	-0.003
10	1	9	9	1	8	6052.548	-0.016
6	2	4	6	1	5	6151.913	-0.022
5	2	3	5	1	4	6240.572	-0.015
2	2	1	1	1	0	7648.249	0.001
2	2	0	1	1	1	7683.684	-0.005
3	2	2	2	1	1	8202.819	0.007
3	2	1	2	1	2	8310.001	0.016
4	2	3	3	1	2	8739.817	0.012
5	2	4	4	1	3	9259.283	0.014
5	2	3	4	1	4	9624.287	0.023
6	2	5	5	1	4	9761.320	0.030
3	3	0	2	2	0	12579.548	-0.028
3	3	0	2	2	1	12580.009	0.008
4	3	2	3	2	1	13168.283	-0.010
4	3	1	3	2	2	13170.437	-0.004

Table AIV-8. Observed frequencies and residuals (in MHz) for the rotational transitions of rotamer VIII of caffeic acid (in MHz).

<i>J'</i>	<i>K'₋₁</i>	<i>K'₊₁</i>	<i>J''</i>	<i>K''₋₁</i>	<i>K''₊₁</i>	v_{obs}	v_{obs - v cal}
8	1	8	7	1	7	4573.206	-0.019
8	0	8	7	0	7	4686.285	-0.012
8	1	7	7	1	6	4852.838	0.002
9	1	8	8	1	7	5456.410	-0.022
10	1	10	9	1	9	5710.907	0.019
10	0	10	9	0	9	5834.071	0.002
10	1	9	9	1	8	6058.893	0.022